Abstract

Ghasemzadehsomarin, Farnam. The Effect of Damage on Mass Transport in Cement-based Materials ("Under the direction of Dr. Mohammad Pour-Ghaz")

The premature deterioration of RC structures is a major concern for infrastructure owners. Cracks accelerate the deterioration processes by providing preferential flow paths for water and aggressive agents. Therefore, to accurately estimate the degradation rate, methodologies to account for the effect of discrete and distributed cracks in service life prediction tools need to be developed. To account for the effect of cracks, their effect on moisture transport in concrete needs to be fully understood and quantified.

The research reported in this dissertation provides more insight to the effect of damage induced by freeze-thaw loading on moisture transport. This study includes an extensive experimental program on moisture transport in saturated and unsaturated damaged cement-based materials. Analytical study and numerical modeling are also used to determine the parameters that have significant effect on the mass transport. Furthermore, new nonlinear parameters are proposed to estimate the freeze-thaw damage in concrete using acoustic spectroscopy technique. Therefore, this study consists of four phases.

In the first phase, three objectives are studied: (i) how damage affects the saturated and unsaturated moisture transport as well as electrical resistivity of concrete. Conceptual models are developed based on the fundamentals of damage mechanics and fluid transport to analytically describe the effect of damage, (ii) whether one-dimensional analyses based on the

Sharp Front Theory can explain the relationship between the saturated and unsaturated moisture transport in damaged concrete, and (iii) which transport property and therefore which measurement method is more sensitive to damage. The results show that damage differently affects each of the transport mechanisms, and saturated hydraulic conductivity is more sensitive to damage as compared to sorptivity and electrical resistivity. The 1D analysis, based on the sharp front theory, does not adequately describe the effect of damage on unsaturated transport.

In the second phase, damage was induced by freeze-thaw in mortar specimens. Mass transport properties were measured using electrical resistivity, rapid chloride permeability, sorptivity, drying, air permeability, water permeability, and desorption isotherm. The results indicate that the measured effect of damage depends on the mechanisms of transport used in the measurement technique and different techniques provide a different measure of the effect of damage. The water and air permeability are comparatively more sensitive to the presence of damage.

In the third phase, it is investigated whether classical isothermal unsaturated moisture transport can be used to simulate moisture ingress in damaged mortar and concrete. The results indicate that the unsaturated moisture transport model well simulates early stages of moisture ingress, where capillary suction is the prominent mechanism, for all damage levels. At later stages of moisture transport, where air diffusion and dissolution have significant contribution, simulation results diverge from the experimental results.

In the fourth phase, it is investigated whether Nonlinear Impact Resonance Acoustic Spectroscopy (NIRAS) technique can be provided a method, using nonlinear parameter and nonlinear quality factor (Qfactor) parameter, to estimate the damage in the absence of prior knowledge of intact material?

The outcomes of this work can be used to develop methodologies to integrate the degree of damage measured on concrete structures using non-destructive testing into service life prediction models and therefore more accurately predict the service life of reinforced concrete structures. More accurate service life prediction models can help operators of infrastructure in scheduling the repair and maintenance activities. Service life prediction is a main deriver in life cycle costing and life cycle assessment analyses and therefore developing more accurate service life prediction models can help to more accurately quantify life cycle cost and environmental emissions and implications of concrete infrastructure.

The Effect of Damage on Mass Transport in Cement-based Materials

by
Farnam Ghasemzadehsomarin

A dissertation submitted to the Graduate Faculty of
North Carolina State University
in partial fulfillment of the
requirements for the Degree of
Doctor of Philosophy

Civil Engineering

Raleigh, North Carolina

2015

APPROVED BY:

Mohammad Pour-Ghaz, Ph.D. Committee Chair	Sami H. Rizkalla, Ph.D.
Rudolf Seracino, Ph.D.	Eric Laber, Ph.D.

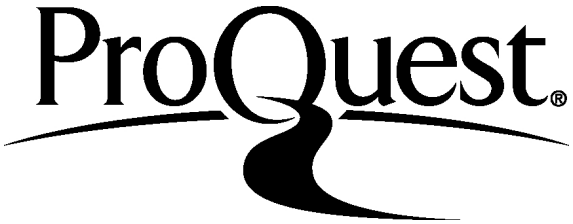

Dedication

This dissertation is dedicated to my beloved family. I specially would like to thank my parents for their endless love, support and encouragement. None of this would have been possible without your support.

Biography

Farnam Ghasemzadeh was born on 1984 in Ardebil, Iran. He completed his BS degree in Civil Engineering from University of Mohaghegh Ardebili, Ardebil, Iran in 2007. Then, he started his graduate program at University of Tehran majoring in structural engineering and construction materials in 2007. During his master degree, Farnam served first as a research assistant and then as a project manager at the Construction Materials Institute (CMI) at the University of Tehran, Iran. While at CMI, Farnam managed several research and industrial projects related to durability design of RC structures as well as repair strategies for deteriorated marine structure. He received the Best Master's Thesis award in Iran and was recognized by President of Iranian Concrete Institute for his contribution in rehabilitation of jetty structures in Persian Gulf, Iran, 2010. After working at CMI, University of Tehran for 5 years, he joined the Wolfpack family at North Carolina State University to pursue his doctoral degree in Structural Engineering and Mechanics in 2012. He studied the influence of distributed damage on mass transport in concrete materials using experimental and numerical techniques at Materials and Sensor Development Laboratory (MSDL) and Constructed Facilities Laboratory (CFL) at North Carolina State University. He earned his doctoral degree in 2015.

Acknowledgements

A special thanks is due to Dr. Mohammad Pour-Ghaz, my thesis supervisor for his countless hours of reflecting, reading, encouraging, and most of all for his patience throughout the past three years. His excitement and willingness to provide feedback made the completion of this research an enjoyable experience. I would like to thank Professors Sami Rizkalla, Rudi Seracino, and Eric Laber for agreeing to serve on my committee and their continued support in this research. I offer my sincere appreciation for the learning opportunities provided by my committee.

I would like also to acknowledge the support, guidance and wisdom of Dr. Gregory Lucier, CFL lab manager, during the past three years. I would like also acknowledge the contributions of the technical staff of CFL (Mr. Jonothan McEntire, and Mr. Jerry Atkinson) as well as the contributions of technical staff of AIF (Mr. Chuck Mooney and Mr. Roberto Garcia) for their assistance and help.

The financial support that I received from the Department of Civil, Construction and Environmental Engineering at North Carolina State University is greatly appreciated.

I would like to extend special thanks to all my colleagues and friends in the Constructed Facilities Laboratory especially Reza Rashetnia and Danny Smyl for their assistance during the numerical phase of this study.

Table of Contents

List of Tables

List of Figures

1. Introduction

The deterioration rate of concrete structures is directly influenced by the ingress of moisture. Therefore, moisture transport influences the majority of deterioration mechanisms of concrete structures. Cracks accelerate the moisture transport and therefore deterioration processes by providing preferential flow paths for movement of water and aggressive agents. To accurately estimate the degradation rate, methodologies to account for the effect of discrete and distributed cracks in service life prediction tools need to be developed. To account for the effect of cracks, their effect on moisture transport in concrete needs to be fully understood and quantified.

While previous studies have enhanced the understanding of the role of cracks and damage, the majority of these studies have investigated the role of cracks and damage in saturated systems. There is a lack of data on the effect of cracks and damage on unsaturated transport. A literature survey also indicates a lack of models that can adequately describe the experimental observations. This research provides fundamental insight to the effect of damage on saturated and unsaturated moisture transport.

Different methods have been developed to measure the transport properties of cement-based materials. These methods provide a different measure of the effect of damage on mass transport properties. A literature review suggests that, first, the effect of discrete cracking is studied in more detail as compared to the effect of damage and second, the effect of damage has been

rarely interpreted in the light of transport mechanisms used in the measurement methods. Third, it is unclear which transport mechanism, and subsequently which measurement method, is more sensitive to the presence of damage. Therefore, this research investigates how do different measurement techniques show the effect of damage on mass transport, and which transport measurement method is more sensitive to the presence of damage.

1.1 Objectives

The objectives of present research are to:

- Investigate the effect of damage (distributed cracks) on mass transport properties of concrete and understand how damage changes the mechanisms of mass transport in cement-based materials,
- Understand how damage affects different mass transport mechanisms,
- Understand whether classical unsaturated transport can be used to model unsaturated transport in damaged materials.
- Develop a new method to estimate damage in cement-based materials using Nonlinear Acoustic Spectroscopy in the absence of prior knowledge of the undamaged properties.

1.2 Thesis organization

This thesis is organized in six chapters. Chapter 1 of this thesis presents the introduction and motivations of this study.

In Chapter 2, three objectives were studied: (i) how damage affects the saturated and unsaturated moisture transport as well as electrical resistivity of concrete. Conceptual models were developed based on the fundamentals of damage mechanics and fluid transport to analytically describe the effect of damage, (ii) whether one-dimensional analyses based on the Sharp Front Theory can explain the relationship between the saturated and unsaturated moisture transport in damaged concrete, and (iii) which transport property and therefore which measurement method is more sensitive to damage. This chapter in the present format is published in Ghasemzadeh and Pour-Ghaz (2014).

In chapter 3, it is investigated which transport measurement method appropriately quantify the effect of damage in mass transport. Therefore, mass transport properties were measured using electrical resistivity, rapid chloride permeability, sorptivity, drying, air permeability, water permeability, and desorption isotherm. This chapter in the present format is submitted for publication (Ghasemzadeh and Pour-Ghaz 2015).

In chapter 4, it is investigated whether classical isothermal unsaturated moisture transport can be used to simulate moisture ingress in damaged mortar and concrete. In this study, the input variables for numerical modeling obtained using experiments and numerical modeling was conducted using HYDROUS. This chapter in the present format is submitted for publication (Smyl et al. 2015).

In chapter 5, it is investigated whether Nonlinear Impact Resonance Acoustic Spectroscopy (NIRAS) technique can provide a method, using nonlinear parameter and nonlinear quality factor (Q-factor) parameter, to estimate the damage in the absence of prior knowledge of intact material. This study in the present format is submitted for publication (Rashetnia et al. 2015).

Chapter 6 presents the summary and conclusion of findings outlined in this dissertation.

2. Effect of Damage on Moisture Transport in Concrete

2.1 Introduction

The premature deterioration of reinforced concrete (RC) structures is a major concern for infrastructure owners (Ghasemzadeh et al. 2013, Shekarchi et al. 2012a). Cracks accelerate the deterioration processes by providing preferential flow paths for water and aggressive agents. Therefore, to accurately estimate the degradation rate, methodologies to account for the effect of discrete and distributed cracks in service life prediction tools need to be developed. To account for the effect of cracks, their effect on moisture transport in concrete needs to be fully understood and quantified.

Cracking can be classified into discrete (or localized) or distributed cracking (network of micro-cracks). Discrete cracks are typically a result of mechanical loading, thermal or shrinkage cracking in concrete. Distributed cracking (referred to as "damage" hereafter) is often associated with cracking due to moisture gradient, freeze-thaw, and Alkali Silica Reaction (ASR) (Langton 2012). Discrete cracking and damage often coexist. While both accelerate the fluid ingress, due to the significant geometric differences between them, they are generally separately dealt with in modelling efforts.

Many researchers have contributed to service life prediction modelling (e.g., Fagerlund 1997, Lockington et al. 1999, Thomas and Bentz 2000, Bentz and Thomas 2001, Henchi et al. 2007,

Brade et al. 2009). The majority of the existing models, however, do not consider the effect of cracks and damage. The effect of discrete cracks on mass transport has been investigated by many researchers (Bentz et al. 2013, Akhavan and Rajabipour 2012, Akhavan et al. 2012, Chunsheng et al. 2012, Pour-Ghaz et al. 2009a and 2009b, Picandet et al. 2009, Djerbi et al. 2008, Yang Z. et al. 2006, Rodriguez and Hooton 2003, Reinhardt and Jooss 2003, Aldea et al. 1999a and 1999b, Wang et al. 1997). Wittke (1990) showed that the rate of flow of water is proportional to the cube of crack width in rocks – referred to as the Cubic Law. Wang et al. (1997) and later Aldea et al. (1999b) experimentally showed that water permeability of concrete containing discrete cracks increases with crack width, number of cracks, and crack length. Tognazzi et al. (1998) showed, using modelling, the dependence of chloride diffusion in cracked concrete on the crack width. Aldea et al. (1999a) showed that the presence of discrete cracks dominates the overall saturated transport in concrete, and therefore, both high and normal strength cracked concretes show similar water permeability. Aldea et al. (1999a) also showed that the presence of discrete cracks more drastically increase the water permeability as compared to chloride permeability. The more recent investigations have underlined the importance of crack geometry (i.e., length, orientation and connectivity) and crack density (Chunsheng et al. 2012). Akhavan and Rajabipour (2012) investigated the effect of discrete cracks on the electrical conductivity and ion diffusion and concluded that the volume fraction of cracks (as compared to crack width) may better describe the effect of cracks. Akhavan et al. (2012) showed that crack permeability is dependent on the crack tortuosity, surface roughness of the crack, and square of crack width as was described by Cubic Law.

Damage can also accelerate the ingress of water and aggressive agents in concrete (Chung et al. 2010, Yang et al. 2006, Yang et al. 2004, Jacobsen 1998, Wiens et al. 1997, Jakobsen et al. 1996, Saito et al. 1994, Ghassemzadeh et al. 2010, Shekarchi et al. 2012b). Jacobsen et al. (1996) observed that freeze-thaw induced damage reduces the compressive strength and increase the chloride penetration rate up to 7.9 times. Fagerlund (1996) showed that water absorption increases with increased micro-cracking due to freeze-thaw. Wiens et al. (1997) also showed that micro-cracking due to freeze-thaw increases the rate of water and deicing salt penetration. Yang et al. (2006) reported a linear increase of water absorption and bilinear increase of electrical conductivity with damage caused by freeze-thaw. Chung et al. (2010) also showed that concretes that experienced freeze-thaw damage show a high chloride transport rate.

While previous studies have enhanced our understanding of the role of cracks and damage, the majority of these studies have investigated their effects in saturated systems. There is a lack of data on the effect of cracks and damage on unsaturated transport. A literature survey also indicates a lack of models that can adequately describe the experimental observations. The main goal of this research is to provide more insight to the effect of damage on moisture transport. In this research it is investigated: (i) how damage affects the saturated and unsaturated moisture transport as well as electrical resistivity of concrete. Conceptual models are developed based on the fundamentals of damage mechanics and fluid transport to analytically describe the effect of damage, (ii) whether simple one-dimensional analyses based on the Sharp Front Theory can explain the relationship between the saturated and unsaturated

moisture transport in damaged concrete, and (iii) which transport property and therefore which measurement method is more sensitive to damage. Material constants are also provided for numerical modelling of unsaturated transport in the specific damaged concrete investigated in this paper.

In this work damage was induced by freeze-thaw and is quantified using Ultrasonic Pulse Velocity (UPV) and active acoustic emission. Passive acoustic emission measurements were also performed to monitor damage development during the freeze-thaw cycles. The water permeability (Saturated Hydraulic Conductivity – SHC) of damaged concrete specimens were measured using a newly developed equipment. Desorption isotherm, sorption, and electrical resistivity measurements were performed.

In the following of this chapter, materials and methods used in this research are presented. This is followed by the results section. Then the results are discussed in detail and analytical calculations and the conceptual damage models are presented. Finally the conclusions of this study are presented.

2.2 Material and Methods

2.2.1 Materials, mixture proportioning, and specimens preparation

Ordinary Portland cement Type I and class F fly ash (24% replacement by weight of cement) were used. The concrete mixture had a water-to-cementitious (cement + fly ash) ratio of 0.50.

Crushed limestone aggregate with a maximum aggregate size of 19 mm and natural river sand with a fineness modulus of 2.67 were used. The concrete was produced by a local ready-mix producer according to ASTM C94. **Table 2-1** provides the concrete mixture proportion.

Table 2-1: Mix proportion of concrete

Cement	Fly ash Type (F)	Water	Coarse Aggregate	Fine Aggregate	Water Reducer
kg/m^3	kg/m^3	kg/m^3	kg/m^3	kg/m^3	kg/m^3
261	83	132.5	1073	747	0.50

Concrete was cast in 102x204 mm (4x8 inch) cylinders and samples were kept sealed for the first 24 hours. The samples were then demolded and cut into appropriate geometries using a diamond-tipped wet saw: 25 mm (1 inch) thick disks for water absorption, electrical resistivity, Saturated Hydraulic Conductivity (permeability) and UPV tests; 50 mm (2 inch) thick disks for acoustic emission and UPV measurements; 10 mm thick specimens with approximate dimensions of 40x40 mm for Scanning Electron Microscope (SEM) imaging; 5.6 mm thick specimens with approximate dimensions of 80x40 mm for moisture desorption isotherm measurements. All of the specimens were cured in lime-saturated water at 25±1°C for 180 days after cutting.

2.2.2 Freeze-thaw testing

An air-cooled freeze-thaw chamber was used. Each cycle was 12 hours including a 2-hour cooling period from 20°C to -23ºC, a 4-hour rest period at -23ºC, 2-hour heating period from -23ºC to 20°C, and a 4-hour rest period at 20ºC. The slow transition period and the rest periods were considered to ensure that the core temperature of all samples with different thickness reach to equilibrium with the air. All specimens were wrapped in a water saturated cloth and were sealed using a thin plastic sheet to keep them saturated during the freeze-thaw testing (Li et al. 2011). A total of five cycles were used and after each cycle a set of specimens were removed from the chamber while other specimens were left to undergo further freeze-thaw cycles.

2.3 Damage Detection Methods

2.3.1 Acoustic Emission

Active acoustic emission was used to monitor the damage in concrete specimens at the end of each cycle (two hours into the thawing period). Passive acoustic emission was used to continuously monitor the damage during the freeze-thaw cycles (Shimada et al. 1991, Farnam et al. 2014). Acoustic emission sensors with a peak frequency of 375 kHz were used. Sensors were installed at opposite sides of the disk specimens (**Figure 2-1**). The curved surface of the specimens was slightly trimmed tangent to the perimeter to facilitate a flat surface for a better contact of sensors with the specimen. A thin layer of vacuum grease was used to couple the sensors to the specimens. Specimens were then placed on a layer of acoustic mat resting on a

rigid stainless steel frame that was isolated from the chamber to minimize vibration and noise. A stainless steel rod was also used as a "reference" specimen to monitor the environmental noise during the test and to ensure that the coupling agent did not degrade during freeze-thaw (Li et al. 2011).

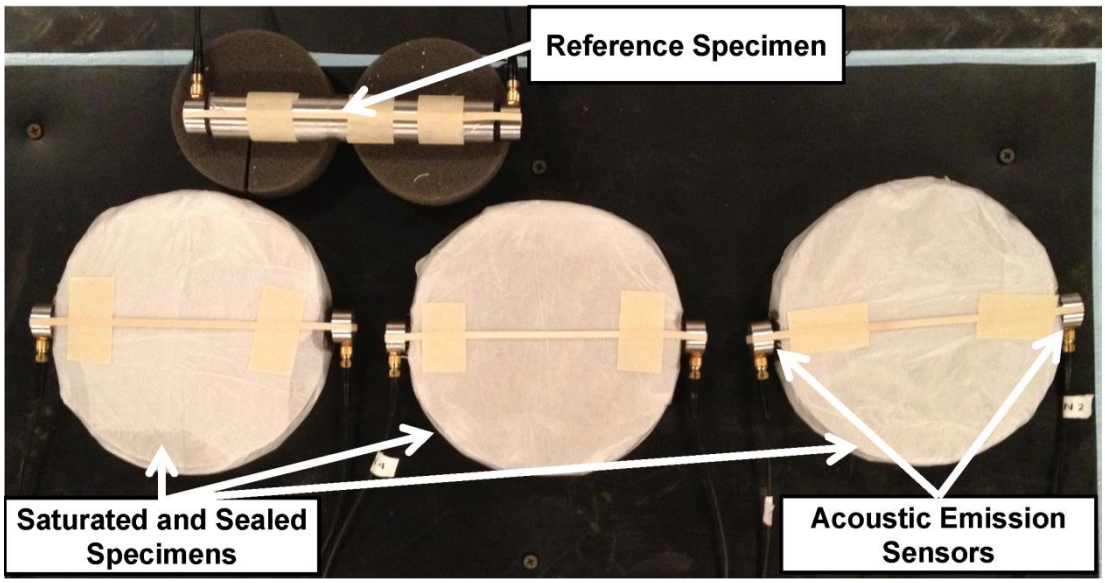

Figure 2-1: Photograph of sealed concrete specimens used in acoustic emission test; a stainless steel rod that does not undergo freeze-thaw damage was used as a reference sample

2.3.2 Ultrasonic Pulse Velocity

UPV was used to quantify the damage, using UPV transducers with 250 kHz frequency. Measurements were performed on four specimens. The specimens were prepared similar to acoustic emission specimens, trimmed perimeter and using vacuum grease, to facilitate a

robust contact between the transducers and the specimen. Similar approach was previously used by Jacobsen et al. (1996).

2.3.3 Scanning Electron Microscopy (SEM)

Scanning Electron Microscopy (SEM) specimens were dried in an oven at 50°C for 48 hours. To minimize cracking during cutting /polishing of the specimens, they were impregnated with an ultra-low viscosity epoxy (200-350 centipoise) under high pressure vacuum pump (0.015 mm Mercury). Impregnated specimens were then cured in an oven at 50° C for 10 hours and were then cut and polished with silicon carbide sand papers (60, 120, 240, 320, 400, 600, 800 and 1200 grits) and a half-micron diamond suspension. Backscattered mode was used for SEM imaging with pressure and accelerating voltage of 30 Pa and 20.0 kV.

2.3.4 Electrical resistivity

Electrical Impedance Spectroscopy (EIS) was used to measure the bulk electrical resistivity of the specimens. Measurements were performed with 500 mV amplitude over a frequency range of 1 Hz to 1 MHz. A total of seven specimens for each degree of damage was measured. To minimize the effect of temperature, specimens were placed in a large water bath at 23+1°C, prior to measurement, until they reached to thermal equilibrium with the water (6 to 8 hours). The specimens were sandwiched between two stainless steel plate electrodes. A Copper-based conductive gel was used to improve the contact of the electrodes with the specimen (Castro et al. 2011b).

2.3.5 Saturated hydraulic conductivity

In this research, it is intentionally used the term "saturated hydraulic conductivity (SHC)" instead of permeability to avoid confusion with different definitions, terminologies, and units that have been used in literature for "permeability" of concrete. The authors define the SHC, K_s with dimensions [LT^{-1}], for a homogeneous isotropic material per Darcy's law ($q = -K_s \nabla h$) where q is the Darcy flux and ∇h is the hydraulic gradient (Charbeneau 2006).

The SHC was measured using an in-house developed equipment set that works by measuring the pressure of a column of water (burette) on top of the concrete disk using a high resolution pressure sensor with a range of 0.0 to 1.0 psi (0-69 mbar) (**Figure 2-2**). Measures were taken to minimize the evaporation from the burette by facilitating an atmospheric pressure contact through a 0.45 mm diameter hole. Measurements on a polymeric disk (with zero effective SHC) showed that the effect of evaporation is negligible. The pressure transducer data was collected at one-minute intervals on a computer. Due to high sensitivity of the pressure sensor, pressure from a 60-cm water filled burette was enough to produce measurable drop in pressure. Depending on the permeability of the specimen, measurements were completed in 12 to 72 hours. Using this equipment, SHC of 102 mm (4 inch) diameter disk specimen with 25 or 50 mm (1 or 2 inch) thickness can be measured. Falling head method (Charbeneau 2006) was used to calculate SHC after reaching a steady-state flow.

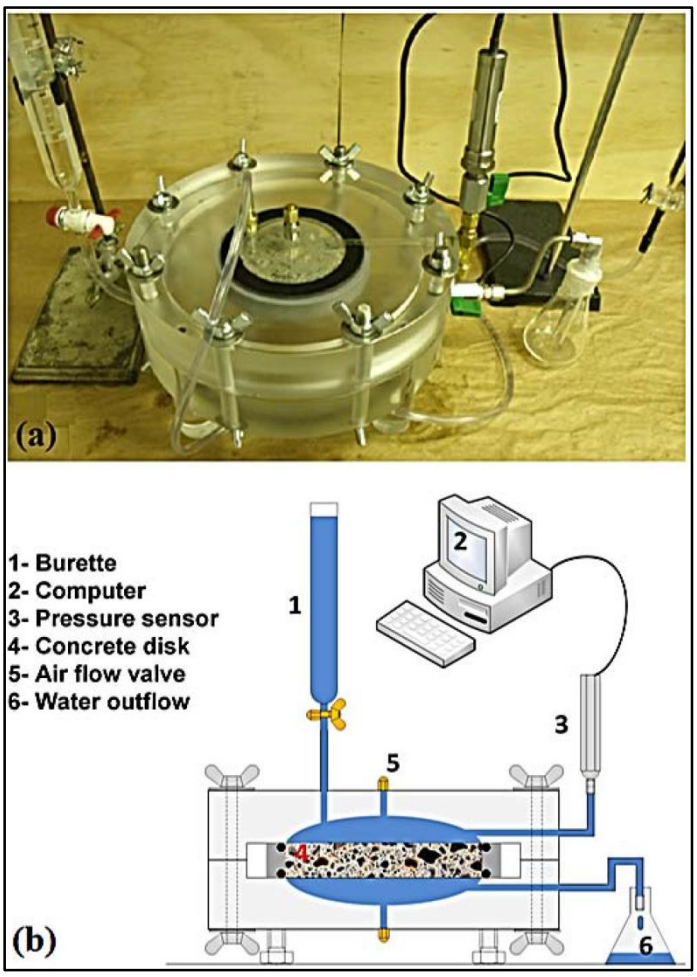

Figure 2-2: Saturated hydraulic conductivity measurement equipment: (a) photograph of the equipment; (b) schematic illustration of the equipment

A total of three replicates were used for each degree of damage. Before the measurements, the circumference surface of the specimens was coated with a rapid setting epoxy. The specimens were saturated under water using a desiccator and high vacuum pump (0.015 mm Mercury) to remove all air pockets. All the measurements were performed in a temperature controlled room at 23+1^{o}C.

2.3.6 Water absorption

Water absorption measurements were carried out similar to the ASTM C1585 procedure with the difference that the specimens were 25 mm (1 inch) thick instead of 50 mm. A total of three specimens were used for each degree of damage. The water absorption tests were carried out for 90 days.

2.3.7 Desorption isotherm

The concrete specimens were conditioned at six relative humidities using four saturated salt solutions ($MgCL_2$ (32.8% RH), $NaCL_2$ (75.3% RH), KCL (85.1% RH), and KNO_3 (93.6% RH)) and two environmental chambers (50% and 65%). When using salt solutions, samples (and the salt solution) were placed inside a glass airtight cabinet desiccator that was placed in a large chamber at 23±1°C. A total of three replicate specimens were used for each degree of damage at each relative humidity (a total of 108 samples). The average weight of the specimens was 52.5 g (with standard deviation of 5.2 g) and the average thickness of the specimens was 5.62 mm (with standard deviation of 1.29 mm). After six months, specimens were weighted using an analytical balance with 0.1 mg resolution in one-month intervals until equilibrium. Equilibrium was defined as variation of less than 1.0 mg in one month interval. Specimens were then dried at 105° C for 24 hours to calculate their water content.

2.4 Results

2.4.1 Damage detection methods

Figure 2-3a shows the measured degree of damage with active acoustic emission and UPV. The damage index (D) is calculated based on the wave travel time in damaged and undamaged specimens and calculating the relative elastic modulus based on equation 2-1.

$$D = 1 - \frac{E_t}{E_o} = 1 - \left(\frac{t_o}{t_t}\right)^2 \qquad \text{Eq. 2-1}$$

where E_t is the dynamic elastic modulus after freeze-thaw, E_o the initial dynamic elastic modulus before freeze-thaw, t_t is the signal transmission time after freeze-thaw, and t_o is the initial signal transmission time before freeze-thaw. In using equation 2-1, we assume that the change in concrete density with damage is negligible.

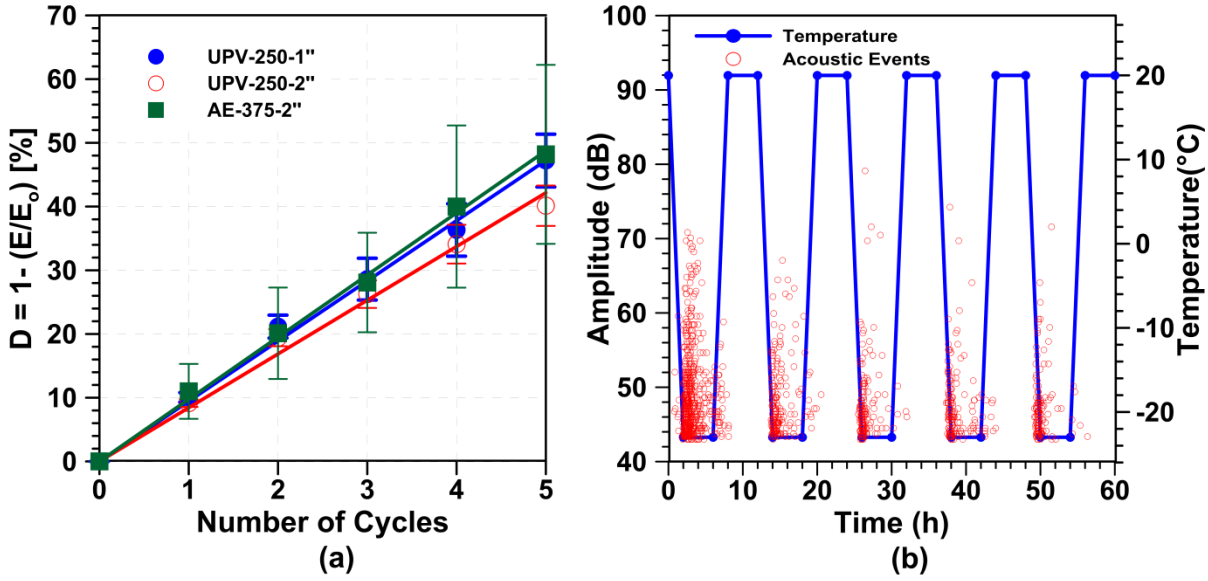

Figure 2-3: (a) Degree of damage calculated based on reduction in elastic modulus monitored using active acoustic emission and ultrasonic pulse velocity; (b) amplitude of captured acoustic events during the freeze-thaw loading using passive acoustic emission

The results of acoustic emission (AE-375-2") in **Figure 2-3**a are an average of three measurements on 50 mm (2 inch) thick disks. The results of UPV in **Figure 2-3**a are an average of four measurements with 50 mm (2 inch) and 25 mm (1 inch) thickness; the results are shown with UPV-250-2" and UPV-250-1" respectively. The degrees of damage measured with the two methods are very close to each other. In **Figure 2-3**a, D increases almost linearly with freeze-thaw cycles. Generally, concrete does not show such a high degree of damage with a few freeze-thaw cycles. However, in this work no air entrainment was used and the concrete specimens were saturated beyond the critical degree of saturation. As was shown previously by others (Li et al. 2011; Fagerlund 1977) when concrete is saturated beyond the critical degree of saturation, significant damage develops in concrete even with a small number of cycles. In all the experiments in this research, 50 mm (1 inch) thick samples were used, and therefore, in

the rest of this paper the damage index measured by UPV-250-1" were used in analyzing the data.

Figure 2-3b illustrates the peak amplitude of the captured acoustic emission events (average of three specimens). In all cycles, acoustic emission events start at the temperatures below -10°C with a small number of events observed at temperatures above -10°C. The events captured at temperatures below -10°C are mainly due to cracking of the concrete. Pore solution freezes at temperatures lower than 0°C due to the effect of dissolved salts in the pore solution as well as the effect of pore confinement (Fagerlund 1973 and Helmuth 1960).

A significantly higher number of events are captured in the first cycle as compared to the subsequent cycles and the number of acoustic emission events decreases with number of cycles. This is because concrete shows Kaiser effect: the cracks that develop during a given cycle, do not produce acoustic hits in the subsequent cycles (Li et al. 2011). While the results in **Figure 2-3**b indicate that the rate of damage development decreases with number of cycles, **Figure 2-3**a indicates that the damage continues to increase. This may be explained by the increase in the crack width of the cracks in later cycles as opposed to increase in the number cracks. This observation agrees with the damage model developed and discussed later in this paper.

2.4.2 Scanning electron microscope

Figure 2-4 illustrates the SEM images of the concrete specimens. Two SEM images with different magnifications are shown for each degree of damage. No cracking is observed in the undamaged specimens (**Figure 2-4**a and **Figure 2-4**b) indicating that sample preparation did not introduce damage. At 10.1% damage (**Figure 2-4**c and **Figure 2-4**d) cracks are mainly observed around the aggregates. These cracks are connected by cracks in the bulk paste. Similar observations were made by Jacobsen (1998) indicating initiation of cracks at the paste-aggregate interface. At 28.6% damage (**Figure 2-4**e and **Figure 2-4**f), the crack density at the interfaces and within the bulk paste increases and cracks become more interconnected. At 47.2% damage (**Figure 2-4**g and **Figure 2-4**h) cracks are well distributed and interconnected. The crack width also increases as compared to 28.6 and 10.1% damage.

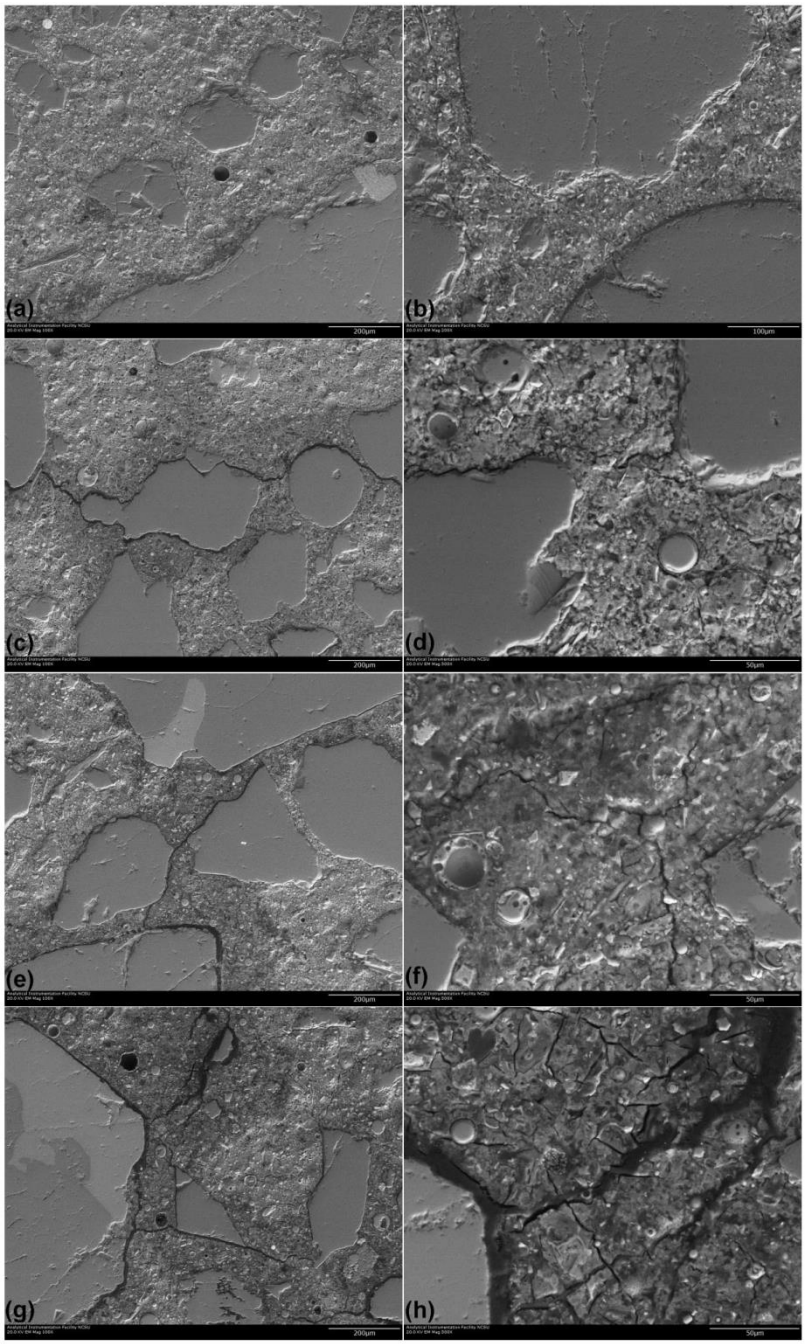

Figure 2-4: Scanning Electron Microscope (SEM) Images of concrete specimens with different degrees of damage (D) with two magnifications: (a) D=0,100X; (b) D=0, 200X;(c) D=10.1%, 100X; (d) D=10.1%, 500X; (e) D=28.6%, 100X; (f) D=28.6%, 500X; (g) D=47.2%, 100X; (h) D=47.2%, 500X.

Figure 2-5 illustrates a SEM image of a concrete specimen with 47.2% damage. It can be seen that cracks are connected to an air void. A similar observation has been previously reported by Yang et al. (2006). The connectivity of the cracks to air voids significantly affects the transport properties of concrete, specifically, it affects the secondary water sorptivity of the specimens as will be discussed later.

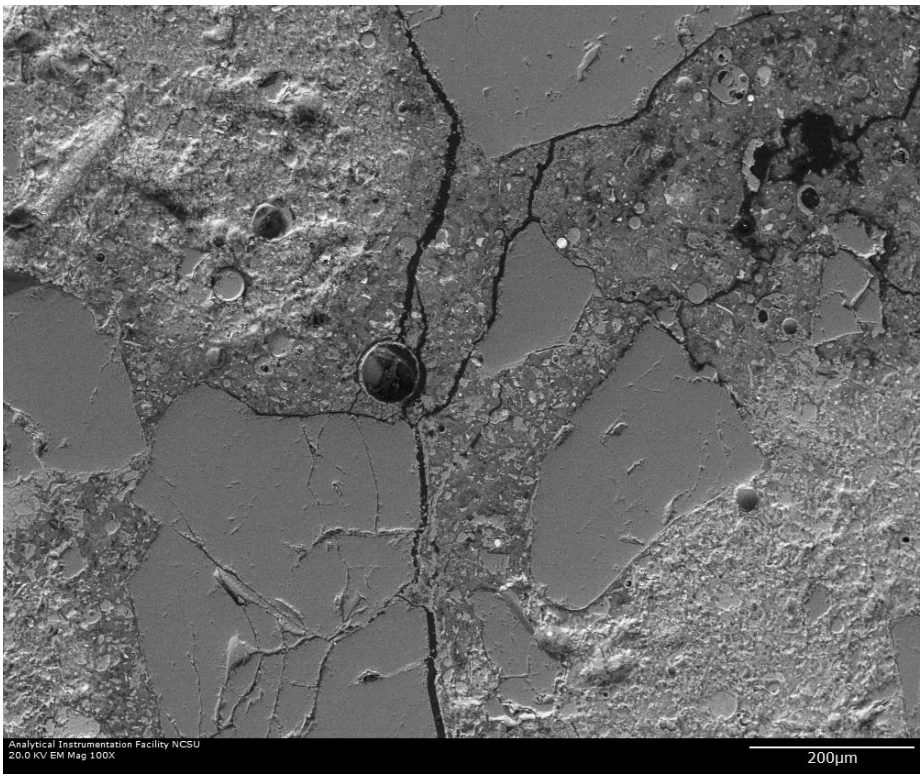

Figure 2-5: Scanning Electron Microscope (SEM) image of concrete with 47.2% damage illustrating the connectivity of the cracks with an air void

2.4.3 Electrical resistivity

Figure 2-6 illustrates the change in the normalized electrical resistivity with damage. The normalized resistivity was obtained by dividing the resistivity of each specimen to its initial resistivity (ρ_o =150.03 Ohm.m average of seven specimens). A "slight" bilinear reduction is observed: the normalized resistivity decreases with a higher rate initially up to 10.1% damage and then decreases with a lower rate from 10.1% to 47.2% damage. Similar bilinear reduction has been previously observed by Yang et al. (2006). According to Yang et al. (2006) the initial higher reduction rate is due to the formation of the cracks while the lower rate afterward reflects the increase of crack width of the existing cracks. In addition to the proposed effects by Yang et al. (2006), the connectivity of the cracks to air voids (as shown in **Figure 2-6**) might also have an effect on the reduction of electrical resistivity as air voids act as current distribution "hubs" resulting in an increased connectivity of the micro-cracks.

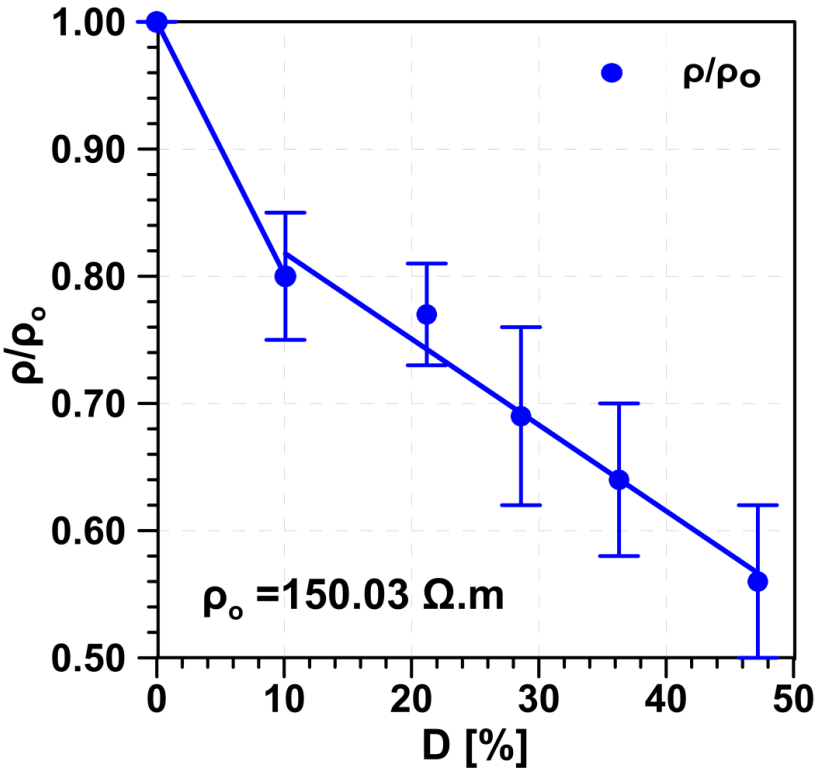

Figure 2-6: Reduction of the normalized electrical resistivity of concrete samples with increased damage; the normalized values are obtained by dividing the resistivity in damaged specimens to the resistivity of the undamaged samples

2.4.4 Saturated hydraulic conductivity

Figure 2-7 illustrates the normalized SHC of the specimens where the SHC values are normalized to the average SHC of the undamaged concrete (K_o=3.77x10^{-11} m/s). The SHC increases with damage as a consequence of increasing crack density and interconnectivity of the cracks. Note that the SHC increase approximately two orders of magnitude when damage increases to 46.2%. The results illustrate the exponential increase of SHC with damage. The rate of the increase in SHC increases more significantly after 28% damage.

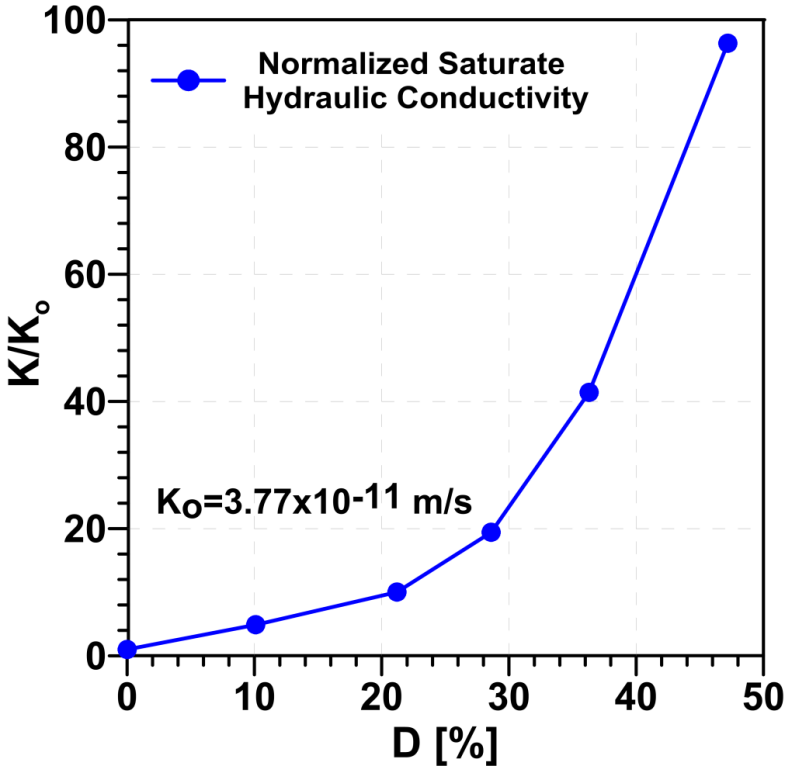

Figure 2-7: Increase in normalized saturated hydraulic conductivity of damaged concrete samples; the normalized values are obtained by dividing the SHC in damaged specimens to the SHC of the undamaged samples

2.4.5 Water sorption

Figure 2-8a illustrates the results of water absorption during the first 90 days (average of three specimens). The maximum standard deviation for each plot is shown in the legend. The volume of absorbed water is normalized to the surface area of the specimen and is plotted against the square root of time. The slope of the first and second linear portions are referred to as "initial" and "secondary" sorptivity respectively, following the terminology in ASTM C1585 and reference (Castro et al. 2011a and 2011b). Note, however, that the true sorptivity driven by capillary suction is the initial sorptivity. Figure 8b shows the normalized initial and secondary

sorptivity of concrete to those of the undamaged sample. The initial sorptivity increases linearly with damage. The secondary sorptivity initially decreases with damage and then remains approximately independent of damage (although slight decrease can be observed). Note that in **Figure 2-8**a damage mainly affects the transition period between the two linear regions.

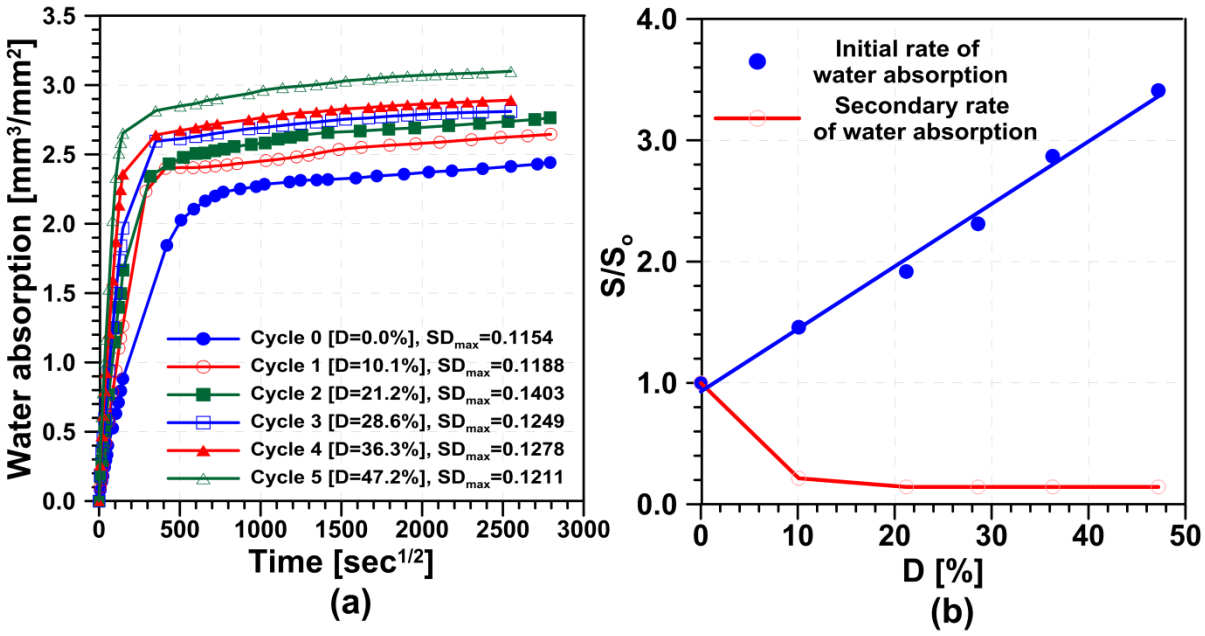

Figure 2-8: (a) Water sorption of concrete specimens during the first 90 days; (b) normalized initial and secondary water sorptivity of concrete as a function of degree of damage; the initial and secondary sorptivity values are normalized to the initial and secondary sorptivity of undamaged concrete respectively

2.4.6 Desorption isotherm

Figure 2-9 illustrates the desorption isotherm of concrete specimens at relative humidity values above 50%. At 50% relative humidity, the water content is approximately the same for all the specimens with different degrees of damage. The water content increases with damage

showing that cracks act as capillary porosity and retain more water within the material. The isotherm suggests that the cracks from freeze-thaw cover a rather wide range of sizes below what is observed in SEM images (illustrated in **Figure 2-4** and **Figure 2-5**).

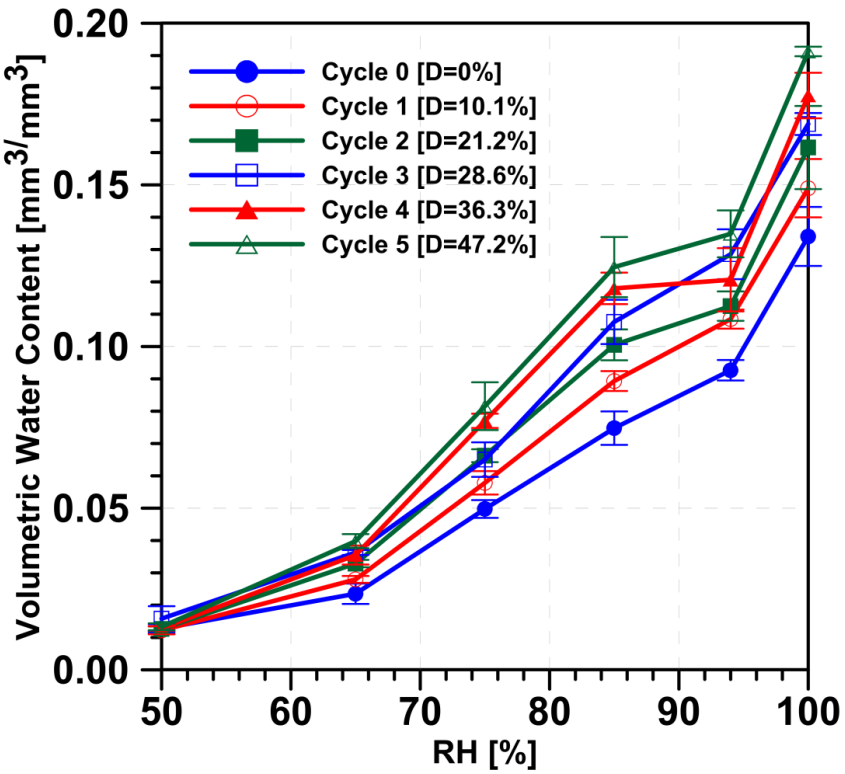

Figure 2-9: Desorption isotherm of concrete specimens with different degrees of damage

2.5 Discussion

2.5.1 Phenomenological explanation of the effect of damage on the initial and secondary sorptivity

The bilinear water absorption as a function of square root of time (**Figure 2-8**a) is caused by two different processes: the first linear portion (initial sorption period) is attributed to the filling

of the capillary pores by capillary suction and the second linear portion (secondary sorption period) is attributed to the slow water transport to larger (as compared to capillary pores) air-filled pores by air-dissolution process (Fagerlund 2012). Secondary sorptivity is also attributed in part to micro-structural changes such as swelling of calcium silicate hydrate (C-S-H) gel and rehydration (Hall et al. 1995). Counterarguments, however, have also been made against swelling of C-S-H (Hanzic et al. 2010).

The authors explain the effect of damage on both water absorption stages using the abovementioned mechanisms by Fagerlund (2012). The distributed cracks affect the initial sorptivity by three mechanisms: (i) cracks act as capillary tubes increasing the porosity of the material. The desorption isotherms in **Figure 2-9** support this concept showing that the distributed cracks may be considered as additional capillary porosity with a wide size distribution; (ii) cracks act as preferential flow paths providing access to capillary pores away from the exposed surface of the specimen; and (iii) cracks provide access to the larger air-filled pores, and therefore, some of these pores (that are generally filled during the secondary sorption period) will be filled during the initial sorption period. The SEM image in **Figure 2-5** which shows that some of the cracks are connected to an air void supports this concept.

The last effect, describes the reason for the decrease of the secondary sorptivity in damaged concrete. Since a fraction of the air-filled voids are filled with water during the first sorption period, a smaller fraction of these air-filled voids are empty during the secondary sorption period. Also, according to the results of acoustic emission in **Figure 2-3**b, a larger number of

cracks forms in the first cycle, therefore, the largest decrease in the secondary sorptivity occurs after the first cycle. **Figure 2-10** illustrates this phenomenological explanation.

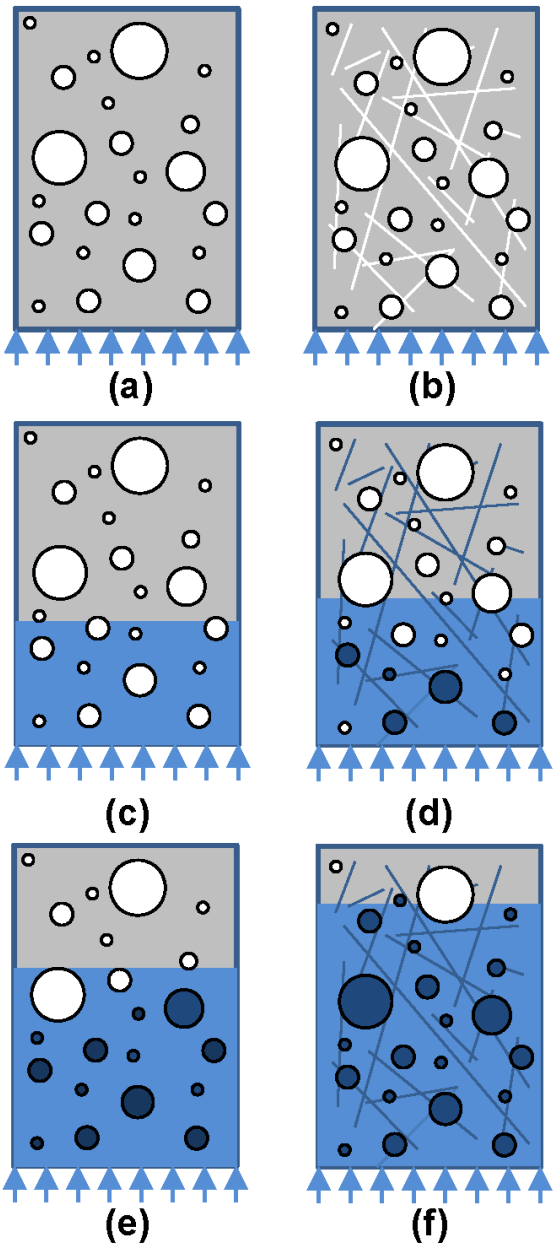

Figure 2-10: Schematic illustration of the effect of damage on water absorption in concrete; the left and right column, respectively, illustrate the undamaged and damaged materials; cracks act as additional porosity, provide access to capillary pores away from the exposed surface of the specimen, and provide access to air-filled voids during the first absorption period; therefore, the initial sorption rate is higher in damaged materials as compared to undamaged materials; during the secondary sorption period, a smaller fraction of air-filled voids are empty in the damaged material and therefore the secondary sorption rate decreases with increase of damage.

It should be noted that air voids do not produce a significant capillary suction due to their large size. Therefore, during the first sorption period, in damaged material, only very small air voids are filled with water by capillary suction. Cracks also accelerate the air-dissolution process in air voids. Thus, during the first sorption period, a portion of air voids are filled by a combination of capillary suction and accelerated air-dissolution process. It is also possible that, during the first sorption period in damaged materials, water forms a thin film on the wall surface of large pores that lack capillary suction (Hanzic et al. 2010).

In **Figure 2-10**, the left and right columns, respectively, illustrate the undamaged and damaged material. The first row illustrates the initial condition where the capillary pores, air-filled voids, and cracks are empty. In **Figure 2-10**c, water is absorbed by capillary pores during the initial sorption period into the undamaged material. In **Figure 2-10**d water is absorbed by capillary pores and cracks into the damaged material. In addition, some of the air-filled voids are filled with water during the initial sorption period. This explains the higher rate of initial water sorption by damaged materials. In the last row, both materials enter into the secondary sorption period. In **Figure 2-10**e the air-filled voids in the undamaged material start to fill with water. In **Figure 2-10**f, however, some of the air-filled voids had already been filled with water during the initial sorption period (**Figure 2-10**d) and a smaller fraction of these air-filled voids are filled with water in the secondary sorption period.

2.5.2 The correlation between saturated and unsaturated flow in damaged concrete based on Sharp Front Theory

In this section, analyses based on the Sharp Front (SF) model are performed to understand whether the effect of damage on saturated flow (saturated hydraulic conductivity – SHC) can be used to describe the effect of damage on unsaturated flow. The SF model is based on simplifying assumptions that enable obtaining a closed-form solution. The SF model was originally developed by Green and Ampt (1911) and has been improved since (e.g., Hall and Hoff 2011 and the references therein). The fundamental assumptions in SF model include: (i) flow is one-dimensional and uniformly progresses in an semi-infinite domain, (ii) the initial water content is uniform throughout the material and remains uniform and equal to the initial water content ahead of the wetting front, (iii) the water content is uniform behind the wetting front and is equal to the saturation water content or some value very close to it, and (iv) the wetting front is sharp (e.g., step function) and changes abruptly from the water content behind the wetting front to the initial water content.

The first assumption agrees with the standard sorption measurements. The second assumption may only be achieved by long-term conditioning and may not be a valid assumption for samples conditioned according ASTM C1585. This assumption is necessary to avoid complex mathematical procedures. While the assumptions iii and iv are not valid for all porous materials, x-ray absorption measurements by Pour-Ghaz et al. (2009a) have shown that during water absorption in dry cement paste the water content behind the wetting front remains close to the saturation water content and the water front is sharp and well approximated with a step

function. For simplicity, the gravitational effects, the effect of air flow, and air compressibility are ignored herein. Gravitational effects are negligible in this case due to the small pore size distribution of concrete and small height of the samples (Hall 1994). Variations of SF model that account for the gravitational effect (Hall 1994), air displacement by water (Wang et al. 1998) and air compressibility (Culligan et al. 2000) have been proposed by others. The SF model can be written as equation 2-2 (Charbeneau 2006)

$$I(t) = K_{ns}t + (\theta_{ns} - \theta_i)(H + \psi_f)\ln\left(1 + \frac{I(t)}{(\theta_{ns} - \theta_i)(H + \psi_f)}\right) \quad \text{Eq.2-2}$$

where I(t) is the cumulative absorption at time t per unit area of the specimen, K_{ns} is the SHC of the wetted region, θ_{ns} is the water content of the wetted region, θ_i is the initial water content, H is the height of the ponding water, and ψ_f is the wetting front pressure head. Note that K_{ns} and θ_{ns} are some value close to (but not equal to) the SHC, K_s, and the saturation water content, θ_s. For simplicity, it is assumed $K_{ns} \approx K_s$ and $\theta_{ns} \approx \theta_s$. Using logarithmic expansion, equation 2-2 is reduced to the short-term expression in equation 2-3 (Charbeneau 2006)

$$I(t) = \sqrt{2K_s(\theta_s - \theta_i)(H + \psi_f)t} \quad \text{Eq.2-3}$$

In equation 2-3, the cumulative absorption is linearly proportional to the square root of time and therefore the sorptivity, S, is given as

$$S = \sqrt{2K_s(\theta_s - \theta_i)(H + \psi_f)} \qquad \text{Eq.2-4}$$

Since equations 2-3 and 2-4 are obtained by short-term expansion, equation 2-4 corresponds to the initial sorptivity. In sorption test, in general H = 0 (since absorption is upward) and equation 2-4 reduces to

$$S = \sqrt{2K_s(\theta_s - \theta_i)\psi_f} \qquad \text{Eq.2-5}$$

While simple, equation 2-5 provides significant insight to the behaviour of the material: (i) sorptivity increases linearly with square root of SHC, (ii) difference between saturation and initial water content (i.e., $\theta_s - \theta_i$) indicates that the sorptivity decreases as the initial water content increases; this was experimentally shown in (Castro et al. 2011a, Parrott 1994, and Parrott 1991), (iii) if the information about ψ_f (the wetting front pressure head) is available, equation 2-5 can be used to estimate the SHC of concrete from sorption data. Equation 2-6, below, is obtained by taking the ratio of the sorptivity for two materials using equation 2-5:

$$\frac{S_2}{S_1} = \sqrt{\frac{K_{s,2}}{K_{s,1}}}\sqrt{\frac{\theta_{s,2} - \theta_{i,2}}{\theta_{s,1} - \theta_{i,1}}}\sqrt{\frac{\psi_{f,2}}{\psi_{f,1}}} \qquad \text{Eq.2-6}$$

where subscripts 1 and 2 indicate materials 1 and 2, respectively, and other parameters bear the same definition as previous equations. Equation 2-6 indicates that the ratio of sorptivity

increases linearly with square root of ratio of SHC. By considering undamaged and damaged concrete as material 1 and 2, respectively, a theoretical initial sorptivity ratio is obtained. Equation 2-6 can be further simplified by neglecting the contribution of the last two factors on the right hand side and can be written in the form of equation 2-7

$$\frac{S_2}{S_1} = \sqrt{\frac{K_{s,2}}{K_{s,1}}} \qquad \text{Eq.2-7}$$

To calculate the sorptivity ratio based on equation 2-6, the values of SHC shown in **Figure 2-7** are used. The saturation and the initial water content for concrete with different degree of damage are experimentally obtained and reported in **Table 2-2: The saturation water content, the initial water content, the wetting front suction head, and the normalized wetting front suction head for concrete with different degree of damage** to calculate the second term on the right hand side of equation 2-6.

Table 2-2: The saturation water content, the initial water content, the wetting front suction head, and the normalized wetting front suction head for concrete with different degree of damage

Damage (%)	θ_s [mm^3/mm^3]	θ_i [mm^3/mm^3]	ψ_f [$cm - H_2O$]	$\frac{\psi_{f,2}}{\psi_{f,1}}$
0	0.134	$3.14x10^{-3}$	$34.55x10^3$	1.00
10.1	0.149	$3.75\ x10^{-3}$	$38.38\ x10^3$	1.11
21.2	0.162	$4.15\ x10^{-3}$	$35.64\ x10^3$	1.03
28.6	0.169	$3.25\ x10^{-3}$	$41.45\ x10^3$	1.20
36.3	0.178	$3.13\ x10^{-3}$	$34.83\ x10^3$	1.01
47.2	0.191	$3.15\ x10^{-3}$	$36.97\ x10^3$	1.07

The value of ψ_f is given by equation 2-8 (for derivation see Neuman 1976)

$$\psi_f = \int_0^{\psi_i} k_r(\psi) d\psi \qquad \text{Eq.2-8}$$

where ψ is pressure head , ψ_i is the pressure head at the initial water content, and k_r is the relative hydraulic conductivity which can be described k_r using van Genuchten (Van Genuchten 1980) or Brooks and Cory (1964) models. Both models require the desorption isotherm that are provided in **Figure 2-9**. In general, ψ_i can be considered as infinity ($\psi_i = \infty$) since the initial pressure head of material is very large (Charbeneau 2006). In this work, Brooks and Cory model is used. The pressure head values were calculated from the relative humidity values in the desorption isotherm (Pour-Ghaz 2011). The Brooks and Cory model was then used in Burdine equation (Charbeneau 2006) to calculate k_r. The expression for k_r was then used in equation 2-8 and the closed-from solution presented in equation 2-9 was obtained (Charbeneau 2006).

$$\psi_f = \frac{2 + 3\lambda}{1 + 3\lambda} \psi_b \qquad \text{Eq.2-9}$$

where λ and ψ_b are the Brooks and Cory model parameters. The values of these parameters are presented in **Table 2-3** for each degree of damage. Since values were obtained with a few data points in **Figure 2-9** the correlation coefficient for the model was rather low (approximately $R^2 = 0.85$).

Table 2-3: Computed values of the Brooks and Cory model for concrete with different degree of damage

	Degrees of Damage (D) [%]					
	0	10.1	21.2	28.6	36.3	47.2
$\psi_b(cm-H_2O)$	5.03 x10^4	5.60 x10^4	5.13 x10^4	6.04 x10^4	4.98 x10^4	5.32 x10^4
λ	0.559	0.566	0.525	0.559	0.500	0.520

Figure 2-1 illustrates the theoretical (based on equation 2-6 and equation 2-7) and experimental (from **Figure 2-8**b) sorption ratios as a function of degree of damage. It can be seen that the predictions of equation 2-6 and 2-7 are close – i.e., the effect of the last two factors on the right hand side of equation 2-6 is rather small. While at low damage levels the theoretically predicated values of sorptivity ratio are close to the experimentally obtained ratios, in general, the experimental theoretical ratios do not agree well. This indicates that SF model does not adequately capture the behaviour of the damaged concrete. This conjecture however, is based on the simplified SF model. Therefore, more accurate numerical modelling may be required for accurate modelling of unsaturated flow in damaged concrete (Syml et al. 2014). In the next section conceptual models are developed to better describe the experimental observations using analytical models.

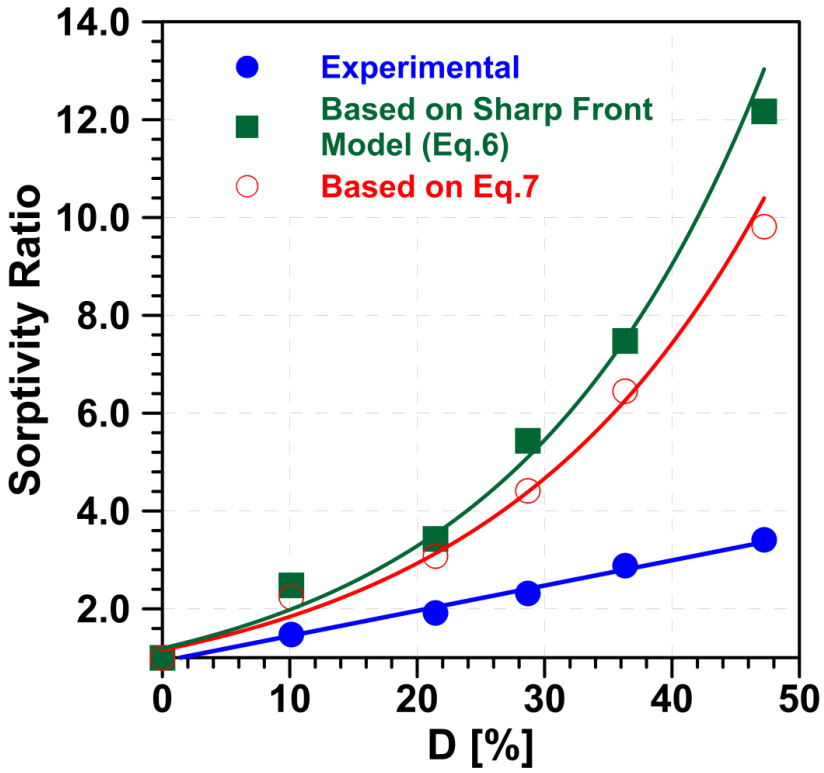

Figure 2-11: Comparison of experimentally obtained sorptivity ratios with the sorptivity ratios calculated based on sharp front theory using Eqs. (6) and (7)

2.5.3 Conceptual damage models

The authors propose new conceptual models that are based on the definition of damage in damage mechanics and fluid transport to describe the effect of damage on SHC, electrical resistivity, and water absorption. These models are based on an idealized damaged porous material shown in **Figure 2-12** with a unit cross sectional area (for simplicity assume $w = 1, d = 1$) and $\mathcal{N}$ idealized parallel plate cracks with an average crack width of $\langle H \rangle$ that are equally spaced throughout the materials with an average crack spacing of $\bar{b}$.

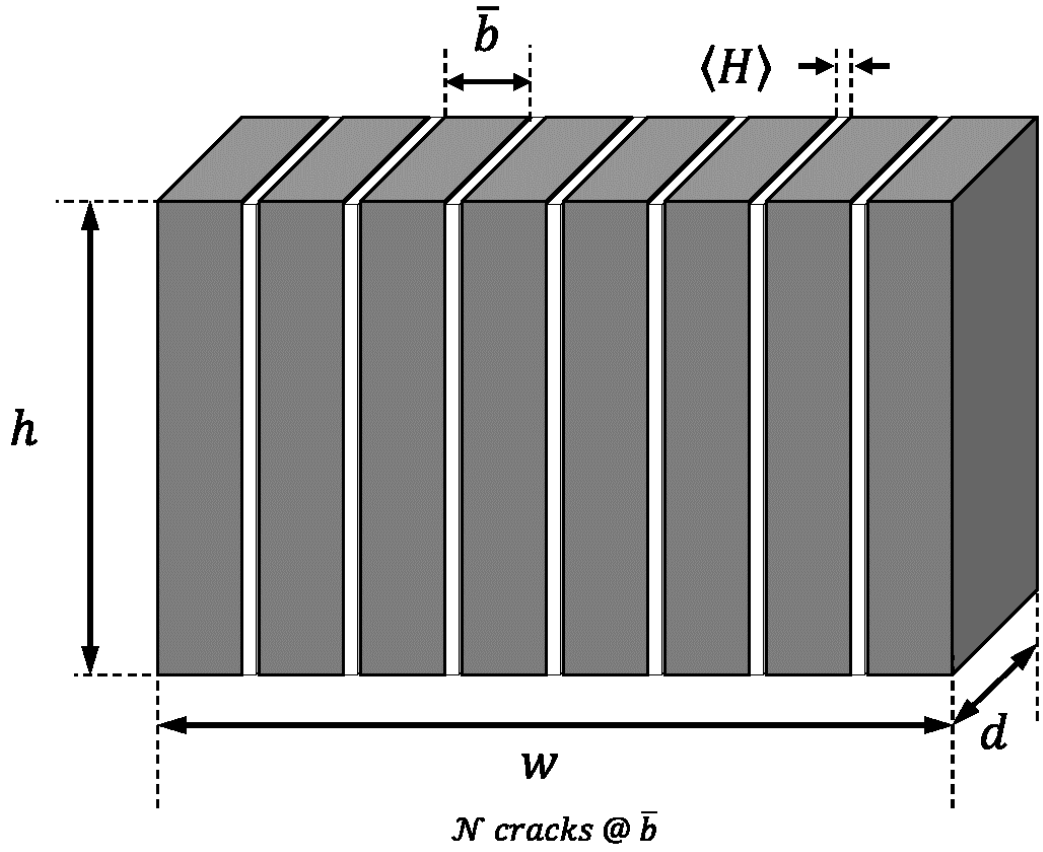

Figure 2-12: Schematic illustration of an idealized damaged porous material with unit cross section ($\mathbf{w}.\mathbf{d} = \mathbf{1}$) and $\boldsymbol{\mathcal{N}}$ idealized parallel plate cracks with an average crack width of $\langle \mathbf{H} \rangle$ that are equally spaced throughout the material with an average crack spacing of $\bar{\mathbf{b}}$.

In classical damage mechanics, damage (D) is defined as the area ratio of the discontinuities to the total area of the materials (Lemaitre and Lippmann 1996).

$$D = \frac{\text{area of discontinuities}}{w.d} = \frac{\mathcal{N}(\langle H \rangle . d)}{w.d} = \mathcal{N}\langle H \rangle \qquad \text{Eq.1-10}$$

Equation 2-10 indicates that damage increases with number of cracks and with average crack width. The results of acoustic emission in **Figure 2-3**b shows that the number of newly formed

cracks decreases at the later freeze-thaw cycles however damage continues to increase (**Figure 2-3**a). According to equation 2-10, therefore, at later freeze-thaw cycles where $\mathcal{N}$ does not increase significantly, the average crack width, $\langle H \rangle$, should increase.

Alternately, the damage parameter can be expressed by $D = \langle H \rangle / \bar{b}$ where in deriving this expression it is assumed that the average crack width is significantly smaller than the average crack spacing (i.e., $\langle H \rangle \ll \bar{b}$) and a large number of cracks (i.e., $\mathcal{N} + 1 \approx \mathcal{N}$) exists in the materials. Using the schematic illustration in **Figure 2-12**, the volume fraction of cracks, $f_f = \mathcal{N}\langle H \rangle$, and the volume fraction of undamaged concrete matrix $f_m = 1 - \mathcal{N}\langle H \rangle$ is obtained.

2.5.3.1 The effect of damage on saturated hydraulic conductivity

The effect of cracks on SHC can be described by a simple composite model

$$K = f_m K_o + f_f K_f \qquad \text{Eq.2-11}$$

where K_o is the SHC of the undamaged concrete matrix, $K_f = \frac{\rho g}{12\mu}\langle H \rangle^2$ is the parallel plate fracture hydraulic conductivity (Witherspoon et al. 1980), ρ is the density of the fluid, g is the gravitational acceleration, and μ is the viscosity of fluid. By substituting the volume fraction of cracks ($f_f = \mathcal{N}\langle H \rangle$) and undamaged matrix ($f_m = 1 - \mathcal{N}\langle H \rangle$), equation 2-12 is obtained:

$$K = (1 - \mathcal{N}\langle H \rangle)K_o + \mathcal{N}\langle H \rangle \left\{ \frac{\rho g}{12\mu} \langle H \rangle^2 \right\} = (1 - D)K_o + \bar{C}_1 \, D \, \langle H \rangle^2 \qquad \text{Eq.2-12}$$

where $\bar{C}_1 = \frac{\rho g}{12\mu}$ is a constant. Equation 2-12 clearly illustrates the importance of crack width on SHC. The results of acoustic emission along with equation 2-10 suggest that crack width increases at the later stages of damage due to freeze-thaw. Therefore equation 2-12 suggests that SHC of damaged material should initially increase linearly with damage (when $\langle H \rangle$ is small) and then the rate of increase of SHC should increase rapidly when $\langle H \rangle$ becomes larger. This is observed in **Figure 2-7** where, for example, with increase of damage from 36.3% (fourth cycle) to 46.2% (fifth cycle), the SHC increases drastically. While this is the largest increment of increase in SHC, the results of the acoustic emission test (**Figure 2-3**b) shows that the least number of events occur between the fourth and fifth cycle emphasizing the effect of crack width. Alternately, the increment of increase of SHC from zero to 10.1% damage is the smallest while the number of acoustic emission events is the largest.

2.5.3.2 The effect of damage on electrical resistivity

The overall conductivity (inverse of resistivity) of the concrete can be expressed by a simple composite (rule of mixtures) model (Weiss 1999, Rajabipour 2006). The rule of mixture has been used as an approximate model to describe the conductivity of cement paste containing cracks (Akhavan et al. 2012; Akhavan and Rajabipour 2013). The rule of mixtures is utilized here to estimate of the overall conductivity of damage concrete, $\bar{\sigma}$, based on the conductivity

of the undamaged concrete matrix, σ_m, and average conductivity of a crack, $\langle\sigma_f\rangle$ by equation 2-13:

$$\frac{\bar{\sigma}}{\sigma_m} = f_m + f_f \frac{\langle\sigma_f\rangle}{\sigma_m} \qquad \text{Eq.2-13}$$

In saturated systems, $\langle\sigma_f\rangle$ may be approximated by the conductivity of the pore solution, σ_o, and some factor to account for tortuosity of the cracks. As a first order approximation $\langle\sigma_f\rangle/\sigma_m = \sigma_o/\sigma_m$ can be considered as the formation factor, F (Rajabipour 2006). Using $f_f = D = \mathcal{N}\langle H\rangle$, equation 2-13 can be rewritten

$$\frac{\bar{\sigma}}{\sigma_m} = 1 + D\left(\frac{\langle\sigma_f\rangle}{\sigma_m} - 1\right) \qquad \text{Eq.2-14}$$

Inverse of equation 2-14 provides the resistivity ratio illustrated in **Figure 2-6**. Since $\langle\sigma_f\rangle/\sigma_m > 1$, equation 2-14 indicates that the conductivity ratio increases linearly with damage, or equivalently, the resistivity ratio decreases linearly with damage. The conceptual model in equation 2-14 approximates the "slight" bilinear behaviour in **Figure 2-6** with a linear model which holds well for damage higher than 10.1%. If a more advanced nonlinear model is used (e.g., self-consistent, differential effective medium, or Hashin-Shtrikman; see for example Neithalath (2004), Rajabipour (2006) and Torquato (2002)), one may be able to capture the bilinear behaviour observed more closely.

2.5.3.3 The effect of damage on capillary sorption

The volumetric flow rate, Q, in a single parallel plate crack can be expressed by (Witherspoon et al. 1980):

$$Q = \bar{C}_1 \frac{P_c}{h} \langle H \rangle^3 \qquad \text{Eq.2-15}$$

where $P_c = \frac{2\gamma \cos\theta}{\langle H \rangle}$ represent the capillary suction pressure within the crack with the assumption of ($\langle H \rangle \ll d$ in **Figure 2-12**) , γ is the surface tension of the fluid, θ is the contact angle, and h is the height of material (**Figure 2-12**). Since $Q = dV/dt$ where V is the total volume of fluid entering into a crack, equation 2-15 can be integrated with respect to time to obtain the total volume of fluid entering into a single crack at time t as $V = \langle H \rangle^{3/2} \bar{C}_2 \sqrt{t}$ (Pour-Ghaz 2014). The total volume of water, V_T, entering into N-cracks therefore can be expressed as

$$V_T = \mathcal{N} \langle H \rangle^{3/2} \bar{C}_2 \sqrt{t} = \left[D \langle H \rangle^{1/2} \bar{C}_2 \right] \sqrt{t} \qquad \text{Eq.2-16}$$

where $\bar{C}_2 = \frac{\rho g \gamma \cos\theta}{6\mu}$ is a constant. Equation 2-16 indicates that the capillary water absorption into the parallel plate cracks is linear with square root of time and therefore the term in square brackets shows the initial sorptivity which increases with damage. Also, the effect of crack

width, $\langle H \rangle$, in capillary sorption is less significant as compared to its effect on SHC (equation 2-12) – note the exponent of $\langle H \rangle$. This explains the deviation of equations 2-6 and 2-7 (that are based SF model) from the observed linear increase in initial sorptivity in **Figure 2-11**: The SF model does not account for the contribution of crack width especially the contribution of large cracks.

To quantitatively use the proposed models, an estimate of average crack width is required which may be obtained, for example, using SEM imaging. In the absence of such information, these models can provide only qualitative insight to the experimental data.

2.6 Cluster Explanation

In this section we use the concept of percolation to describe the effect of micro-cracks on water absorption, electrical resistivity, and saturated hydraulic conductivity (permeability). The schematic illustration in **Figure 2-13** shows a simple two-dimensional cluster of micro-cracks that connects the bottom of the specimen to the top of the specimen. One can assume that the cluster is made of a network of resistors that facilitates flow of electrical current (the same analogy can be made for flow of water through a network of pipe segments), the path in the cluster that conducts the current between the bottom and top of the specimen is referred to as the backbone. In **Figure 2-13**, thick lines (red solid and dashed) show the backbone of the cluster. Loops are portion of the backbone that include more than one path between the two ends. The dashed lines in the backbone illustrate the loops. Loops contribute to conduction and with increasing number of loops, more current can flow through the backbone. In **Figure 2-13**

the thin (black lines) show the dangling ends. Dangling ends are the "dead-ends" and they do not contribute to the current flow (Stanley 1977).

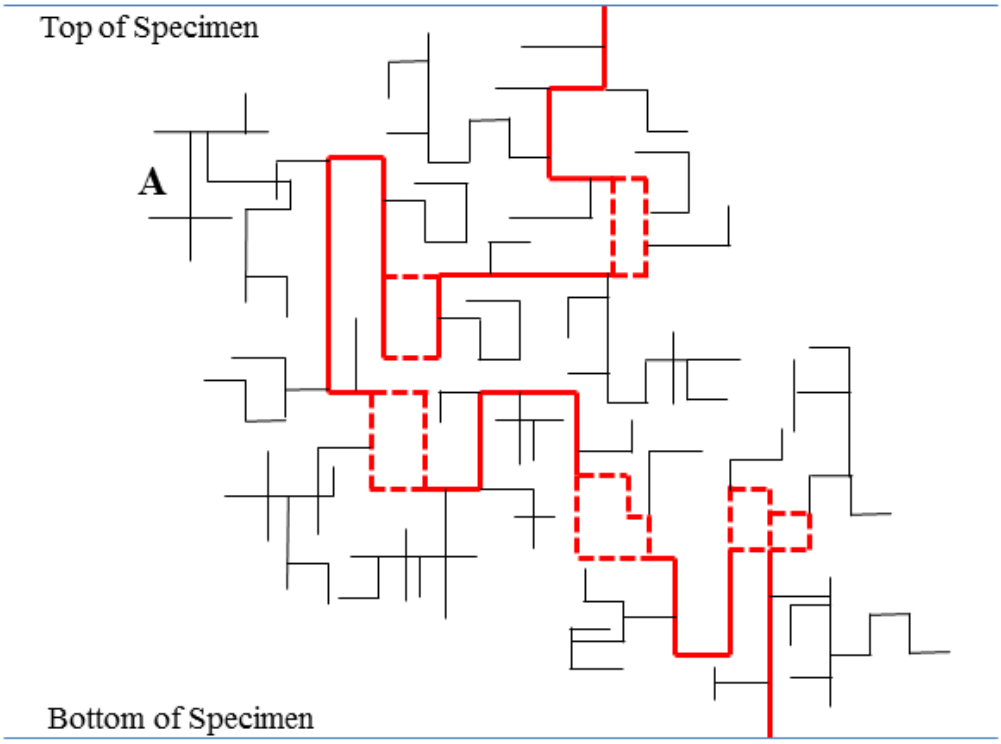

Figure 2-13: Schematic illustration of a network of micro-cracks after percolation. Thick lines (red solid and dashed lines) show the backbone of the cluster. Thin lines (black lines) illustrate the dangling ends. Dashed lines illustrate the loops of the backbone (after Stanley 1977).

When damage occurs within the specimen (e.g., due to freeze-thaw), clusters of micro-cracks forms. At a certain degree of damage (i.e., critical degree of damage), these clusters form a large enough cluster that percolates the entire system (percolating cluster) and connects the bottom of the specimen to the top of the specimen (i.e., percolation occurs). After the percolation, the backbone of the percolating cluster is the main path of electrical and hydraulic

flow. As the degree of damage increases, the number of dangling ends increases. The dangling ends merge and form more loops in the backbone, resulting in strengthening the conduction in backbone.

The percolating cluster, contributes to the increase of water sorptivity. The micro-cracks of the cluster act as capillary tubes and absorb water by capillary suction resulting in increased initial sorptivity. The dangling ends in the cluster also act as capillary tubes contributing to increase of water absorption. In addition, the dangling ends, facilitate access to the capillary pores that are far from the water absorbing surface (e.g., bottom of the specimen). For example, the dangling end A in **Figure 2-13** provides rapid access to the capillary pores in its vicinity while these pores are far from the bottom of the specimen (assuming the water is absorbed from the bottom of the specimen). The percolating cluster will provide access to the air-filled pores and therefore some of the air-filled pores will be filled with water during the initial sorption period; and therefore, the rate of water absorption decreases during the secondary sorption period. This phenomenological explanation is in line with the effect of damage on the initial and secondary sorptivity that was discussed in section 2.5.1 and shown schematically in **Figure 2-10**.

It is well known that cement paste is the most conductive phase in concrete and the pore solution is the main contributor to electrical conductivity of the cement paste. Because of the electrical conductivity of the cement paste, in damaged concrete, the electrical current flows through the cement paste as well as the percolating cluster. In saturated systems, the electrical conductivity of the cluster is higher than the electrical conductivity of damaged cement paste

is higher than the electrical conductivity of the undamaged cement paste due to the larger size of micro-cracks, less tortuosity of the micro-cracks, and more connectivity of the micro-cracks as compared to capillary pores. However, due to the contribution of the cement paste to electrical conductivity, the contribution of the micro-cracks to electrical conductivity is less pronounced as compared to the contribution of the cracks to saturated hydraulic conductivity (permeability). As the percolating cluster forms in the concrete, the electrical conductivity of the concrete increases. Due to the contribution of the cement paste itself to the conductivity (background conductivity), the systems containing clusters that are close to the critical percolating cluster size will also behave similar to the systems containing a percolating cluster and therefore, it is expected that "percolated behavior" for electrical conductivity to occur with smaller cluster size (smaller degree of damage).

The backbone of the cluster is the main contributor to the electrical conductivity. The dangling ends have minimal contribution to electrical conductivity since the electrical current will preferentially flow through the backbone. Loops contribute to electrical conduction and decrease the electrical resistivity of the system. The contribution of the loops, however, only incrementally improves the conduction within the backbone since they act as parallel resistors at some segments of the backbone. Therefore, after formation of the backbone, the rate of decrease of electrical resistivity with damage decreases. The observed bi-linear decrease of electrical resistivity in **Figure 2-6** therefore may be explained by this simple percolation model. It should be noted that, in saturated systems, since the cracks are highly conductive, the increase of crack width may also contribute to enhanced electrical conductivity.

The backbone is the main contributor to hydraulic conductivity, however, the dangling ends do not contribute to the hydraulic conduction. Another main contributing factor to hydraulic conduction is the crack width. The effect of crack width however is not considered in the percolation model shown in Figure 2-13. It is well known that the hydraulic conductivity of a crack increases linearly with square of crack aperture. Therefore, the rate of increase of saturated hydraulic conductivity should be higher than the rate of increase of electrical conductivity (decrease of electrical resistivity) because of the contribution of crack width.

Based on the discussion above, while simple percolation model can phenomenologically explain the effect of cracks on electrical conductivity, sorptivity, and saturated hydraulic conductivity, it is rather difficult to identify a single critical degree of damage that can describe the entire behavior of the system.

2.7 Chapter Conclusions

In the present work, the effect of damage due to freeze-thaw on saturated and unsaturated moisture transport as well as electrical properties of concrete was experimentally investigated. The following summarizes the findings of this study.

The initial sorptivity increases linearly with degree of damage because (i) cracks act as capillary tubes that absorb water rapidly, (ii) cracks provide access to capillary pores within the specimen and away from the exposed surface (preferential flow paths), and (iii) cracks provide access to the larger air-filled pores, and therefore, some of these air-filled voids are filled with water during the initial sorption period resulting in higher initial sorption rate.

The secondary sorptivity initially decreases with damage, and then remains almost constant because cracks provide access to the larger air-filled voids and therefore some of these air-filled voids are filled with water during the initial sorption period leaving a smaller fraction of these air-filled voids empty for the secondary sorption period.

The results of passive acoustic emission, scanning electron microscope, saturated hydraulic conductivity, and a simple damage mechanics based model collectively indicate that initially a larger number of cracks develop within the material with freeze-thaw loading. At the later cycles of freeze-thaw, a smaller number of cracks develop, but the average crack width increases. This gives rise to exponential increase of saturated hydraulic conductivity with degree of damage.

The Electrical resistivity shows a slight bilinear decreased with damage: The electrical resistivity initially decreases with a higher rate due to the formation of cracks and then the rate of decrease of resistivity decreases with further damage development since in the later stages the connectivity is enhanced but smaller number of new cracks are developed. The conceptual damage model developed approximates the bilinear decrease with a linear decrease.

In general, damage in the form of distributed cracking increases the rate of moisture transport. The extent to which damage affects the rate of transport is dependent on the mechanism of transport. It appears that saturated hydraulic conductivity is much more sensitive parameter to damage as compared to sorption and electrical resistivity. The conceptual model developed supports this observation by showing the higher dependence of saturated hydraulic conductivity to crack width.

3. A Comparison of Methods to Evaluate Mass Transport in Damaged Mortar

3.1 Introduction

Distributed micro-cracking, referred to as damage hereafter, is a common problem in concrete structures. Damage may result from different deteriorations, such as freeze-thaw and alkali silica reaction, and adversely affects the service life of structures. In order to account for the effect of damage on the service life, its effect on mass transport needs to be quantified. Different methods have been developed to measure the transport properties of cement-based materials. These methods provide a different measure of the effect of damage on mass transport properties (Ghasemzadeh and Pour-Ghaz 2014). In this research the following question are posed: How do different measurement techniques show the effect of damage on mass transport, and which transport measurement method is more sensitive to the presence of damage? To this end, it is experimentally compared different mass transport measurement techniques.

The effect of damage and discrete cracking on the transport properties of cement-based materials has been studied in numerous investigations (Ghasemzadeh and Pour-Ghaz (2014), Samaha and Kenneth (1992), Aldea et al. (1999), Zhou et al. (2012), Akhavan et al. (2012), Zhou et al. (2012), Picandet et al. (2009), Yang et al. (2006), Torrijos et al. (2010), Wang and Ueda (2014), M'Jahad et al. (2014), Rashetnia et al. (2015), Gerard and Marchand (2000), De la Varga et al. (2014), Bentz et al. (2013), Fagerlund (2012), Jacobsen et al. (1996), Langton (2012), Pour-Ghaz et al. (2009a), Pour-Ghaz et al. (2009b), Reinhardt and Jooss (2003)).

Different measurement methods have been used in these works and they all show that damage and cracking increases the mass transport. **Table 3-1** summarizes previous works that studied the effect of discrete cracking and damage on transport properties of cement-based materials. These works, in **Table 3-1**, are classified based on the type of cracking: discrete cracking or damage. Three conclusions can be drawn from **Table 3-1**. First, the effect of discrete cracking is studied in more detail as compared to the effect of damage. Second, the effect of damage has been rarely interpreted in the light of transport mechanisms used in the measurement methods. Finally, it is unclear as which transport mechanism, and subsequently which measurement method, is more sensitive to the presence of damage.

In this study, damage was induced by freeze-thaw loading in mortar specimens. Active acoustic emission (AE) was used to quantify the degree of damage. Passive AE was also used to monitor damage formation during the freeze-thaw cycles. Electrical Impedance Spectroscopy (EIS) and four-electrode Wenner methods were used to measure the bulk and surface electrical resistivity, respectively. Rapid Chloride Penetration Test (RCPT) measurement was also used. Soprtion, drying, air permeability, water permeability and desorption isotherm measurements were also carried out.

In the following sections, the materials and methods used are described. Then, the results are presented and discussed. Finally, the conclusions of this study are presented.

Table 3-1: Summary of previous studies on mass transport in cracked cement-based materials

Study	Mechanism of cracking	Material	Measurement methods	Highlights
Discrete cracking				
Samaha and Hover (1992)[2]	Compressive load-induced cracking	Concrete Mortar	RCPT and Water absorption	The water absorption and chloride ion penetration differently reflect the effect of damage on transport properties of concrete as load levels increases.
Aldea et al. (1999) [3]	Split tensile load-induced cracking	Concrete	Water and chloride permeability	Water permeability is a more sensitive parameter, than chloride permeability, to crack width.
Chunsheng et al. (2012)[4]	Compressive load-induced cracking	Concrete	Air permeability, sorptivity and electrical resistivity	While gas permeability correlated with damage, sorptivity and electrical resistivity correlated with open porosity – the connected pores available for fluid flow.
Akhavan et al. (2012) [5]	Split tensile load-induced cracking	Mortar	Water permeability and image analysis on cracks	Permeability is a function of square of crack width. Crack tortuosity and roughness reduce the permeability.
Chunsheng et al. (2012)[6]	Compressive load-induced cracking	Concrete	Water absorption, gas permeability, electrical resistivity and crack geometry analysis	Crack geometry (i.e., length, orientation, and connectivity) and crack density have strong impact on transport properties.
Picandet et al. (2009) [7]	Split tensile load-induced cracking	Concrete	Gas and water permeability	Cracks provide direct path to convey a large portion of flow, with no influence from saturation degree. Permeability could be considered as an intrinsic parameter to evaluate the global effect of load-induced damage on concrete durability.
Distributed cracking				
Yang et al. (2006) [8]	Freeze-thaw loading	Concrete	Water absorption and electrical resistivity	Sorptivity increases linearly with damage; electrical conductivity increases in a bilinear fashion.
Torrijos et al. (2010) [9]	Low RH with high temperature and ASR	Concrete	Water absorption and water permeability	Depending on the main transport mechanism, crack width, type of cracks and crack density differently affect the transport properties.
Wang and Ueda (2014) [10]	Freeze-thaw loading	Concrete	Water absorption and chloride ion penetration	Water absorption and chloride penetration is faster in damaged specimens compared with undamaged concrete. The total amount of absorbed water in damaged specimens is more than undamaged specimens.
Jahad et al. (2014) [11]	Freeze-thaw loading	Concrete	Mercury intrusion porosimetry, desorption isotherm, relative gas permeability, and gas breakthrough pressure	Gas breakthrough pressure seems to be a more sensitive indicator of damage than other studied methods.
Ghasemzadeh and Pour-Ghaz (2014) [1]	Freeze-thaw loading	Concrete	Water absorption, electrical resistivity, desorption isotherm and saturated hydraulic conductivity	The rate of moisture transport increases with damage. The extent to which damage affects the rate of transport is dependent on the mechanism of transport. Saturated hydraulic conductivity is much more sensitive parameter to damage due to the higher dependence of saturated hydraulic conductivity to crack width.

3.2 Material and Methods

3.2.1 Materials, mixture proportioning, and specimen preparation

Ordinary Portland cement Type I and river sand with a fineness modulus of 2.65 were used. The mortar mixture had a water-to-cement ratio (w/c) of 0.42. The amount of cement, fine aggregate, and water reducer in the mixture were 609 kg/m^3, 1466 kg/m^3, and 0.50kg/m^3, respectively. The mortar was made according to ASTM C192-07.

After casting mortar in 102 mm x 204 mm cylindrical molds, all of the samples were kept sealed for 24 hours. The samples were then demolded and cut into appropriate geometries (for different experiments as shown in **Table 3-2**) using a diamond-tipped wet saw. The top and bottom ends of the cylindrical specimens (roughly 25 mm) were not used to minimize possible end-effects. All of the specimens were cured in lime-saturated water at 25±1ºC for 18 months after cutting.

3.2.2 Freeze-thaw testing

Freeze-thaw loading was performed in an air-cooled chamber. Each cycle was 4 hours including a cooling period from 21˚C to -35˚C, and a heating period back to 21˚C. The cooling and heating periods included two ramps as well as two constant temperature parts (temperature profile shown **Figure 3-1**). The constant temperature parts were designed to decrease the temperature gradient across the samples. The core temperature of specimens was monitored using embedded thermocouples. To keep the specimens saturated, during the freeze-thaw

testing, they were wrapped in a water saturated cloth and then were sealed with a thin plastic sheet. A total of 25 freeze-thaw cycles were used and specimens were removed from the chamber for testing after 2, 5, 10, 15, and 25 cycles.

3.2.3 Methods

A number of tests based on different mechanisms were performed. In **Table 3-2**, the number and the dimensions of the specimens used in each are provided. Detailed description of the testing equipment and processes are provided below.

Table 3-2: List of test methods and the number of specimens and their dimensions

Method	**Specimen details**		
	Number of Specimens*	**Diameter [mm]**	**Thickness [mm]**
Acoustic Emission (AE)	3	102	25&50
Rapid Chloride Penetration Test (RCPT)	4	102	50
Electrochemical Impedance Spectroscopy (EIS)	4	102	50
Surface Resistivity (SR)	3	102	204
Sorptivity	2	102	25
Drying	2	102	50
Air permeability	3	102	25
Water Permeability	4	102	25
Desorption isotherm	2	Specimens with 0.50-1.5 mm thick and 50-100 mg in weight**	

*Indicates the number of samples for each degree of damage
**Specimens were cut from 25x102 mm disk

3.2.3.1 Acoustic Emission

Active AE was used to monitor damage in mortar specimens at the end of each freeze-thaw cycles and passive AE was used to continuously monitor damage during the freeze-thaw cycles. AE sensors with a peak frequency of 375 kHz were used. Flat surfaces for mounting the sensors were created by trimming the side surfaces of specimen tangent to the perimeter. AE sensors were coupled to the specimen using vacuum grease. Specimens were placed on a layer of acoustic mat resting on a rigid stainless steel frame which was isolated from the chamber to minimize vibration and noise. A stainless steel rod was also used as a reference specimen to monitor the environmental noise during the test and to ensure that the coupling agent did not degrade during freeze-thaw. Further detailed information regarding the application of AE system on damage monitoring in cement-based materials can be found elsewhere (Ghasemzadeh and Pour-Ghaz (2014), Rashetnia et al. (2015), Kim and Weiss (2003), Li et al. (2011), and Farnam et al. (2014)).

3.2.3.2 Rapid Chloride Penetration Test (RCPT)

Rapid chloride penetration test (RCPT) was carried out according to the ASTM C1202-10.

3.2.3.3 Surface Resistivity

Surface resistivity was measured using a four-electrode Wenner probe on 102 mm x 204 mm cylinders. The equipment used works with a 40 Hz alternate current (AC). Before measurements, specimens were kept in a large water container until they reached to thermal

equilibrium with the ambient temperature (approximately 24 hrs). After each measurement, specimens were placed back in chamber to undergo more freeze-thaw cycles.

3.2.3.4 Electrical Resistivity

Bulk electrical resistivity was measured on 50 mm thick disk specimens, using EIS, after a given number of freeze-thaw cycles. Three different arrangements were used in measuring bulk electrical resistivity. First, the specimens were sandwiched between two stainless steel plate electrodes; to improve electrode contact, a copper-based conductive gel was used and measurement was performed using EIS ((Pour-Ghaz (2011), Spragg et al. (2011)). Second, specimens were installed in a RCPT cell and EIS was used to measure the bulk resistivity (Akhavan and Rajabipour 2011). Finally, the initial current from the RCPT measurements were utilized to measure the bulk electrical resistivity (Snyder et al. 2000). To provide a better comparison, the same specimens were used in all three methods for each degree of damage. EIS measurements were performed with amplitudes of 500 mV over the frequency range of 1 Hz to 1 MHz. Before measurements, specimens were kept in a large water container until they reach to thermal equilibrium with the ambient temperature (6-8 hours).

3.2.3.5 Sorptivity

Water absorption was carried out following ASTM C1585-13 on 25 mm thick disks and experiment was carried out up to 150 days.

3.2.3.6 Drying test

The drying rate of mortar specimens with different degree of damage were measured by monitoring mass loss in a chamber with a relative humidity of 50±5 % at 23±1°C. Prior to weight loss measurements, specimens were saturated under high vacuum (0.015 mm Mercury). Weight loss was continuously recorded with one minute intervals for the first 10 hrs and then the measurements were continued daily, up to 7 days, and weekly up to 60 days. Only one surface of the sample was subjected to drying and all other surfaces were sealed.

3.2.3.7 Air permeability

The air permeability of mortar specimens were measured using the method in (Schonlin and Hilsdorf (1988), Dilek and Leming (2008)). The vacuum pressure was induced using a vacuum pump. A vacuum pressure of 736 mm Hg was induced and then the time to reach to vacuum pressure at 635 mm Hg was recorded. Depending on the permeability of the specimens, measurements were completed in 1–30 min. To ensure air tightness of the equipment seals, tests were performed on a 25 mm thick aluminium disk and no pressure decay observed.

The circumference surface of the specimens was coated with a rapid-setting epoxy to induce one-dimensional air flow through the face of the disk. All the specimens were dried in an oven at 50°C for 48 hrs before the measurements. This essentially resulted in complete drying eliminating the effect of initial moisture content of the samples while minimizing additional

cracking (Villani et al. 2014). A thin strip of soft clay was also used to seal the chamber to the face of specimen.

The Boyle-Marriotte law was used to calculate the air permeability assuming the specimen is a homogeneous porous material. Air permeability is calculated per Eq. 3-1 (Dilek and Leming 2008).

$$K_{(air)} = \frac{\left(P_f - P_i\right) V_s}{(\Delta t)\left(P_a - \frac{P_i + P_f}{2}\right)} \frac{L}{A} \qquad Eq.3-1$$

where $K_{(air)}$ is the air permeability index (m^2/s), P_i and P_f are the initial and final vacuum pressure in the chamber (Pa) respectively, V_s is the volume of vacuum chamber (m^3), Δt is the duration of measurement (s), P_a is the atmospheric pressure (Pa), L is the thickness of specimen (m), and A is the cross section of the specimen (m^2).

3.2.3.8 Water Permeability

Water permeability measurements were performed using in-house developed equipment. The details of water permeability equipment has discussed in previous chapter and in Ghasemzadeh and Pour-Ghaz (2014). Measurement was performed at 23±1°C.

3.2.3.9 Desorption Isotherm

The desorption isotherm of mortar specimens with different degrees of damage were measured using an automated vapour sorption analyzer. Measurements were performed at 23˚C. The specimen was equilibrated at 97.5% RH and the relative humidity was sequentially dropped from 97.5% to 0% RH, in 5% RH increments to 2.5% and then to zero RH. The sample was held at each RH step until it reached to equilibrium. Equilibrium was defined as a mass change less than 0.001 mg within 15 min (Pour-Ghaz et al. 2010). The specimens were 0.50-1.5 mm thick and 50-100 mg in weight. A full description of desorption isotherm experiment using automated sorption analyzer has been discussed in Pour-Ghaz et al. (2010), and Villani et al. (2014)).

3.3 Results and Discussion

3.3.1 Acoustic Emission

Figure 3-1 illustrates the peak amplitudes of the captured AE events during the freeze-thaw loading. **Figure 3-1**a and **Figure 3-1**b present the first and the last 5 cycles for 25 mm samples. **Figure 3-1**c shows the total number of AE hits in each cycle as a function of number of freeze-thaw cycles in samples with 25 mm thick. The same plots presenting the results for 50-mm thick samples are shown in **Figure 3-1**d, **Figure 3-1**e, and **Figure 3-1**f. In **Figure 3-1**c and **Figure 3-1**f a higher number of events are captured during the first few cycles as compared to the subsequent cycles, signifying that high number of cracks develops initially (Ghasemzadeh and Pour-Ghaz (2014), Li et al. (2011)).

Figure 3-2 shows the degree of damage measured with active acoustic emission (AE) after a given number of freeze-thaw cycles. The damage index (D) is calculated based on the wave travel time in damaged and undamaged specimens (Ghasemzadeh and Pour-Ghaz (2014)). In **Figure 3-2** results for specimens with 50 mm and 25 mm thickness are labelled by AE-50 and AE-25 respectively. A linear increase of damage with the number of freeze-thaw cycles is observed. Slightly higher damage is observed in 25-mm thick samples. This is in part a result of a lower core temperature in 25-mm thick disks as compared to 50-mm thick samples.

Note that while damage increases with the number of cycles in **Figure 3-2**, the number of AE events significantly decreases in the subsequent cycles (**Figure 3-1**c and **Figure 3-1**f) reflecting the reduction in the rate of development of new cracks. This observation is consistent with previous study by the authors which indicates that in later freeze-thaw cycles the average crack width increases with a higher rate as compared with the formation of new cracks. In fact, increase of degree of damage at higher damage levels can be mainly attributed to the increase in the crack width. An analytical model to describe this was previously presented in (Ghasemzadeh and Pour-Ghaz (2014)). In addition to increased crack width, crack density increases, resulting in crack percolation. Crack percolation results in a high degree of damage.

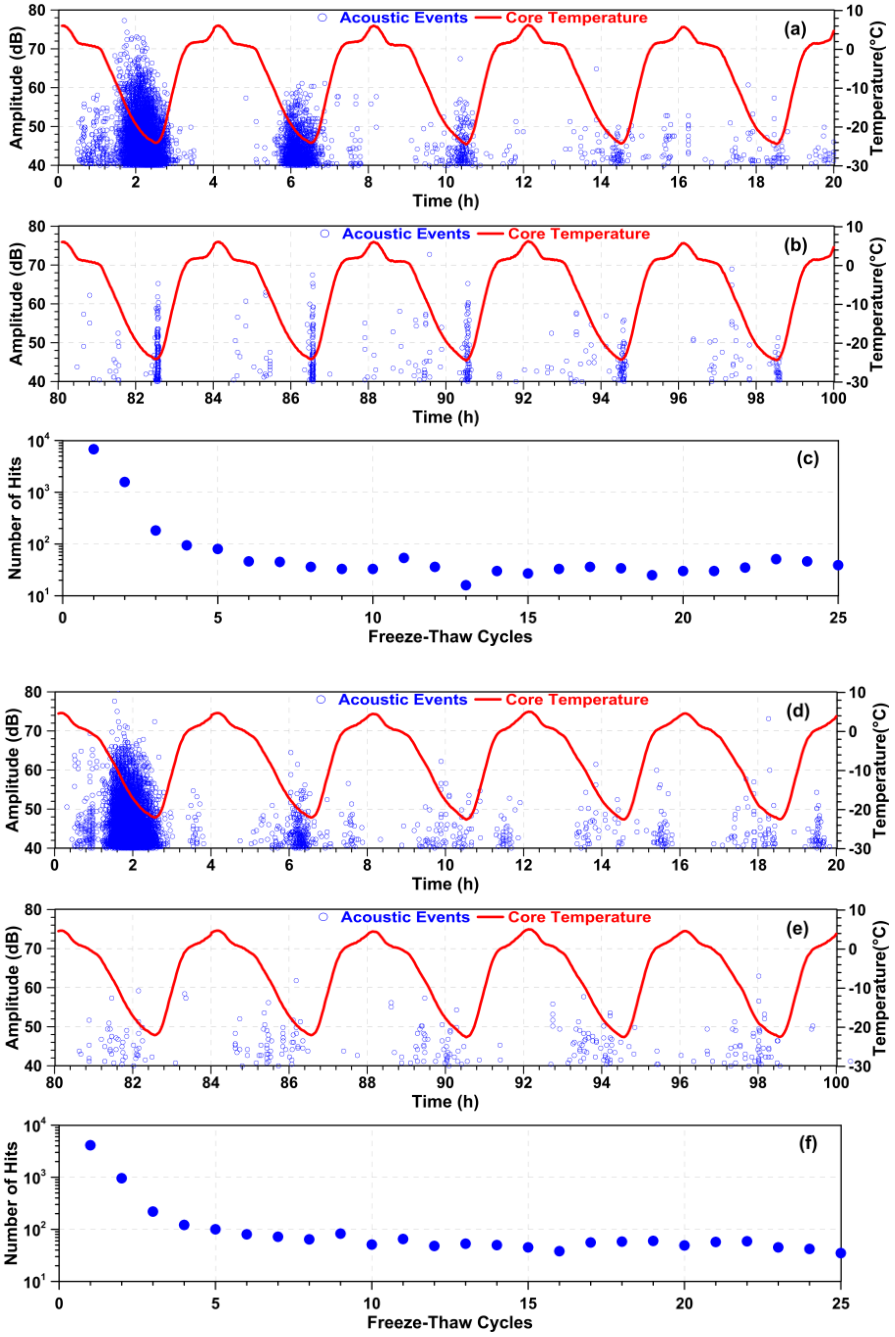

Figure 3-1: Damage formation during the freeze-thaw loading monitored by passive acoustic emission: (a) first 5 cycles in 25 mm sample, (b) last 5 cycles in 25 mm sample, (c) the total number of events in each freeze-thaw cycle in 25 mm sample, (d) first 5 cycles in 50 mm sample, (e) last 5 cycles in 50 mm sample, (f) the total number of events in each freeze-thaw cycle in 50 mm sample.

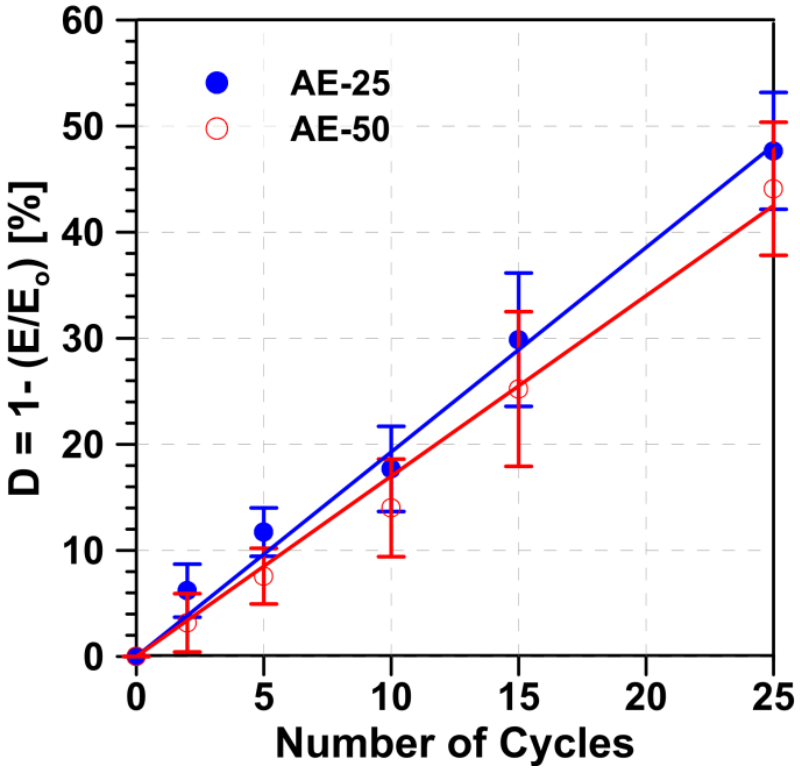

Figure 3-2: Damage measurement based on acoustic emission (AE)

3.3.2 Rapid Chloride Penetration Test (RCPT)

Figure 3-3 illustrates the results of RCPT for specimens with different degrees of damage. **Figure 3-3**a and **Figure 3-3**b show the current flow over time and the total charge passed (coulombs) in specimens with different degrees of damage, respectively. In **Figure 3-3**a while the current continuously increases over time at low level of damage, it initially increases and then decreases in specimens with higher level of damage. This reduction of current at later times affects the total charge passed in damaged specimens. In **Figure 3-3**b the total charge passed increases with damage, however, it reaches a plateau at high degrees of damage. The rather insignificant difference between the total charged passed from D=25.21% to D=44.09%

makes the reliability of RCPT questionable. There are three possible explanations for this observation. First, in the presence of high degree of damage, the chloride concentration reduces in the NaCl solution cell due to the transfer of high amount of chloride ions to the NaOH solution cell. This in turn reduces the amount of current transfer by chloride ions through the specimen. Second, the chloride concentration may be reduced in the system due to the chloride binding of hydration products (Spiesz and Brouwers 2012)). In the presence of high degree of damage, a higher amount of chloride ions can move into the specimen, thus increasing the chance of chloride binding, and thus, decreasing the amount of current transfer by chloride ions (Yuan et al. 2009). Third, during the chloride binding a portion of chloride ions can be replaced by the OH^- ions. Once OH^- ions are released, simultaneous diffusion and migration occurs and therefore OH^- ions could either move to the catholyte solution (NaCl solution) side through diffusion mechanism or to the anolyte solution (NaOH solution) side through the migration mechanism (Andrade 1993). The OH^- ions movement mechanism depends on the concentration of OH^- ions in the pore solution. According to the results in **Figure 3-3**, it seems that the OH^- ions movement mechanism changes into diffusion mechanism during the experiment in specimens with high level of damage, thus reducing the current passed through the specimen.

It should be also noted that specimens were kept 18 months in lime-saturated water and it could be assumed that cement particles were well hydrated. Therefore, healing of the cracks could not be a strong reason for current reduction of damaged specimens in **Figure 3-3**a.

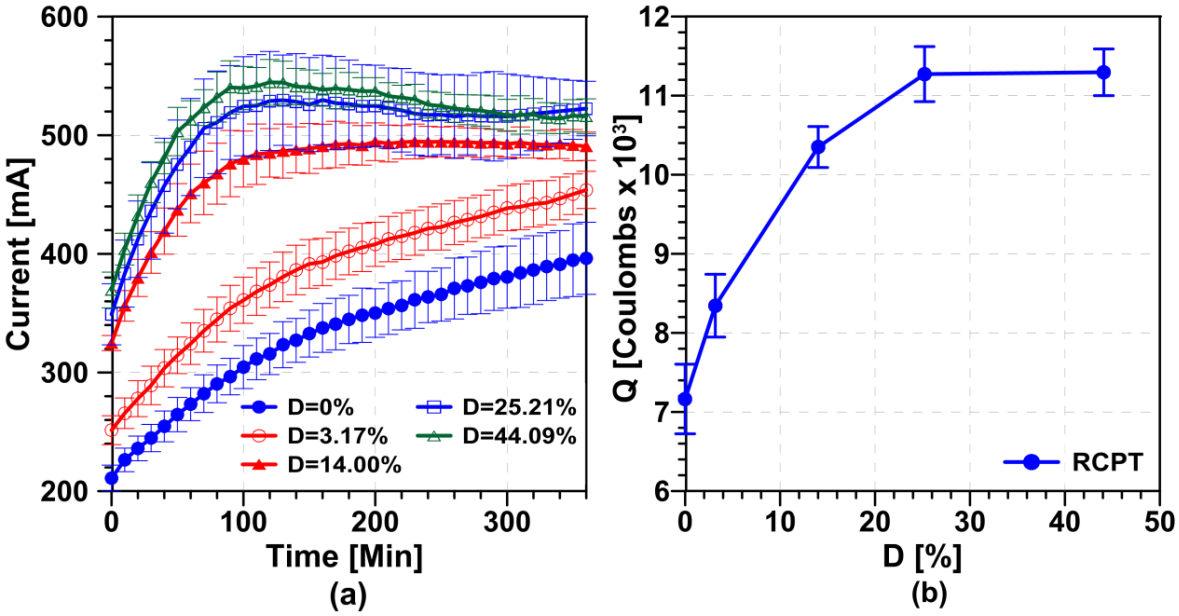

Figure 3-3: The results of Rapid chloride penetration test (RCPT): (a) transferred current during the RCPT, (b) change in total charge passed.

3.3.3 Electrical resistivity

Figure 3-4a illustrates the normalized bulk resistivity of mortar specimens. The results are normalized to the initial resistivity (undamaged value). In all three sets of measurement the normalized bulk resistivity decreases with damage. Resistivity decreases with a high rate initially in which initial cracks in specimens form due to the freeze-thaw loading. With further increase of damage the electrical resistivity decreases with a lower rate. The results obtained using stainless steel plates show a lower resistivity at all damage levels as compared to other

methods. This is mainly due to reduce contact impedance when RCPT cells are used in measurements (Halaji et al. 2015).

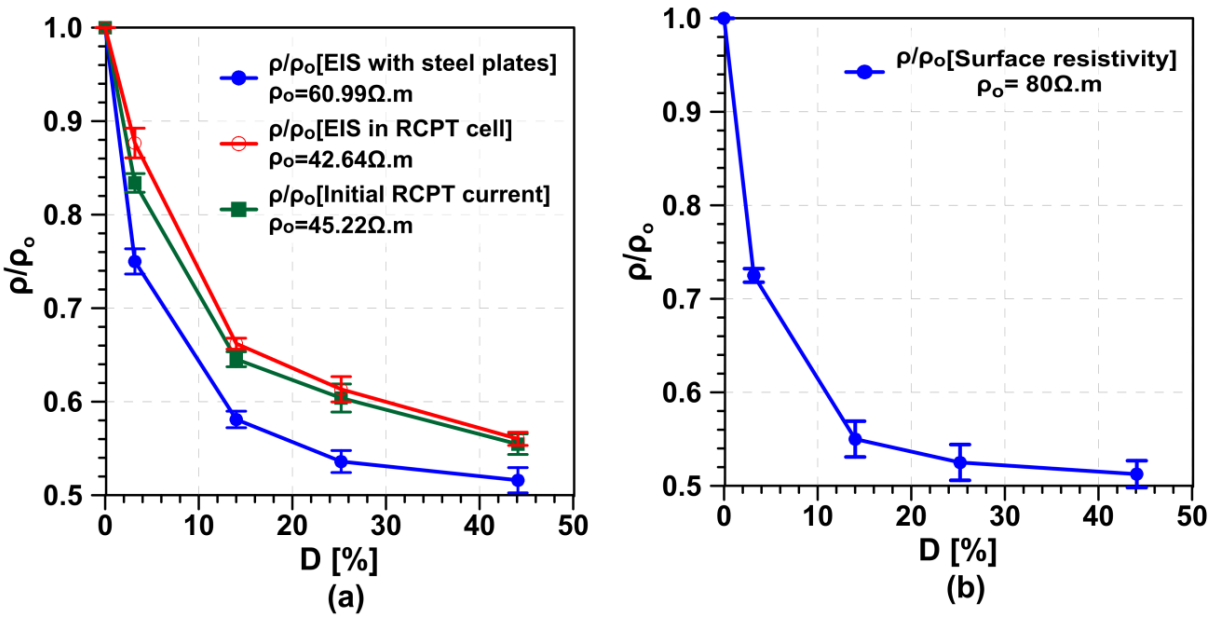

Figure 3-4: (a) Normalized bulk electrical resistivity, to the resistivity of undamaged mortar, of mortar specimens, (b) normalized surface resistivity as a function of damage.

Figure 3-4b illustrates the normalized change of surface resistivity with damage. The measurements were performed on 102 mm x 204 mm cylinders (Spragg et al. 2011). It should be noted that the degrees of damage were not measured for these cylinders and we have assumed the same degree of damage for the cylinder specimens and 50 mm thick disks at equal number of freeze-thaw cycles. While this may not be a completely correct assumption, it provides a first order approximation. In **Figure 3-4**b the normalized surface resistivity decreases with increase of damage with a similar reduction as observed in bulk resistivity. While there is a slight difference between the bulk and surface measurements, the simplicity

of surface resistivity measurements potentially put forward the idea that this technique might be used to evaluate freeze-thaw damage on cement-based materials provided the boundary conditions and temperature effects are well controlled. More investigation, however, required to correlate surface resistivity to damage.

3.3.4 Sorptivity

Figure 3-5 illustrates the results of water absorption during the first 150 days. **Figure 3-5**a shows the amount of the absorbed water (normalized to the surface area of specimen) as a function of square root of time. **Figure 3-5**b shows the same results presented in **Figure 3-5**a in terms of degree of saturation. **Figure 3-5**a shows that the total water absorption increases with damage, indicating the physical change in pore structure (Ghasemzadeh and Pour-Ghaz 2014). Also, at early stages of water absorption, the rate of water absorption increases with damage. Furthermore, in **Figure 3-5**a, specimens with high level of damage reach the plateau earlier. This observation indicates that unsaturated cracks and capillary pores are first filled with water and then water is diffused to the larger air voids slowly. **Figure 3-5**b also shows specimens with high level of damage reach to higher degree of saturation at earlier time compare to specimens with a lower level of damage. **Figure 3-5**c shows that initial sorptivity increases almost linearly with an increase of damage while, the secondary soprtivity decrease with an increase of damage in low damage state and then remains constant at higher level of damage. It seems that the secondary sorptivity is independent of degree of damage. It is discussed in chapter 1 that cracks change water absorption mechanism in damaged specimens.

In the initial phase of water absorption, cracks act as capillary tubes that absorb water rapidly, provide access to capillary pores away from the exposed surface and provide access to large air-filled voids (Ghasemzadeh and Pour-Ghaz 2014). At later stage, air diffusion and dissolution mechanisms play a more significant role in water absorption (Ghasemzadeh and Pour-Ghaz (2014), Smyl et al. (2015)).

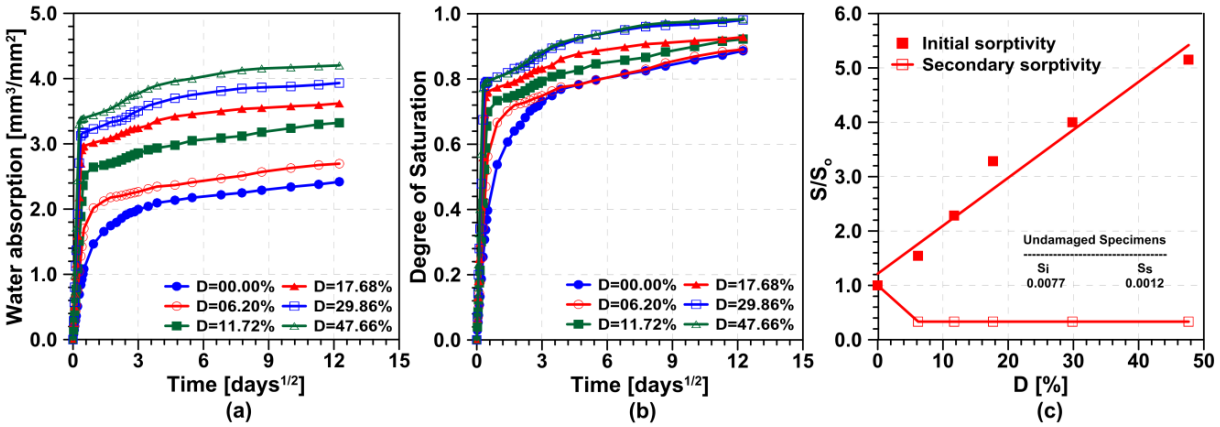

Figure 3-5: (a) Water sorption of mortar specimens with different degrees of damage during the first 150 days; (b) degree of saturation of mortar specimens with different degrees of damage; (c) normalized initial and secondary water sorptivity of mortar specimens as a function of damage.

3.3.5 Permeability

Figure 3-6a and **Figure 3-6**b illustrate the results of air permeability and water permeability measurements, respectively. In both experiments the values are normalized to the permeability of the undamaged mortar. Note that in **Figure 3-6**a, $K_{(air)}$ is air permeability index as opposed to actual permeability. The result in **Figure 3-6**a and **Figure 3-6**b show that air and water permeability exponentially increase with damage. The rapid increase of air and water

permeability with damage can be attributed to the high volume of crack density, increase in crack width, and crack percolation.

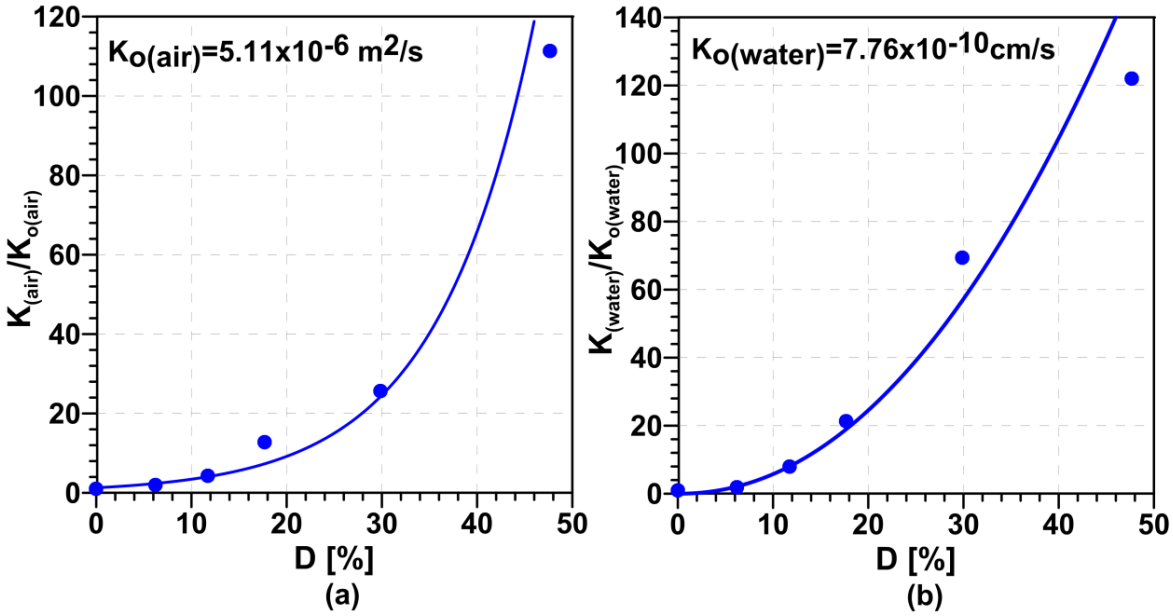

Figure 3-6: Normalized change of permeability with damage. (a) air permeability, (b) water permeability.

3.3.6 Drying

Figure 3-7 illustrates the results of drying test presented in terms of total remaining water in the specimens as a function of square root of time (to better illustrate the water loss at early ages). In **Figure 3-7**, it is observed that the rate of drying increases with damage since cracks provide paths for water to migrate to the surface. This mechanism is the so-called wicking which is created by drying of water from the capillary surfaces (Brosnan and Robinson 2003). Once water dries from the surface, cracks start to drain the interior water in cracks and capillary pores. From **Figure 3-7**, it seems that once all water in cracks is wicked to the surface, the

mechanism of drying changes to the diffusion of water vapour. However, there is certainly some overlap between these two mechanisms.

It is also important to note that in **Figure 3-7**, the total amount of water present in the samples increases continuously with damage. In **Table 3-3**, the saturation water content, the residual water content (the remaining water at the end of drying experiment after 60 days), and the amount of evaporated water (difference between initial and residual water) are provided for specimens with different degrees of damage. The saturation and residual water were determined by placing specimens in an oven at 50˚C for two days. As shown in **Table 3-3**, specimens retain significantly more water in the cracks as damage increases, resulting in supplying more water to the surface of specimen during drying test.

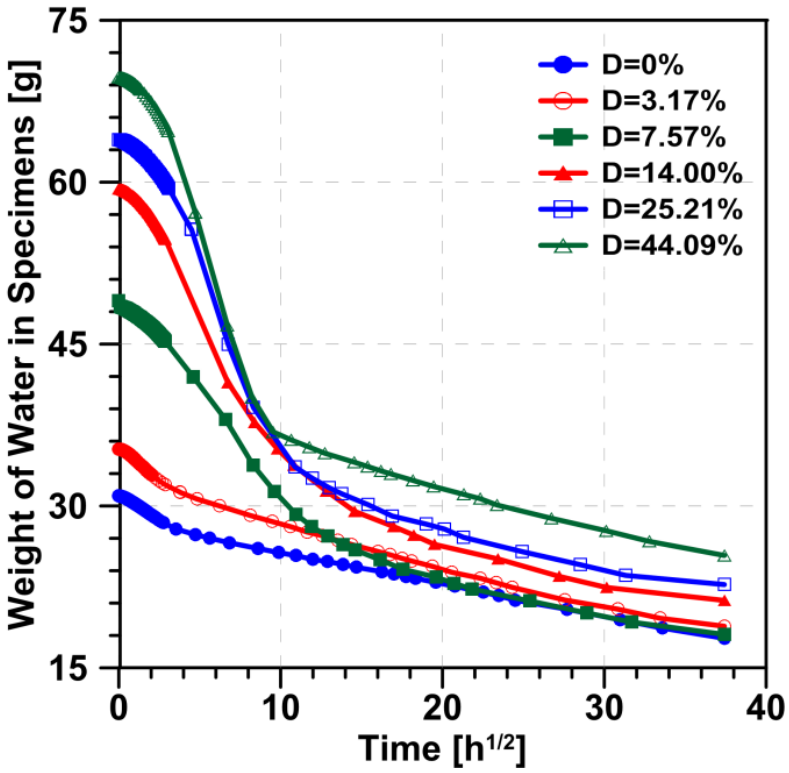

Figure 3-7: Change in water weight in mortar specimens with different degrees of damage during the first 60 days.

Table 3-3: Change in water content in specimens with different degrees of damage.

Damage	Amount of water in different conditions (g)		
	Saturation Water	Residual Water	Evaporated Water
0.00%	30.92	17.74	13.18
3.17%	35.26	18.86	16.4
7.57%	49.00	18.10	30.90
14.00%	59.37	21.25	38.12
25.21%	63.95	22.72	41.23
44.09%	69.72	25.42	44.30

3.3.7 Desorption isotherm

The desorption isotherm of specimens with different degrees of damage are shown in **Figure 3-8**. The water content gradually increases with damage at intermediate relative humidity values, followed by a rather large increase at high relative humidity values. The higher water content in mortar specimens with higher level of damage can be explained by the contribution of cracks acting as capillary porosity and retaining more water within the material (Ghasemzadeh and Pour-Ghaz 2014). The desorption isotherms can be used to provide a quantitative measure of size distribution of the cracks. Note however, the desorption isotherms are obtained up to 97.5% RH. Cracks within the samples however cover equivalent crack widths (Kelvin radius) much larger than that corresponding to relative humidity of 97.5%. Therefore, the entire information about the crack distribution is not necessarily included in the isotherms in **Figure 3-8**.

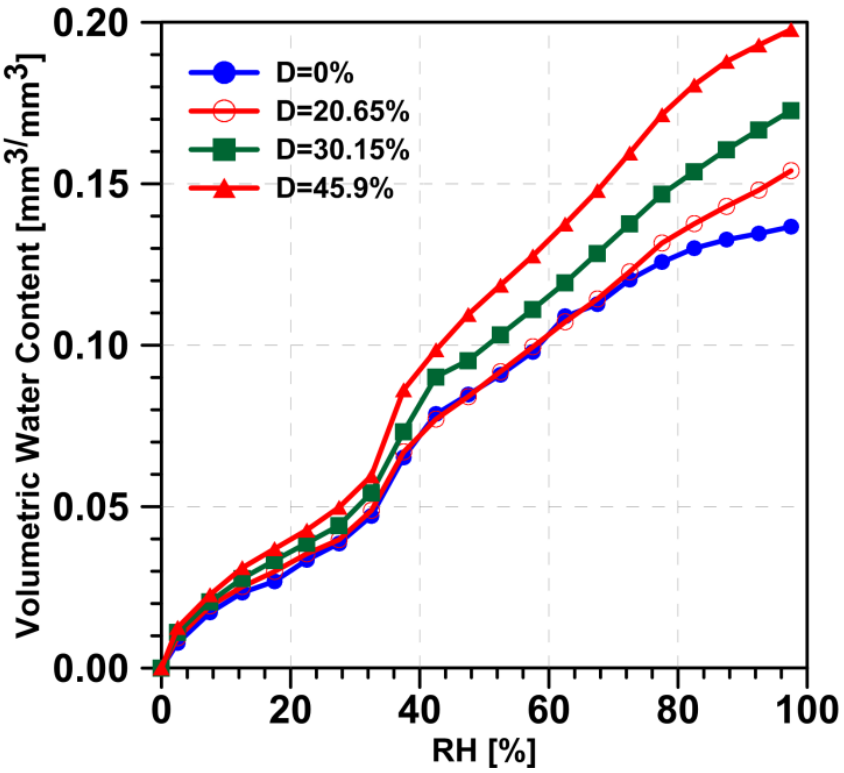

Figure 3-8: Desorption isotherm of mortar specimens with different degrees of damage.

3.4 Evaluating transport methods

Results of the laboratory tests on moisture transport in mortar specimens with different degrees of damage shows that transport measurement methods differently reflect the effect of damage. Table 3-4 summarizes how each measurement technique shows the effect of damage. Depending on the mechanism of mass transport, the effect of damage changes significantly. It can be seen that RCPT and electrical resistivity are not sensitive at high damage levels while they increase almost linearly at low damage levels. Initial sorptivity increases linearly with damage but secondary sorptivity initially decreases with damage and then remains

approximately constant. Finally, both air and water permeability increase exponentially with damage.

Table 3-4: Comparison of different transport measurement methods

Method	Effect of Damage	Mechanism of measurement
Rapid Chloride Penetration Test (RCPT)	Linearly increases at low damage levels of damage and then remains approximately constant	Electrophoresis
Electrical resistivity (EIS and surface resistivity)	Decreases at a high rate at low damage levels and with a low rate at high damage levels	Electrical conduction (AC current)
Sorptivity	Initial sorptivity increases linearly with damage and secondary sorptivity remain constant with damage increase	Capillary suction
Drying	The initial rate of drying increases with damage increase	Moisture diffusion
Air permeability	Air permeability exponentially increases with damage increase	Flow under pressure gradient
Water Permeability	Water permeability exponentially increases with damage increase	Flow under pressure gradient
Desorption isotherm	The water content gradually increases with damage at intermediate RH values, followed by a further increase at high RH values.	----

3.5 Chapter Conclusion

In this research, this question posed that how different measurement techniques show the effect of damage on mass transport, and which transport measurement method is more sensitive to the presence of damage? To this end, we experimentally measured the effect of damage, induced by freeze-thaw loading in mortar samples, using different mass transport measurement techniques. It was observed that mass transport increases with damage. However, different measurement methods differently reflect the effect of damage on mass transport depending on the mechanism of transport utilized in the measurement method.

Different methods also show different sensitivity to the presence of damage. Rapid chloride permeability test and electrical resistivity are only sensitive at low damage levels (below 20%). Initial sorptivity increases linearly with damage at all levels. Water and air permeability increase exponentially with damage and seem to be the most sensitive parameter to the presence of damage.

4. Numerical Simulation of Unsaturated Moisture Transport in Damaged Mortar and Concrete

4.1 Introduction

The rate of freeze-thaw deterioration, chemical attack, corrosion of reinforcement, and many other deleterious processes in concrete structures are strongly dependent on the rate of moisture ingress (Pour-Ghaz 2011). The rate of moisture ingress is influenced by the degree of saturation and the presence of damage (Sajedi et al. 2011). Concrete, during its service life, is rarely saturated and some degree of damage is often present (e.g., due to freeze-thaw). Distributed damage in concrete significantly increases the rate and the amount of moisture ingress (Yang et al. 2004, Hearn 1999, Aldia et al. 1999). While unsaturated moisture transport in concrete material has been studied (Hallaji et al. 2015, Lockington et al. 1999, Martys et al. 1997, Hall 1989), limited research exists on unsaturated moisture transport in damaged concrete. Specifically, modeling studies on unsaturated moisture transport in damaged concrete are scarce. In this research, it is investigated whether classical unsaturated moisture transport can be used to model moisture ingress in damaged mortar and concrete with a wide range of degree of damage.

The majority of the previous studies on transport in damaged concrete were experimental. These studies have shown that, for example, chloride migration increased 20% in concrete after subjecting concrete to high levels of compressive loading as tested by Rapid Chloride Permeability Testing (Samaha and Hover, 1992), the saturated water permeability of concrete

increases with damage (Wang et al. 1997), the rate and the total amount of moisture absorbed increases linearly with distributed damage (Yang et al. 2006), and the effect of distributed damage is dependent on the mechanism of transport (Ghasemzadeh and Pour-Ghaz 2014).

The classical model describing unsaturated mass transport in porous media is Richards' equation (Richards, 1931), modeling capillary suction. Richards' equation has been identified as a valid model for mass transport in building materials (Wilson et al. 1999). Analytical solutions to Richards' equation have been developed for simple geometries (Cao et al. 2014, Parlange et al. 1999, Parlange et al. 1997, Warrick et al. 1991). Analytical solutions are generally feasible in simple geometries subjected to simple boundary conditions. Practical application of Richards' equation requires numerical methods, such as the Finite Element Method. The Finite Element Method has been used previously to analyze unsaturated mass transport in concrete (Pour-Ghaz et al. 2009a, Pour-Ghaz et al. 2009b). However, none of these studies investigated cementitious material with distributed damage. There is a need, therefore, to identify modeling methods that can accurately model unsaturated moisture transport in damaged mortar and concrete. The research question of the current chapter is: Can classical isothermal unsaturated moisture transport be used to model moisture ingress in damaged mortar and concrete?

4.2 Numerical Methods

4.2.1 2.1 General

In this research, moisture transport is modeled using the so-called Richards' Equation (Eq. 4-1) (Richards, 1931) for unsaturated moisture flow. Equation 4-1 is the classical governing differential equation for isothermal unsaturated flow where air diffusion and dissolution do not play a significant role.

$$\frac{\partial \theta}{\partial t} = \frac{\partial}{\partial x_i}\left[K(h)\left(\frac{\partial h}{\partial x_j} + \delta_{ij}\right)\right] \qquad \text{Eq.4-1}$$

where $K = K(h)$ (mm/hour) is the unsaturated hydraulic conductivity, θ is the volumetric moisture content, h is the pressure head, x_i is the spatial coordinate (i,j = 1, 2, 3 for three dimensional space) and δ_{ij} is the Kronecker Delta function which accounts for the gravitational effect.

4.2.2 Van Genuchten – Maulem Model

The unsaturated hydraulic conductivity (K) in Eq. 4-1 is a function of pressure head (i.e., $K = K(h)$). Experimental measurements of unsaturated hydraulic conductivity are generally difficult and time consuming. These measurements are especially challenging for cement-based materials due to the fine pore size distribution resulting in a high pressure head requirements at low water contents (Pour-Ghaz et al. 2009a, Pour-Ghaz et al. 2009b).

Alternatively, the unsaturated hydraulic conductivity can be expressed as a product of the saturated hydraulic conductivity, K_s, and the relative hydraulic conductivity, K_r (i.e., $K = K_s K_r$). The value of K_s can be experimentally measured using Darcy's law. The relative hydraulic conductivity is related to water content and pressure head by Maulem's model (Maulem 1976) given by Eq. 4-2

$$K_r = \Theta^I \left[\frac{\int_0^{\Theta} \frac{1}{h(x)} dx}{\int_0^1 \frac{1}{h(x)} dx} \right]^2 \qquad \text{Eq.4-2}$$

$$\Theta = \frac{\theta - \theta_r}{\theta_s - \theta_r} \qquad \text{Eq.4-3}$$

Where $0 \leq \Theta \leq 1.0$ is the effective material saturation, and θ_s and θ_r are saturated moisture content and residual moisture content respectively. In this work, θ_s is experimentally obtained for each degree of damage and $\theta_r = 0$ (Pour-Ghaz et al. 2009a, Pour-Ghaz et al. 2009b). I is an empirical parameter which has been described as accounting for tortuosity and connectivity of pores (Maulem, 1976). Maulem proposed $I = \frac{1}{2}$ as an optimal value for 45 undisturbed soils; however, he noted that values for I can take positive or negative values. Values for soil have been shown to range from –8.83 to 100 (Schaap and Leij 2000, Yates 1992, Schuh and Cline 1990). Kosugi argued that I has no physical significance and should be interpreted as a fitting parameter (Kosugi 1999). Values of I in concrete are not readily available. Schneider et al. (2012) reported values of -3.0 and 35.2 for mortar and concrete, respectively. Poyet et al. (2011) concluded that the values of I are negative for concrete.

In this study, values of I are estimated by training the model: The experimental data for sorption were split into two sets: training and test set. The training set was used to estimate the value of I for each degree of damage by fitting the simulations to the experimental data (computed to the nearest integer).

To integrate Eq. 4-2, the effective saturation should be expressed as a function of pressure head (i.e., $\Theta = \Theta(h)$). Different models for $\Theta = \Theta(h)$ have been developed (Kosugi 1996, Brooks and Corey 1964). The model proposed by van Genuchten is used in this study (van Genuchten 1980, van Genuchten 1985) and is shown in Eq. 4-4

$$\Theta = \frac{1}{[1+(\alpha h)^n]^m}, m = 1 - \frac{1}{n} \quad \text{Eq.4-4}$$

Where α and n are fitting parameters (α, inversely proportional to the mean pore diameter (mm^{-1}) and n (non-dimensional) is the curve shape parameter). These fitting parameters are obtained by fitting Eq. 4-4 to experimentally obtained water retention curves. In the case of cement-based materials, instead of water retention, $\Theta = \Theta(h)$, it is more common to measure the sorption isotherm of material (i.e., $\Theta = \Theta(RH)$, RH = relative humidity). The sorption isotherm can then be converted to retention curve using Kelvin-Laplace Equation (Eq. 4-5) (Pour-Ghaz et al. 2009a, Leech et al. 2006):

$$h = \frac{\rho_w RT}{m_w} \ln(RH) \quad \text{Eq.4-5}$$

where ρ_w (g/mm^3) is the density of water, R (J.K^{-1}mol^{-1}) is universal gas constant, T (K) is the temperature, and m_w (g/mole) is the molecular weight of water.

4.2.3 Numerical Simulation and Experimental Corroboration

In this work, a commercially available Finite Element Software, HYDRUS 3D, was used (Sejna et al., 2014). The sorption test was simulated by modeling water sorption in a 100 mm x 25 mm cylinder. Zero-flux boundary conditions were applied to all surfaces except the bottom surface where the sample was in contact with water. The boundary condition at the bottom surface was saturated boundary condition. Uniform initial moisture content, θ_i, were considered in this study, values for θ_i are tabulated in the section 4-4. This initial uniform moisture content is essentially different from experimental specimens since these specimens were conditioned according to ASTM C1585-13. Such a conditioning does not necessarily grant uniform moisture distribution. However, this assumption is necessary for modeling as the actual moisture distribution within the sample is complex and unknown. Finite element modeling consisted of tetrahedron elements with a maximum dimension of 1.0 mm. The finite element model was solved in terms of moisture content.

Figure 4-1 graphically depicts the procedure used in this research to obtain the material parameters for simulations. The experimental measurements included desorption isotherm for mortar and concrete at different degree of damage, measurement of saturated hydraulic

conductivity at each degree of damage, saturation water content, and water sorption experiments.

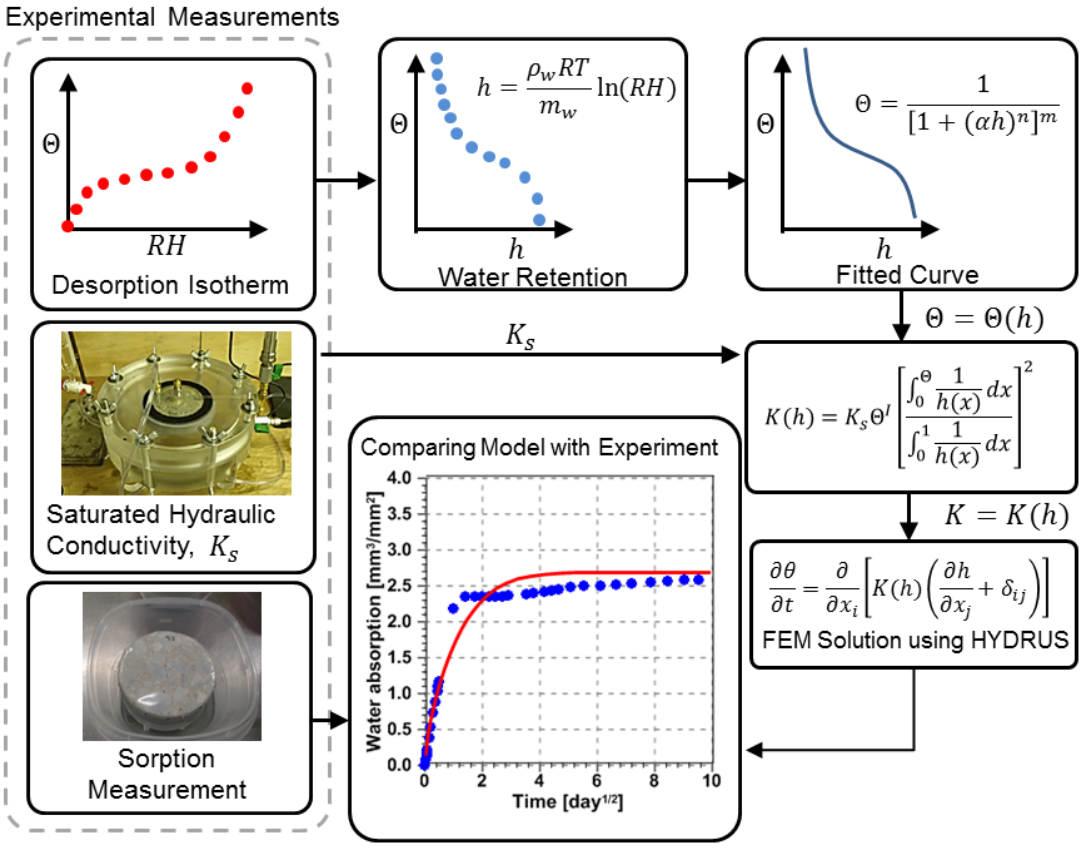

Figure 4-1: Schematic of numerical procedure and experimental corroboration of unsaturated moisture transport modeling.

4.3 Materials and Methods

4.3.1 Materials

Both mortar and concrete were used. **Table 4-1** reports the mixture proportions for concrete and mortar. For both materials, cylindrical samples with dimensions 200 mm x 100 mm were cast. All specimens were cut into disks (25 mm x 100 mm) after 24 hours of sealed curing and then were stored for 18 months in lime saturated water. Specimens were then subjected to freeze-thaw loading to induce different degrees of damage. The degree of damage after each freeze thaw cycle was quantified using the change in dynamic elastic modulus (Ghasemzadeh and Pour-Ghaz 2014). Concrete specimens with five different degrees of damage (10, 21, 29, 36, and 47%) and mortar specimens with three different degrees of damage (18, 30, and 48%) were prepared.

Table 4-1: Mix proportions of concrete and mortar

Proportions	Concrete	Mortar
Cement* (kg/m^3)	261	609
Fly Ash, Type F (kg/m^3)	83**	---
Water (kg/m^3)	132.5	256
Coarse Aggregate (kg/m^3)	1073	0
Fine Aggregate (kg/m^3)	747	1466
Water Reducer (kg/m^3)	0.50	0.50
w/cm	0.50	0.42

*Ordinary Type I portland cement

**24% replacement by mass of cement

4.3.2 Desorption Isotherm

4.3.2.1 Concrete

Specimens, with different degrees of damage, were conditioned at six relative humidity (32.8%, 50%, 65%, 75.3%, 85.1%, and 93.6%). The concrete specimens had an average mass of 52.5 g and an average thickness of 5.64 mm. Specimens were conditioned using saturated salt solutions, except for the 50% and 65% RH where environmental chambers were used. A total of three replicate specimens were used for each degree of damage.

4.3.2.2 Mortar

To measure desorption isotherm of mortar specimens with different degrees of damage, an automated sorption analyzer was utilized. Small samples (0.5-1.5 mm thick and 50-100 mg weight) were used. The mass of the specimens were monitored while the relative humidity was sequentially dropped from 97.5% to 0% RH, with a 5% RH decrease between each successive step after reaching equilibrium. Equilibrium was defined as a mass change less than 0.001 mg within 15 minutes. A comprehensive description of isotherm measurements using automated sorption analyzer can be found (Villani et al. 2014, Pour-Ghaz et al. 2010).

4.3.3 Saturated Hydraulic Conductivity

The saturated hydraulic conductivity (K_s) measurements were performed using an in-house developed equipment. Measurements were performed on 25 mm thick disks. A total of three replicates were used for concrete and a total of four replicates were used for mortar at each degree of damage. The details of water permeability can be found in (Ghasemzadeh and Pour-Ghaz 2014).

4.4 Results and Discussion

4.4.1 Material Parameters

Figure 4-2a and **Figure 4-2**b show the measured desorption isotherms for mortar and concrete specimens respectively. The desorption isotherms of mortars have a higher number of data

points and a wider range of RH values, as compared to that of concrete, since they were measured using an automated sorption analyzer. For both materials the isotherms shift upward with increased damage, indicating damage increases porosity over a wide range (Ghasemzadeh and Pour-Ghaz 2014). The van Genuchten model (Eq. 4-4) was fit to these isotherms, after converting them to water retention curves using Eq. 4-5. The van Genuchten model parameters for mortar and concrete are reported in **Table 4-2** and **Table 4-3** respectively. The values for saturated hydraulic conductivity (K_s), and saturated moisture content (θ_s), empirical parameter *I* are also reported in **Table 4-2** and **Table 4-3**. In **Table 4-2** and **Table 4-3** "C" and "M" stand for concrete and mortar respectively, and the number following these letters indicates the degree of damage.

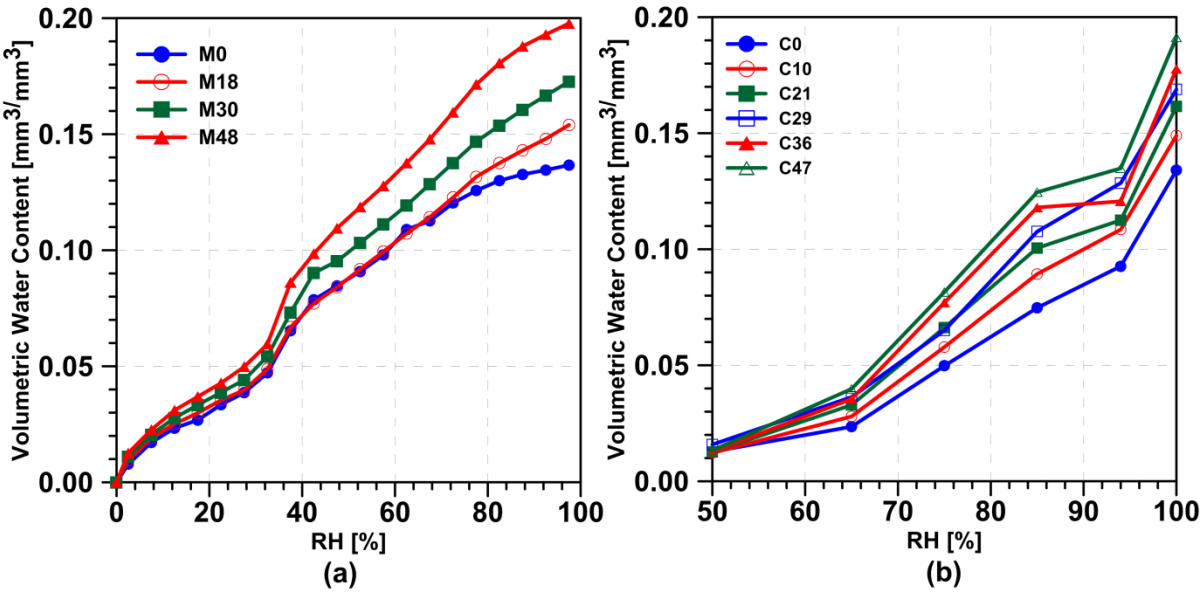

Figure 4-2: Desorption isotherm of specimens with different degrees of damage; (a) mortar, (b) concrete

Table 4-2: Saturated hydraulic conductivity, saturation water content, and van Genuchten model parameters for mortar specimens

Identifier	**Damage**	**Ks**	**α**	**n**	***l***	**θ_i**	**θ_s**
-	%	mm/hr	1/mm	-	-	-	-
M0	0	$3.0x10^{-5}$	$1.2x10^{-2}$	2.06	-9.0	0.03	0.14
M18	18	$59.0x10^{-5}$	$1.8x10^{-2}$	1.75	-8.0	0.01	0.15
M30	30	$194.0x10^{-5}$	$3.3x10^{-2}$	1.52	-8.0	0.02	0.17
M48	48	$341.0x10^{-5}$	$1.7x10^{-2}$	1.81	-8.0	0.01	0.20

Table 4-3: Saturated hydraulic conductivity, saturation water content, and van Genuchten model parameters for concrete specimens

Identifier	**Damage**	**Ks**	**α**	**n**	***l***	**θ_i**	**θ_s**
-	%	mm/hr	1/mm	-	-		-
C0	0	$1.4x10^{-4}$	$6.4x10^{-2}$	2.26	-7.0	0.03	0.15
C10	10	$7.0x10^{-4}$	$4.9x10^{-2}$	2.45	-7.0	0.03	0.15
C21	21	$14.0x10^{-4}$	$4.6x10^{-2}$	2.47	-7.0	0.04	0.16
C29	29	$26.0x10^{-4}$	$4.6x10^{-2}$	2.48	-6.0	0.03	0.17
C36	36	$56.0x10^{-4}$	$4.1x10^{-2}$	2.64	-5.0	0.03	0.18
C47	47	$131.0x10^{-4}$	$4.3x10^{-2}$	2.58	-5.0	0.03	0.19

It is pointed out here that while Maulem (Maulem, 1976) proposed parameter I as to account for tortuosity and pore connectivity, such a physical interpretation is only meaningful if $I \geq 0$. In this study, using training set, satisfactory results were found for negative values similar to the works in (Poyet et al. 2011, Schneider et al. 2011, Schaap and Leij 2000, Yates 1992, and Schuh and Cline 1990). Negative values of I result in unrealistic relative hydraulic conductivity at intermediate levels of saturation and therefore should only be considered as a modeling parameter.

Saturated hydraulic conductivity (K_s), was measured experimentally in this work and has a significant effect on initial sorption. The analytical study in (Ghasemzadeh and Pour-Ghaz 2014) has shown that initial sorption increases linearly with square root of K_s.

4.4.2 Simulation of Unsaturated Mass Transport in Mortar

Results of the experimental measurements and numerical simulations of water absorption of mortar with different degrees of damage are compared in **Figure 4-3**. The results are presented as volume of water (mm^3) absorbed per water absorbing surface area (mm^2) of the sample versus square root of time ($day^{1/2}$). The results were compared for the first 90 days. Note that for each degree of damage, simulation results are compared with experimental results from two samples from the test set.

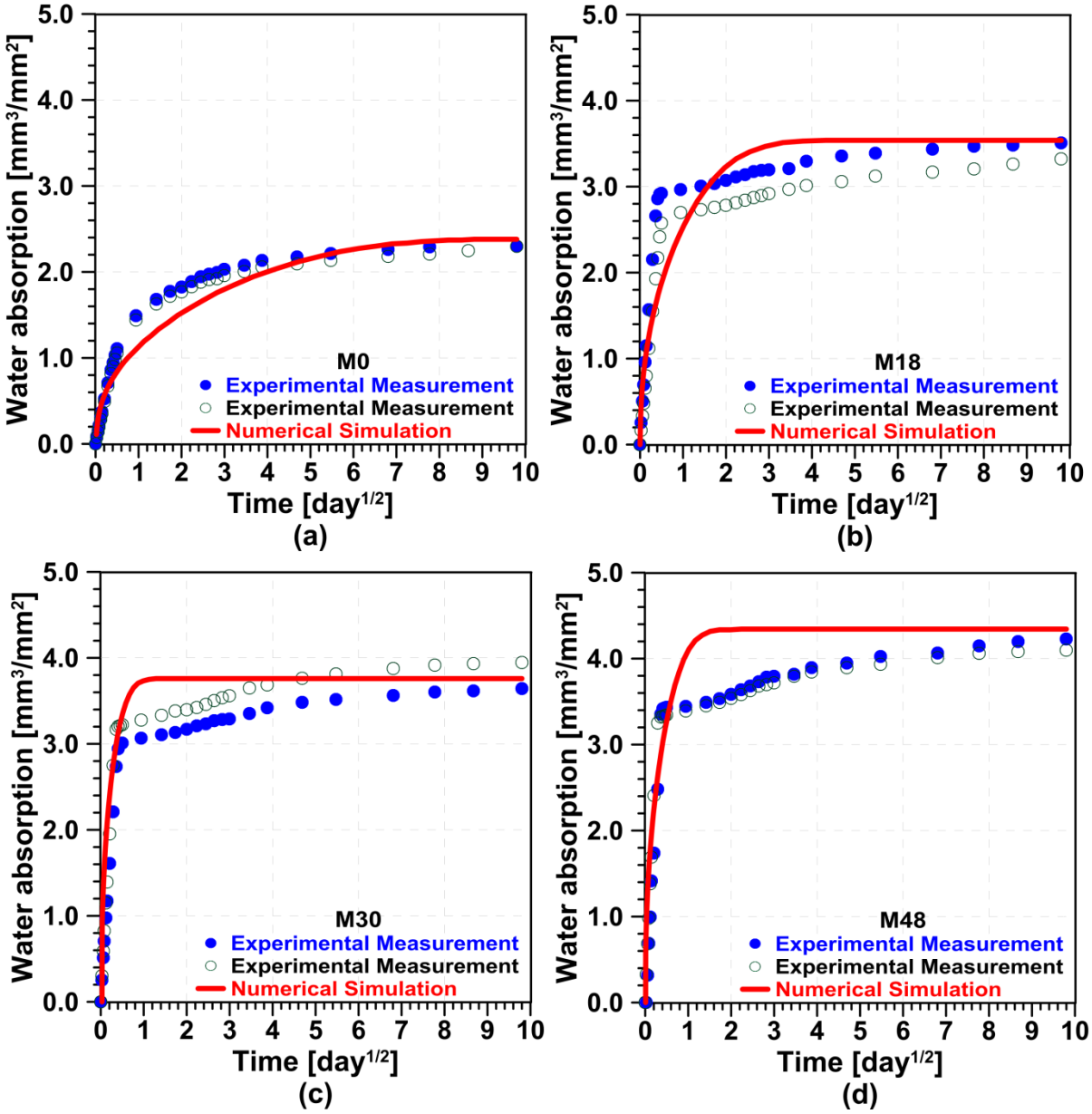

Figure 4-3: Experimental and numerical sorption results for mortar specimens with different degrees of damage; a) D=0%, b) D=18%, c) D=30%, d) D=48%

In **Figure 4-3**, for all degrees of damage, the results of simulations of water absorption in mortar compare well with experimental results at early stages of water absorption. The slope of the first linear portion of the experimental and numerical results, initial sorptivity, is

calculated and plotted as a function of degree of damage in **Figure 4-4**. **Figure 4-4** confirms that the results of simulation for the initial stages of water absorption agree well with experimental results.

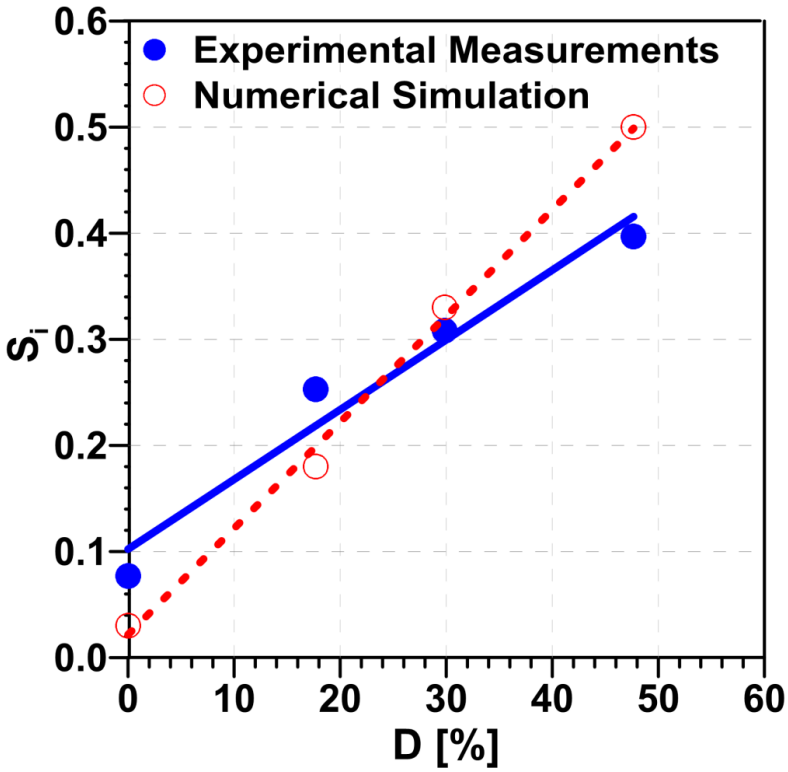

Figure 4-4: Initial sorptivity of mortar as a function of damage

In **Figure 4-3**, at later stages of water absorption, simulation results deviate from the experimental results. The deviation increases with damage level. As the damage increases, a sharp "knee point" appears in both experimental and numerical results. There is however, a distinct difference between the numerical and experimental results after the knee point. In

simulated results the sharp transition marks the transition from unsaturated to saturated state of the sample while in experimental results the specimen continues to absorb water after the knee point.

The knee point marks transition from capillary suction to air diffusion and dissolution mechanism of water absorption (Ghasemzadeh and Pour-Ghaz 2014). Since Richards' equation does not account for air diffusion and dissolution mechanisms, in simulation results (**Figure 4-3**), the specimen continues to absorb water until saturation with capillary suction. However, in experimental results, the specimen continues to absorb water after the knee point with air diffusion and dissolution mechanisms.

4.4.3 Simulation of Unsaturated Mass Transport in Concrete

Results of the experimental measurements and numerical simulation of water absorption in concrete with different degrees of damage are compared in **Figure 4-5**. Similar to the results for mortar specimens, the results are compared for the first 90 days. **Figure 4-6**, similar to **Figure 4-4**, compare the initial sorptivity calculated from experimental and numerical results. Note that for each degree of damage, simulation results are compared with experimental results from two samples from the test set. The results in **Figure 4-5** are generally similar to the results presented in **Figure 4-3**. At early stages of water absorption, the simulation and experimental results agree well while they diverge at later stages of water absorption.

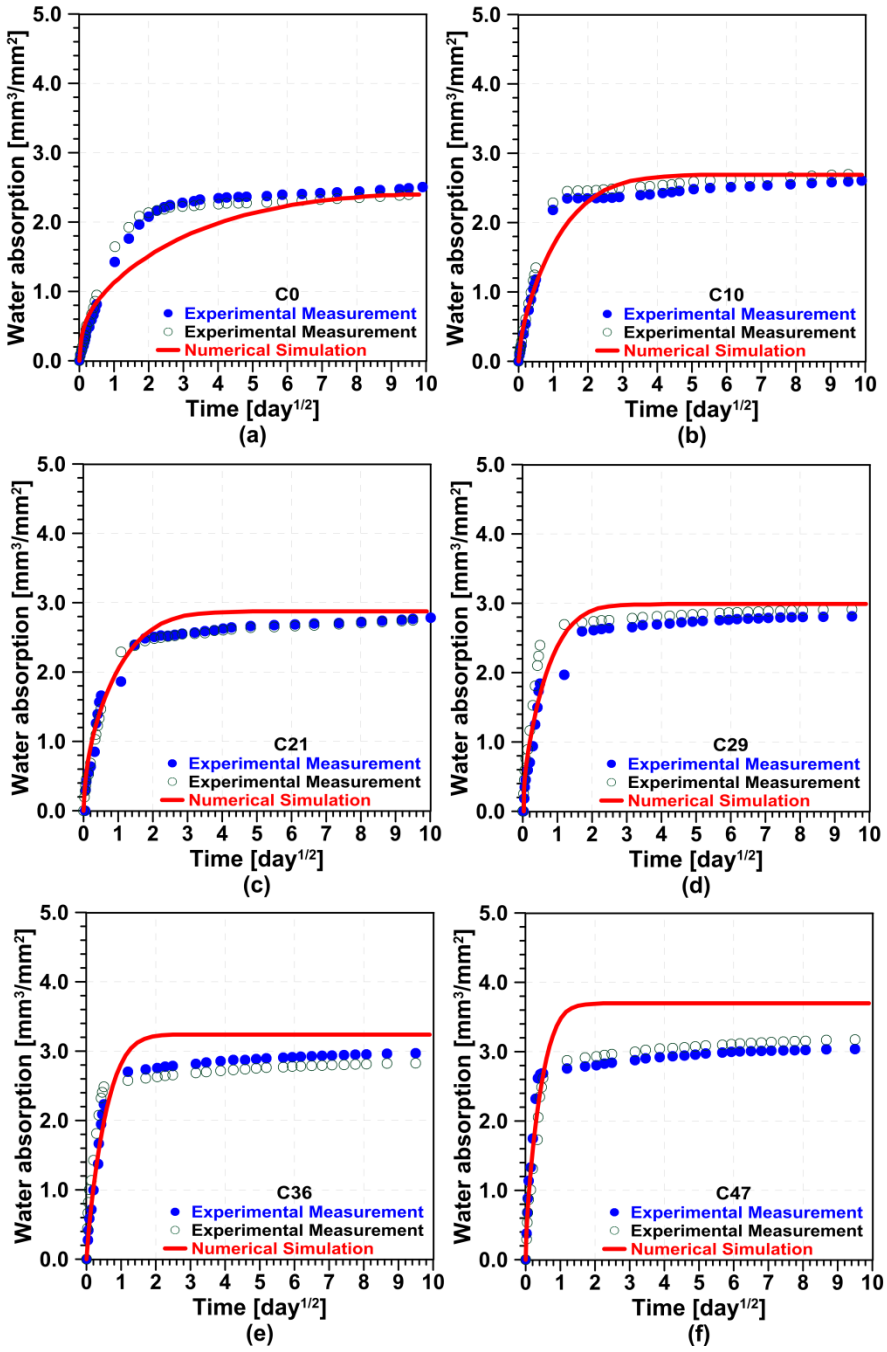

Figure 4-5: Experimental and numerical sorption results for concrete specimens with different degrees of damage; a) D=0%, b) D=10%, c) D=21%, d) D=29%, e) D=36 %, f) D=47%

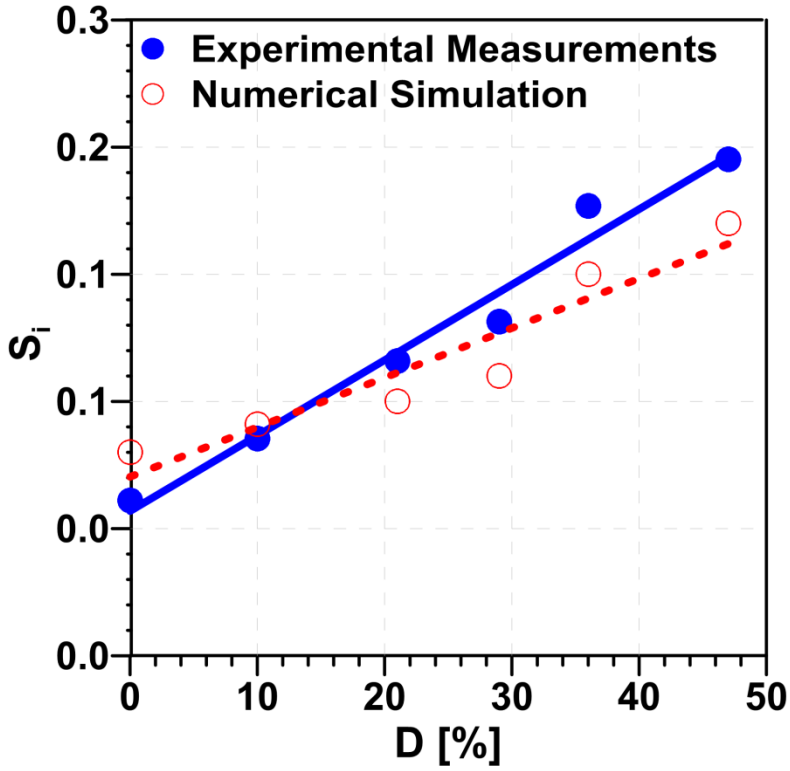

Figure 4-6: Initial sorptivity of concrete as a function of damage

4.5 Chapter Conclusion

In this work, classical isothermal unsaturated moisture transport model was used to simulate moisture ingress in mortar and concrete with a wide range of damage. The required material parameters for the simulations were experimentally obtained. The results indicate that, for all levels of damage, the classical isothermal unsaturated moisture transport model well simulates the early stages of moisture ingress in mortar and concrete where capillary suction is the underlying mechanism. At later stages where air diffusion and dissolution mechanisms play a more significant role, the results of simulation deviate from experimental measurements. The use of more advanced material models might be necessary to obtain more accurate results.

5. Estimating Freeze-Thaw Damage in Concrete Using Nonlinear Acoustic Spectroscopy

5.1 Introduction

Damage caused by freeze-thaw is a major concern in concrete structures since it adversely affects the mechanical properties of concrete and accelerates the rate of mass transport, reducing the service life of the structures. The remaining service life of concrete structures can be more accurately predicted if damage is properly quantified (Ghasemzadeh et al. 2015). To quantify damage, linear methods based on the change in resonance frequency (Ghasemzadeh et al. 2105, Ghasemzadeh and Pour-Ghaz 2014, Kim and Weiss 2003, Farnam et al. 2014) or change of quality factor (Q-factor) (Eiras et al. 2014, Eiras et al. 2013) have been developed. These methods require a prior knowledge of the undamaged properties (e.g., resonance frequency, Q-factor, or elastic modulus). Very often, however, there exists no reliable information about the undamaged properties. There is a need therefore, for new methods to estimate damage in the absence of a prior knowledge of the undamaged properties. Methods that are based on the nonlinear response of materials to excitations may be used for this purpose.

The nonlinear response of concrete to acoustic and ultrasonic excitations is mainly dominated by the classical anharmonicity (Kim et al. 2006a, Kim et al. 2006b) and dynamic hysteresis (Johnson et al. 1996). Nonlinear elasticity parameters are sensitive to the microstructural

changes and the formation of microcracks. The sensitivity of nonlinear parameters to the mechanical damage (Antonachi et al. 2010, Eiras et al. 2012), alkali-silica reaction damage (Chen et al. 2010, Lesnicki et al. 20111, Chen et al. 2011, Lesnicki et al. 2013, Eiras et al. 2013b), and freeze-thaw damage (Eiras et al. 2013) has been previously shown.

Several elegant nondestructive test methods have been developed that are based on nonlinear elasticity. (Kim et al. 2006b) evaluated fatigue damage in alloys using the amplitude of a second harmonic signal by generating higher order harmonics and subharmonics. In Van Den Abeeele and Johnson (2000), Chen et al. (2008) and Kober and Prevorovsky (2012) damage in metals and cement-based materials were estimated by nonlinear modulation of waves with different frequencies. In Chen et al. (2010), Lesnicki et al. (2011), Chen et al. (2011), Lesnicki et al. (2013), Eiras et al. (2013a), Eiras et al. (2013b), Chen et al. (2015), Kodjo et al. (2009) the shift of resonance frequencies with increase of excitation amplitude and time shift (Moradi-Marani et al. 2014) were used to evaluate damage in concrete.

In addition to the frequency change, linear change in the magnitude of Q-factor has been used as a measure of damage (Eiras et al. 2013a and Eiras et al. 2013b). The nonlinear change of normalized Q-factor with excitation amplitude in cementitious materials has been discussed in literature (Chen et al. 2011, Johnson and Sutin 2005) but has not been used to measure damage, to the best of knowledge.

In this research, it is investigated whether nonlinear elasticity parameters and the nonlinear change of Q-factor can be used to estimate damage in concrete without a prior knowledge of

the undamaged material properties. To this end it is studied how these parameters change with freeze-thaw damage in concrete. Specifically, it is used the so-called Nonlinear Impact Resonance Acoustic Spectroscopy (NIRAS) technique developed and used in (Chen et al. 2010, Lesnicki et al. 20111, Chen et al. 2011, Lesnicki et al. 2013, Chen et al. 2015, Kodjo et al. 2009). However, in this work, circular disk geometry is used which enables estimation of dynamic elastic modulus based on axisymmetric flexural vibration solution of the free circular plate (Hutchinson 1979). Disk geometry is also attractive since it can be produced from field extracted samples. It also is used active and passive acoustic emission to quantify and monitor damage during freeze-thaw loading.

In the following, a brief theoretical background on the nonlinear vibration and axisymmetric flexural vibration solution are presented. Then, materials, sample preparation, and test methods are discussed. This is followed by results and discussions. Finally the summary of the findings are presented.

5.2 Background

5.2.1 Nonlinear Resonance Vibration

The reduction of resonance frequency with the formation of defects and microcracks is well known. This effect, which is referred to as linear frequency reduction, is shown schematically in **Figure 5-1**a with ΔF. In addition to this linear effect, the presence of defects can produce highly nonlinear effects such as nonlinear resonance frequency shift with increased amplitude

of excitation. This nonlinear effect is shown schematically in **Figure 5-1**b with β. The NIRAS technique is based on monitoring this shift in frequency.

The nonlinear resonance frequency shift in concrete, is mainly attributed to the effect of microcracks such as the clapping motion of the cracks and the Hertzian contact of the discontinuity faces, resulting in the distortion of elastic waves (Lesnicki et al. 2011). The elastic wave distortion phenomena can be modeled with hysteresis and classical nonlinear constitutive law for elastic modulus per Equation 5-1:

$$E = E_0(1+\gamma\varepsilon+\delta\varepsilon^2+\alpha(\Delta\varepsilon+\varepsilon\ sgn(\dot{\varepsilon}))) \qquad \text{Eq. } 5-1$$

where E_0 is the linear elastic modulus, γ is the quadratic anharmonicity parameter, δ is the cubic anharmonicity parameter, ε is strain, $\Delta\varepsilon$ and $\dot{\varepsilon}$ are the strain amplitude and the strain rate respectively, α is the hysteresis nonlinear parameter, and sgn is the sign function.

The relation between normalized resonance frequency shift and strain amplitude is shown in Equation 5-2 (Van Den Abeele et al. 2000):

$$\frac{f_0-f}{f_0} \approx \beta\Delta\varepsilon \qquad \text{Eq. } 5-2$$

where f_0 and f are the resonance frequencies at the lowest and a higher excitation amplitudes respectively, and β is the nonlinear parameters (Chen et al. 2011). β is proportional to the parameters describing nonlinearity in Equation 5-1 (i.e., γ, δ, and α).

Quality factor, Q, is another parameter that is used to quantify damage. Q is a measure of the ratio of the stored to dissipated energy and is defined as the ratio of the resonance frequency to its half-power bandwidth as schematically shown in **Figure 5-1**b and presented by Equation 5-3.

$$Q = \frac{f_0}{f_2 - f_1} \qquad \text{Eq. } 5-3$$

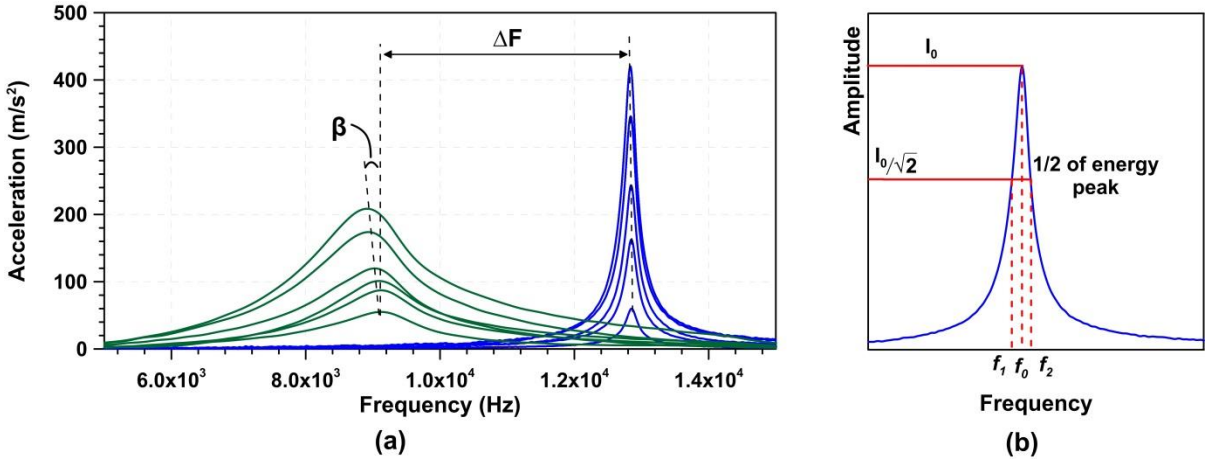

Figure 5-1: (a) Schematic illustration of linear frequency shift, ΔF, and nonlinear frequency shift, (b) Schematic illustration of quality factor, Q, calculation.

5.2.2 Axisymmetric Flexural Vibration of a Thick Circular Plate

The circular disk geometry used in this work, enables calculation of dynamic elastic modulus from resonance frequency using the solution for the axisymmetric flexural vibration of a thick free circular plate (Hutchinson 1979). The dynamic elastic modulus, E_d, can be calculated using Equation 5-4.

$$E_d = 2(1+\nu)\rho[\frac{\pi fd}{\Omega_0}]^2 \qquad \text{Eq. } 5-4$$

where ν is the Poisson's ratio, ρ is the mass density of the disk, f is the resonance frequency, d is the diameter of the disk, and Ω_0 is the dimensionless resonance frequency parameter. The dimensionless resonance frequency parameter is estimated for a given geometry using the axisymmetric flexural vibration of a thick circular plate provided in Hutchinson (1979).

The equations describing axisymmetric flexural vibration of the circular disk are shown by Equations 5-5 and 5-6.

$$K[\psi' + \frac{\psi}{r} + \omega'' + \frac{\omega'}{r}] + \Omega^2\omega = 0 \qquad \text{Eq. } 5-5$$

$$\frac{2}{1-\nu}[\psi'' + \frac{\psi'}{r} - \frac{\psi}{r^2}] - \frac{3K(\psi + \omega')}{h^2} + \Omega^2\psi = 0 \qquad \text{Eq. } 5-6$$

where r, ω and ψ are, respectively, dimensionless radial coordinate, dimensionless axial displacement and dimensionless radial displacement of the disk, h is the thickness to diameter ratio of the disk, K is the shear coefficient of the disk, and is the dimensionless frequency parameter. Primes in Equations 5-5 and 5-6 denote differentiation with respect to r. Equations 5-5 and 5-6 can be solved by letting:

$$\psi = J_1(\delta r) \qquad \text{Eq. } 5-7$$

$$\omega = AJ_0(\delta r) \qquad \text{Eq. } 5-8$$

where A is an arbitrary constant, and $J_1$and J_0 are the Bessel functions of the first kind. By substitution of Equations 5-7 and 5-8 into Equations 5-5 and 5-6, Equation 5-9 is obtained. Since, A is an arbitrary constant, Equation 5-9 is solved by setting the determinant of the coefficients matrix equal to zero resulting in Equation 5-10.

$$\begin{bmatrix} K\delta & \Omega^2 - K\delta^2 \\ \delta^2 - \dfrac{2\delta^2}{(1-\nu)} - \dfrac{3K}{h^2} & \dfrac{3K\delta}{h^2} \end{bmatrix} \begin{bmatrix} 1 \\ A \end{bmatrix} = \begin{bmatrix} 0 \\ 0 \end{bmatrix} \qquad \text{Eq. } 5-9$$

$$\delta^4 + a_1\delta^2 + a_2 = 0 \qquad \text{Eq. } 5-10$$

where

$$a_1 = -\Omega^2[\frac{1}{K} + \frac{(1-\nu)}{2}] \qquad \text{Eq. } 5-11$$

$$a_2 = \Omega^2[\frac{\Omega^2}{K} - \frac{3}{h^2}]\frac{1-\nu}{2} \qquad \text{Eq. } 5-12$$

Only two out of the four roots of δ in Equation 5-10 are real. The real roots are used with Bessel function and in the case of the imaginary roots, the Bessel function is replaced by the modified Bessel function and the imaginary root is considered real. By using two roots of δ^2 in Equation 5-9, Equations 5-7 and 5-8 can be expressed by Equations 5-13 and 5-14.

$$\psi = B_1 J_1(\delta_1 r) + B_2 J_1(\delta_2 r) \qquad \text{Eq. } 5-13$$

$$\omega = B_1 A_1 J_0(\delta_1 r) + B_2 A_2 J_0(\delta_2 r) \qquad \text{Eq. } 5-14$$

where B_1 and B_2 are arbitrary constants. The boundary condition of the disk is satisfied by Equation 5-15.

$$\begin{bmatrix} [1-sgn(\delta_1)A_1]J_1(\delta_1) & [1-sgn(\delta_2)A_2]J_1(\delta_2) \\ \delta_1 J_1'(\delta_1)+\nu J_1(\delta_1) & \delta_2 J_1'(\delta_2)+\nu J_1(\delta_2) \end{bmatrix} \begin{bmatrix} B_1 \\ B_2 \end{bmatrix} = \begin{bmatrix} 0 \\ 0 \end{bmatrix} \qquad \text{Eq. } 5-15$$

Ω_0 is the solution of Equations 5-5 and 5-6 satisfying the boundary condition in Equation 5-15 and is found iteratively. An iterative procedure, shown in **Figure 5-2** is programmed which is described as follows. First an initial value is assumed for Ω. Then, this Ω is used in Equations 5-11 and 5-12, to calculate a_1 and a_2, and consequently in Equation 5-10 to calculate δ_1 and δ_2. Then A_1 and A_2, roots of Equation 5-9, are calculated. Finally, the determinant of coefficient matrix in Equation 5-15 is found to satisfy the boundary conditions. The incremental assumption for Ω continues until this determinant becomes zero with an acceptable tolerance. The computed frequency parameter represents dimensionless resonance frequency, Ω_0 (Leming et al. 1998, Recalde and Leming 2009).

Finally, Ω_0, f, d, ρ and υ are used in Equation 5-4 to calculate the dynamic elastic modulus. It is performed a large set of computations to calculate Ω_0 for a wide range of circular disk geometries. Figure 5-3 shows Ω_0 for a wide range of disk sizes with different thicknesses for two Poisson's ratios (0.2 and 0.25).

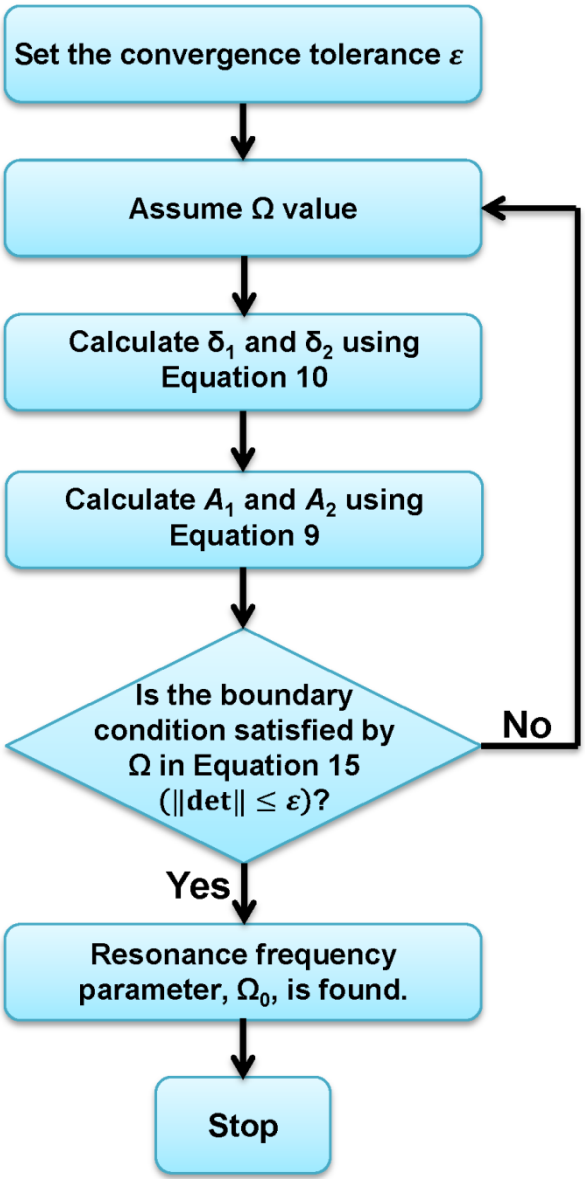

Figure 5-2: Flowchart of the semi-analytical approach for computing dimensionless resonance frequency parameter, Ω_0.

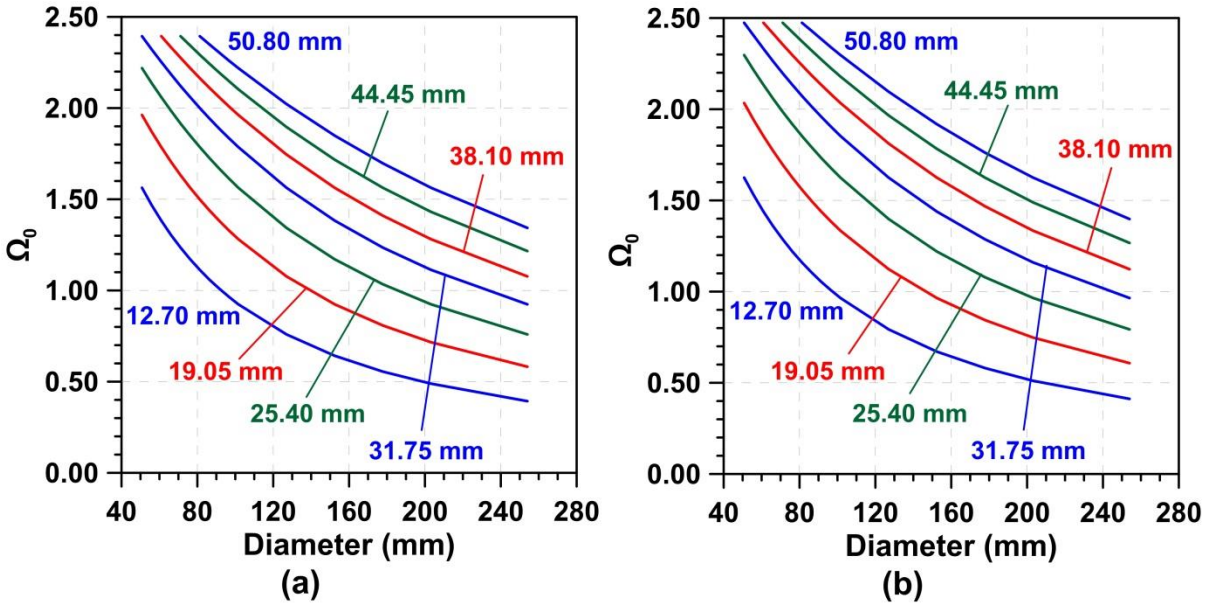

Figure 5-3: Resonance frequency parameter, Ω0, for disks with different diameters and thicknesses. a) ϑ = 0.20, b) ϑ = 0.25.

5.3 Materials and Methods

5.3.1 Materials

Mortar specimens with a water-to-cement ratio (w/c) of 0.42 were produced according to ASTM C192-07. Ordinary Portland Cement (OPC) Type I and natural river sand, with a fineness modulus of 2.65 were used. The mixture contained 55% aggregate by volume. The mortar was cast in 102x204 mm cylindrical model. After 24 hours, the specimens were cut into three 25 mm thick disks. The disk specimens were then cured in lime-saturated water at 23±1°C for 18 months prior to freeze-thaw testing.

5.3.2 Freeze-thaw test

An air-cooled freeze-thaw chamber was used. Each freeze-thaw cycle consisted of a 155 minute cooling period from 20ºC to -35ºC and a 85 minute heating period back to 20ºC. Both heating and cooling periods had two ramps and two constant temperature portions. The constant temperature portions were considered to decrease the difference between the temperature between the core and the surface of the specimen. A thermocouple was embedded in a sample and to monitor the sample core temperature. To keep the samples saturated during freeze-thaw cycles, samples were wrapped in a piece of water saturated cloth and sealed with a plastic wrap (Ghasemzadeh et al. 2015, Li et al. 2012). All the specimens were placed in the freeze-thaw chamber and after each 5 cycles, measurements were performed on them. The specimens are referred to as C0, C5, C10, C15, C25 and C30, where "C" stands for concrete and the number indicates the number of freeze-thaw cycles.

5.3.3 Acoustic emission measurements

A total of three mortar disks were instrumented with acoustic emission (AE) sensors. Sensors with a peak frequency of 375 kHz were used. All samples were placed on an acoustic mat resting on a rigid stainless steel frame to minimize vibration and noise. Two sensors were coupled, using vacuum grease, on the perimeter of the disk at 180º with respect to each other. A stainless steel rod was also used as a reference specimen to monitor the noise from the chamber and possible degradation of coupling agent (Pour-Ghaz et al. 2012).

Passive AE was continuously monitored during the freeze-thaw cycles. Active AE measurements were performed to measure wave travel time at the end of each given number of cycles (similar to ultrasonic pulse velocity). The damage, D, was calculated using Equation 5-16

$$D = 1 - \frac{E_t}{E_0} = 1 - (\frac{t_0}{t_t})^2 \qquad \text{Eq. } 5-16$$

where E_0 and E_t are respectively the elastic modulus before and after freeze-thaw, and t_0 and t_t are the wave travel time before and after freeze-thaw loading respectively.

5.3.4 Nonlinear impact resonance acoustic spectroscopy measurements

Figure 5-4a shows a photograph of the NIRAS test setup. During the measurements the disk was supported on a soft foam mat, allowing a rather "free" vibration of the specimen. The acceleration was induced using steel balls of different weight. Equally a light hammer could be used. A high frequency accelerometer was coupled to the center of the specimen, using a commercial quick bonding adhesive through a small hole in the foam, to measure the vibration of the specimen.

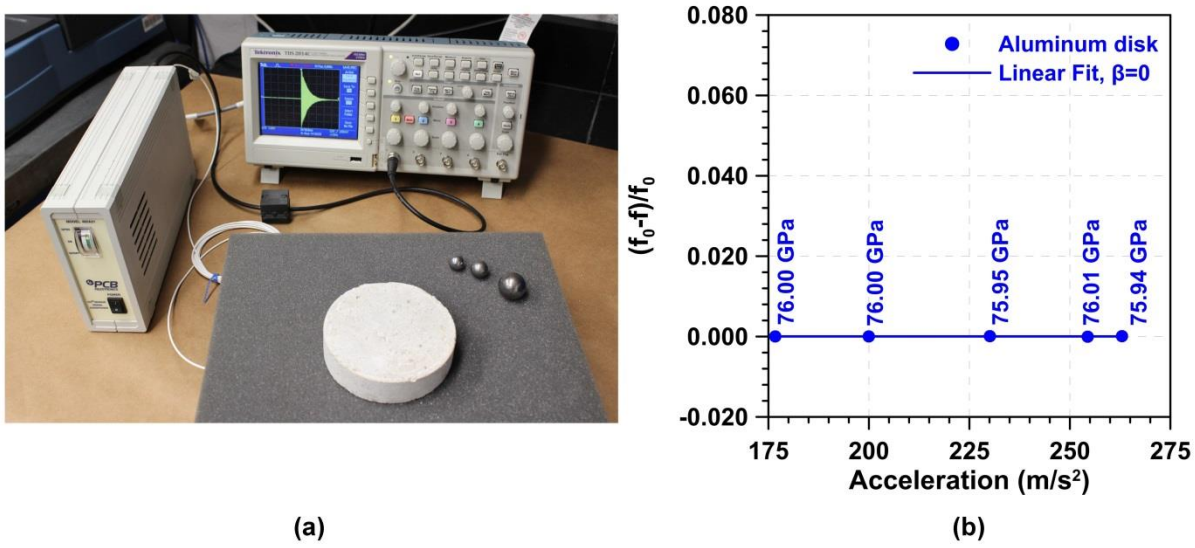

Figure 5-4: a) Nonlinear impact resonance acoustic spectroscopy measurement test setup. b) Aluminum resonance frequency shift and dynamic elastic modulus values.

The linearity of the measurement setup was checked by performing measurements on a 25.4 mm thick aluminum disk with 101.6 mm diameter. The results of these measurements are shown in Figure 5-4b, illustrating linearity of the test setup (i.e., no change in frequency with increased acceleration). The values shown in Figure 5-4b are the calculated elastic modulus from the obtained resonance frequency of the aluminum disk using Equation 5-4. In the calculations, the Poisson's ratio of aluminum was assumed 0.33 and therefore, Ω_0= 1.73 was used. These calculations provide an approximate elastic modulus of 76 GPa for aluminum which is quite an acceptable value.

5.4 Results and discussion

5.4.1 Passive and active acoustic emission

Figure 5-5 illustrates the results of passive AE: the peak amplitude of the captured AE events for the first five cycles and for the last five cycles is shown in **Figure 5-5**a and **Figure 5-5**b respectively. The core temperature of the specimens is also plotted. **Figure 5-5**c illustrates the total number of hits captured at each cycle for all 25 cycles.

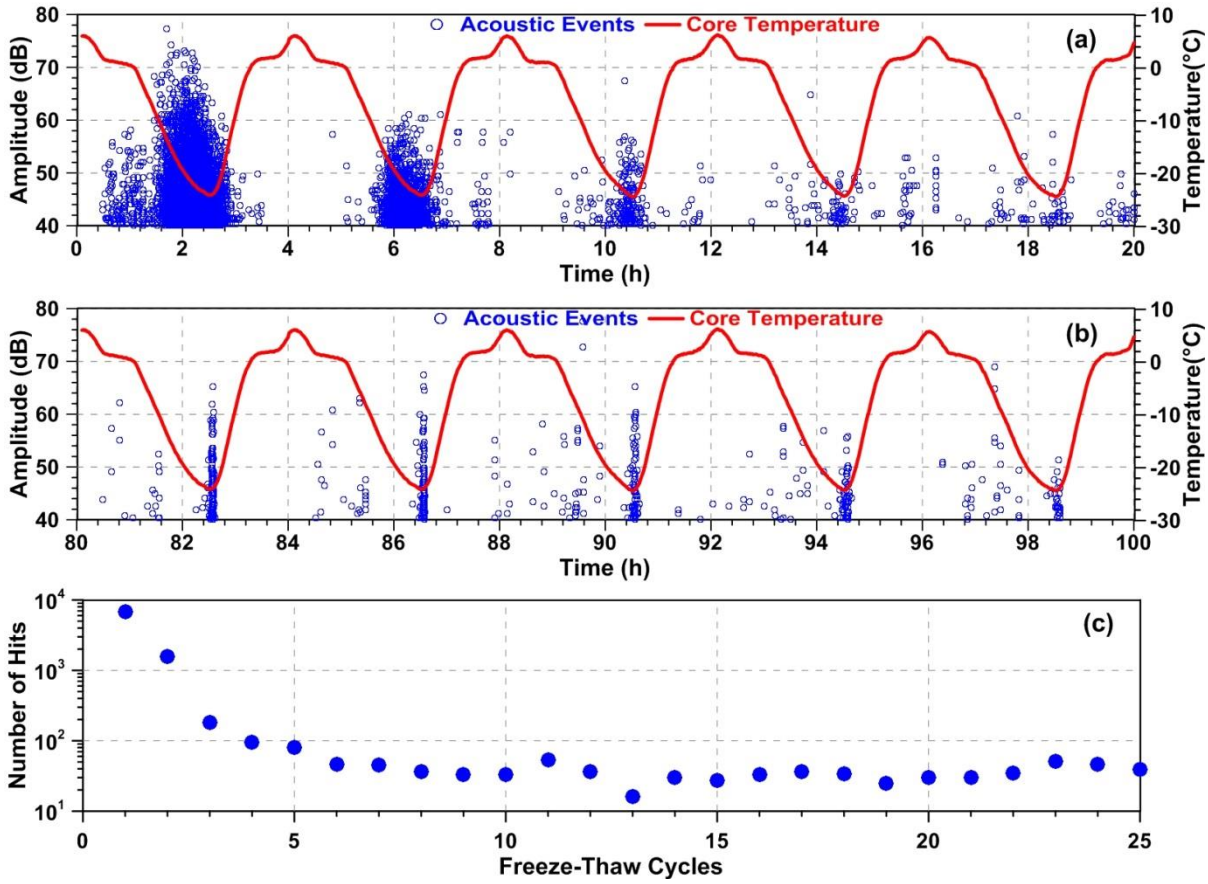

Figure 5-5: Passive acoustic emission: a) for samples during first five cycles. b) for samples during last five cycles. c) Passive acoustic emission events number for all freeze-thaw cycles.

A significantly higher number of AE events are captured during the first few cycles as compared to the subsequent cycles. While passive AE shows the formation of damage, the degree of damage cannot be inferred from these results. Active AE, however, provides a quantitative measure of the damage. The damage measured with active AE is reported in **Table 5-1**. **Table 5-1** also reports the standard deviation of the damage level.

Table 5-1: Damage level measured with active AE

Freeze-Thaw Cycles	Damage level	
	AE Damage (%)	AE Standard Deviation (%)
0	0	0
5	11.73	2.28
10	17.68	4.02
15	29.86	6.29
25	47.67	5.51

Despite the decrease in the number of AE hits after 5 freeze-thaw cycles, the degree of damage continues to increase after 5 cycles as shown in **Table 5-1**. This signifies that the nature of cracks forming in concrete changes at later freeze-thaw cycles: Initially large number of small cracks form and later smaller number of larger and wider cracks forms (Ghasemzadeh et al. 2015).

5.4.2 Nonlinear impact resonance acoustic spectroscopy

The average dynamic elastic modulus computed using the method outlined in section 5.2.2 is reported in **Table 5-2**. Note that, to calculate the dynamic elastic modulus in **Table 5-2** the average value of the frequency is used (i.e., the frequency shift is neglected). The damage in **Table 5-2** is calculated using Equation 5-16. The reported damage is close to the damage estimated based on active AE results in **Table 5-1**. The scatter in the impact resonance data (standard deviation) is smaller than that of AE. Note that in **Table 5-2** the degree of damage for 30 cycles is also reported which is not reported in **Table 5-1**.

Table 5-2: Dynamic elastic modulus and the degree of damage after freeze-thaw loading

Freeze-Thaw Cycles	**Mechanical Properties**		
	Dynamic elastic modulus (GPa)	**Damage (%)**	**Standard Deviation (%)**
0	38.63	0	0.54
5	37.22	3.64	0.17
10	32.65	15.49	1.42
15	27.28	29.37	1.45
25	20.72	46.35	2.31
35	14.13	63.41	0.23

Figure 5-6 illustrates the change in the normalized frequency shift with increased acceleration (**Figure 5-6**a) and the change in the normalized Q-factor shift with acceleration (**Figure 5-6**b). Both parameters increase linearly with acceleration. The slope of the linear lines in **Figure 5-6**a is the nonlinear elasticity parameter, β, and the slope of the linear lines in **Figure 5-6**b, η, are the nonlinear Q-factor parameter. The values of β and η are shown in each graph.

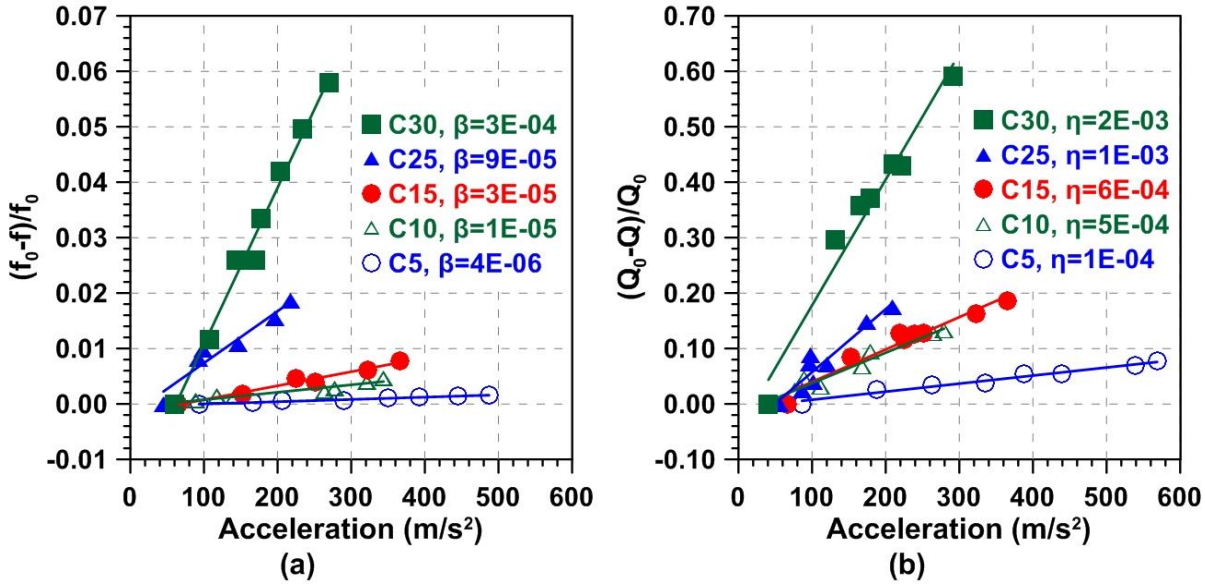

Figure 5-6: a) Normalized resonance frequency shift and b) normalized Q-factor shift, with increased accelerations.

Figure 5-7 illustrates the change of β and η with damage (from **Table 5-2**). These results clearly shown that while β increases exponentially with damage ($log(\beta)$ increases linearly with damage), η increases linearly with damage.

The data in **Figure 5-7** suggests that both β and η can be used to obtain an estimate of damage in the absence of prior knowledge about the undamaged properties of materials. The value of β and η might be dependent on the properties of the concrete mixture, such as paste and aggregate content, and therefore, the plots in **Figure 5-7** may not be generalized to all concrete materials. However, since the actual elastic module of the material is calculated, per section 5.2.2, a more informed interpretation of values of β and η can be achieved.

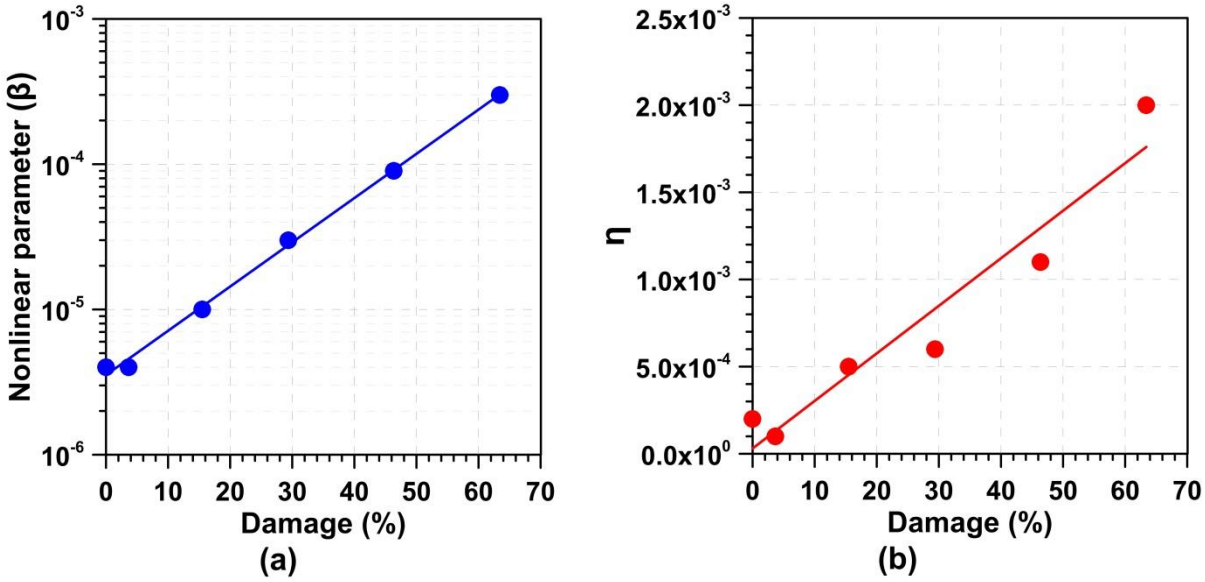

Figure 5-7: (a) Increase of nonlinear parameter **β** with damage, (b) Change in nonlinear Q-factor parameter **η** with damage.

5.5 Chapter Conclusion

Freeze-thaw damage was evaluated in concrete using passive acoustic emission, active acoustic emission, and nonlinear impact resonance acoustic spectroscopy. The results indicate an exponential increase of nonlinear elasticity parameter, β, and a linear increase of nonlinear Q-factor parameter, η, with damage. The actual value of elastic modules calculated based on axisymmetric flexural vibration of a thick circular plate, and the values of β and η can be used to estimate damage in the absence of prior knowledge about the undamaged properties of materials.

6. Conclusions

The research reported in this dissertation provides more insight to the effect of damage on moisture transport properties of concrete. This study included an extensive experimental program on moisture transport in saturated and unsaturated damaged cement-based materials. Analytical study and numerical modeling are also used to determine the parameters that have significant effect on the mass transport. Based on the investigation on the effect of damage on moisture transport in concrete and findings of this research, the following conclusions and recommendations can be drawn:

1. The initial sorptivity increases linearly with degree of damage because (i) cracks act as capillary tubes that absorb water rapidly, (ii) cracks provide access to capillary pores within the specimen and away from the exposed surface (preferential flow paths), and (iii) cracks provide access to the larger air-filled pores, and therefore, some of these air-filled voids are filled with water during the initial sorption period resulting in higher initial sorption rate.
2. The secondary sorptivity initially decreases with damage, and then remains almost constant because cracks provide access to the larger air-filled voids and therefore some of these air-filled voids are filled with water during the initial sorption period leaving a smaller fraction of these air-filled voids empty for the secondary sorption period.

3. The results of passive acoustic emission, scanning electron microscope, saturated hydraulic conductivity, and a simple damage mechanics based model collectively indicate that initially a larger number of cracks develop within the material with freeze-thaw loading. At the later cycles of freeze-thaw, a smaller number of cracks develop, but the average crack width increases. This gives rise to exponential increase of saturated hydraulic conductivity with degree of damage.
4. The Electrical resistivity shows a slight bilinear decreased with damage: The electrical resistivity initially decreases with a higher rate due to the formation of cracks and then the rate of decrease of resistivity decreases with further damage development since in the later stages the connectivity is enhanced but smaller number of new cracks are developed. The conceptual damage model developed approximates the bilinear decrease with a linear decrease.
5. In general, damage in the form of distributed cracking increases the rate of moisture transport. Investigates It appears that saturated hydraulic conductivity is much more sensitive parameter to damage as compared to sorption and electrical resistivity. The conceptual model developed supports this observation by showing the higher dependence of saturated hydraulic conductivity to crack width.
6. In this work, classical isothermal unsaturated moisture transport model was used to simulate moisture ingress in mortar and concrete with a wide range of damage. The required material parameters for the simulations were experimentally obtained. The results indicate that, for all levels of damage, the classical isothermal unsaturated moisture transport model simulates the early stages of moisture ingress in mortar and

concrete where capillary suction is the underlying mechanism. At later stages where air diffusion and dissolution mechanisms play a more significant role, the results of simulation deviate from experimental measurements. The use of more advanced material models might be necessary to obtain more accurate results.

7. Different measurement methods differently reflect the effect of damage on mass transport depending on the mechanism of transport utilized in the measurement method. Different methods also show different sensitivity to the presence of damage. Rapid chloride permeability test and electrical resistivity are only sensitive at low damage levels (below 20%). Initial sorptivity increases linearly with damage at all levels. Water and air permeability increase exponentially with damage and seem to be the most sensitive parameter to the presence of damage.
8. The results indicate an exponential increase of nonlinear elasticity parameter, β, and a linear increase of nonlinear Q-factor parameter, η, with damage. The actual value of elastic modules, calculated based on axisymmetric flexural vibration of a thick circular plate, and the values of β and η can be used to estimate damage in the absence of prior knowledge about the undamaged properties of materials.
9. It is recommended to modify existing concrete service prediction models based on the crack development (damage formation) during service.
10. Since damage does not generally form uniformly in concrete, it is recommended to investigate or model the change in transport properties of layered damage in concrete. It would be helpful to more accurately predict the service life of concrete structures (e.g. concrete pavements).

11. It is recommended to investigate the effect of change in transport properties of damaged concrete subjected to deicing salts.

Refrences

Akhavan, A., & Rajabipour, F. (2013). "Evaluating ion diffusivity of cracked cement paste using electrical impedance spectroscopy." Materials and Structures, 46(5), 697-708.

Akhavan, A., Shafaatian, S. M. H., & Rajabipour, F. (2012). "Quantifying the effects of crack width, tortuosity, and roughness on water permeability of cracked mortars." Cement and Concrete Research, 42(2), 313-320.

Aldea, C. M., Shah, S. P., & Karr, A. (1999a). "Effect of cracking on water and chloride permeability of concrete." Journal of Materials in Civil Engineering, 11(3), 181-187.

Aldea, C. M., Shah, S. P., & Karr, A. (1999b). "Permeability of cracked concrete." Materials and Structures, 32(5), 370-376.

Andrade C. (1993). "Calculation of chloride diffusion coefficients in concrete from ionic migration measurements." Cement and Concrete Research, 23(3): 724-742.

Antonaci, P., Bruno, C., Bocca, P., Scalerandi, M., and Gliozzi, A. (2010). "Nonlinear ultrasonic evaluation of load e_ects on discontinuities in concrete." Cement and Concrete Research, 40(2), 340-346.

Barde, V., Radlinska, A., Cohen, M., & Weiss, W. J. (2009). "Relating material properties to exposure conditions for predicting service life in concrete bridge decks in Indiana." JTRP Technical Reports, Purdue University.

Bentz, D. P., Ehlen, M. A., Ferraris, C. F., & Garboczi, E. J. (2001). "Sorptivity-based service life predictions for concrete pavements." In7th International Conference on Concrete Pavements– Purdue University, West Lafayette, IN.

Bentz, D. P., Garboczi, E. J., Lu, Y., Martys, N., Sakulich, A. R., & Jason Weiss, W. (2013). "Modeling of the influence of transverse cracking on chloride penetration into concrete." Cement and Concrete Composites, 38, 65-74.

Bentz, E., & Thomas, M. D. A. (2001). "Life-365 service life prediction model." Computer Program for Predicting the Service Life and Life-Cycle Costs of Reinforced Concrete Exposed to Chlorides, University of Toronto.

Brooks, R. J., and Corey, A. T. (1964). "Hydraulic properties of porous media." Hydrology papers 3, Colorado State University, Fort Collins, Colorado.

Brosnan DA, & Robinson GC. (2003). "An introduction to drying of ceramics." The American Ceramic Society, Westerville, Ohio.

Cao, H. and Yue, X. (2014). "Homogenization of Richards' equation of van Genuchten–Mualem model." Journal of Mathematical Analysis and Applications., 391-400.

Castro, J., Bentz, D., & Weiss, J. (2011a). "Effect of sample conditioning on the water absorption of concrete." Cement and Concrete Composites, 33(8), 805-813.

Castro, J., Spragg, R., & Weiss, J. (2011b). "Water absorption and electrical conductivity for internally cured mortars with a W/C between 0.30 and 0.45." Journal of Materials in Civil Engineering, 24(2), 223-231.

Charbeneau, R. J. (2006). "Groundwater hydraulics and pollutant transport." Waveland Press: Long Grove, Illinois.

Chen, J. and Zhang, L. (2015). "Experimental study of effects of water-cement ratio and curing time on nonlinear resonance of concrete." Materials and Structures, 48(1-2), 423-433.

Chen, J., Jayapalan, A., Kim, J., Kurtis, K., and Jacobs, L. (2010). "Rapid evaluation of alkali-silica reactivity of aggregates using a nonlinear resonance spectroscopy technique." Cement and Concrete Research, 40, 914-923.

Chen, J., Kim, J., Kurtis, K., and Jacobs, L. (2011). "Theoretical and experimental study of the nonlinear resonance vibration of cementitious materials with an application to damage characterization." Journal of the Acoustical Society of America, 130(5), 2728-2737.

Chen, X., Kim, J., Kurtis, K., Qu, J., Shen, C., and Jacobs, L. (2008). "Characterization of progressive microcracking in portland cement mortar using nonlinear ultrasonics." Nondestructive Testing and Evaluation International, 41(2), 112-118.

Chung, C. W., Shon, C. S., & Kim, Y. S. (2010). "Chloride ion diffusivity of fly ash and silica fume concretes exposed to freeze–thaw cycles." Construction and Building Materials, 24(9), 1739-1745.

Chunsheng, Z., Li, K., & Pang, X. (2012). "Geometry of crack network and its impact on transport properties of concrete." Cement and Concrete Research, 42(9), 1261-1272.

Culligan, P. J., Barry, D. A., Parlange, J., Steenhuis, T. S., & Haverkamp, R. (2000). "Infiltration with controlled air escape." Water Resources Research, 36(3), 781-785.

De la Varga I, Spragg R, Bella CD, Castro J, Bentz DP, and Weiss J. (2014). "Fluid transport in high volume fly ash mixtures with and without internal curing." Cement and Concrete Composites, 45: 102-110.

Dilek U, & Leming ML. (2008). "Elastic dynamic Young's modulus and permeability of concrete in fire damaged structural members." Journal of Materials in Civil Engineering, 20(2): 102-110.

Djerbi, A., Bonnet, S., Khelidj, A., & Baroghel-Bouny, V. (2008). "Influence of traversing crack on chloride diffusion into concrete." Cement and Concrete Research, 38(6), 877-883.

Eiras, J., Kundu, T., Bonilla, M., and Paya, J. (2013a). "Nondestructive monitoring of ageing of alkali resistant glass fiber reinforced cement (grc)." Journal of Nondestructive Evaluation, 32, 300-314.

Eiras, J., Kundu, T., Popovics, J., Monzo, J., Borrachero, M., and Paya, J. (2013b). "Monitoring material nonlinearity and attenuation vibrations in mortar subjected to freezing-thawing cycles." Journal of the Acoustical Society of America, 134(5), http://dx.doi.org/10.1121/1.4831063.

Eiras, J., Monzo, J., Paya, J., Kundu, T., and Popovics, J. (2014). "Non-classical nonlinear feature extraction from standard resonance vibration data for damage detection." Journal of Acoustical Society of America, 135(2), http://dx.doi.org/10.1121/1.4862882.

Eiras, J., Popovics, J., Borrachero, M., Monzo, J., and Paya, J. (2012). "Nonlinear impact resonant acoustic spectroscopy to discern mechanical damage in cement based materials." 15th International Conference on Experimental Mechanics, Porto, Portugal.

Fagerlund G. (2012). "Effect of water-cement ratio, air content and age on the risk of frost damage of concrete." Report TVBM-3163, Lund Institute of Technology, Lund University.

Fagerlund, G. (1973). "Determination of pore-size distribution from freezing-point depression." Matériaux et Construction, 6(3), 215–225.

Fagerlund, G. (1977). "The international cooperative test of the critical degree of saturation method of assessing the freeze/thaw resistance of concrete." Materials and Structures, 10(4), 231-253.

Fagerlund, G. (1996). "Predicting the service life of concrete exposed to frost action through a modelling of the water absorption process in the air-pore system" H. Jennings, J. Kropp, K. Scrivener (Eds.), The modeling of microstructure and its potential for studying transport properties and durability, Springer Netherlands, 503–537.

Fagerlund, G. (1997). “On the service life of concrete exposed to frost action.” Freeze-thaw durability of concrete, J. Marchand, M. Pigeon and M. J. Setzer, eds., E & FN Spon, London, 23–42.

Fagerlund, G. (2012), “Effect of water-cement ratio, air content and age on the risk of frost damage of concrete.” Report TVBM-3163, Lund Institute of Technology, Lund University.

Farnam Y., Bentz D., Sakulich A., Flynn D., Weiss J. (2014). “ Measuring freeze and thaw damage in mortars containing deicing salt using a low-temperature longitudinal guarded comparative calorimeter and acoustic emission.” Advances in Civil Engineering Materials, 3(1), DOI: http://dx.doi.org/10.1520/ACEM20130095.

Ghasemzadeh F, Sajedi S, Shekarchi M, Layssi H, and Hallaji M. (2013) “Performance Evaluation of Different Repair Concretes Proposed for an Existing Deteriorated Jetty Structure.” Journal of Performance of Constructed Facilities 28(4): 04014013.

Ghassemzadeh F, Shekarchi M, Sajedi S, Khanzadeh M, and Sadati S. (2010). “Effect of silica fume and GGBS on shrinkage in the high performance concrete.” In Sixth International Conference on Concrete under Severe Conditions: Environment and Loading. 2010.

Ghasemzadeh, F., Pour-Ghaz, M. (2014). “The effect of damage on moisture transport in concrete.” Journal of Material in Civil Engineering., DOI: 10.1061/(ASCE)MT.1943-5533.0001211.

Ghasemzadeh, F., Rashetnia, R., and Pour-Ghaz, M. “Methods to evaluate transport in damaged mortar.” Cement and Concrete Composites, Submitted.

Green, W. H., & Ampt, G. A. (1911). “Studies on soil physics, 1. The flow of air and water through soils.” Journal of Agriculture Science, 4(1), 1-24.

Gérard B, and Marchand J. (2000). “Influence of cracking on the diffusion properties of cement-based materials: Part I: Influence of continuous cracks on the steady-state regime.” Cement and Concrete Research, 30(1): 37-43.

Halaji M, Seppänen A, & Pour-Ghaz M. (2015). “Electrical resistance tomography to monitor unsaturated moisture flow in cementitious materials.” Cement and Concrete Research. 69(March): 10-18.

Hall, C. (1989). “Water sorptivity of mortars and concrete: a review.” Magazine of Concrete Research., 51–61.

Hall, C. (1994). “Barrier performance of concrete: a review of fluid transport theory.” Materials and Structures, 27(5), 291-306.

Hall, C., & Hoff, W. D. (2011). "Water transport in brick, stone and concrete." CRC Press Hall, Boca Raton, Florida, DOI: 10.1201/b12840-15.

Hall, C., Hoff, W. D., Taylor, S. C., Wilson, M. A., Yoon, B. G., Reinhardt, H. W., Sosoro, M., Meredith, P., and Donald, A. M. (1995). "Water anomaly in capillary liquid absorption by cement-based materials." Journal of Materials Science Letters, 14(17), 1178-1181.

Hanžič, L., Kosec, L., & Anžel, I. (2010). "Capillary absorption in concrete and the Lucas–Washburn equation." Cement and Concrete Composites, 32(1), 84-91.

Hearn, N. (1999). "Effect of shrinkage and load-induced cracking on water permeability of concrete." ACI Materials Journal., 234–240.

Helmuth, R. A. (1960). "Capillary size restrictions on ice formation in hardened Portland cement pastes." In proceeding of the 4th International Symposium on Chemistry of Cement, Paper VI-S2, Portland Cement Association, Research and Development Laboratories, Skokie, IL, 855–869.

Henchi, K., Samson, E., Chapdelaine, F., & Marchand, J. (2007). "Advanced finite-element predictive model for the service life prediction of concrete infrastructures in support of asset management and decision-making." In Computing in Civil Engineering, ASCE, Pittsburgh, USA, 870-880.

Hutchinson, J. (1979). "Axisymmetric exural vibrations of a thick free circular plate." Journal of Applied Mechanics, 46(1), 139-144.

Jacobsen, S., Marchand, J., & Boisvert, L. (1996). "Effect of cracking and healing on chloride transport in OPC concrete." Cement and Concrete Research, 26(6), 869-881.

Jakobsen, U., H., (1998). "Understanding the features observed in concrete using various fluorescence impregnation techniques." In Proceedings of the Twentieth International Conference on Cement Microscopy, Guadalajara, Mexico, 19-23.

Johnson, P. and Sutin, A. (2005). "Slow dynamics and anomalous nonlinear fast dynamics in diverse solids." Journal of the Acoustical Society of America, 117(1), 124-130.

Johnson, P., Zinszner, B., and Rasolofosaon, P. (1996). "Resonance and elastic nonlinear phenomena in rock." Journal of Geophysical Research, 101, 11553-11564.

Kim B, and Weiss WJ. (2003). "Using acoustic emission to quantify damage in restrained fiber-reinforced cement mortars." Cement and Concrete Research, 33(2): 207-214.

Kim, J., Jacobs, L., Qu, J., and Littles, J. (2006a). "Experimental characterization of fatigue damage in a nickel-base superalloy using nonlinear ultrasonic waves." Journal of the Acoustical Society of America, 120(3), 1266-1273.

Kim, J., Qu, J., Jacobs, L., Littles, J., and Savage, M. (2006b). "Acoustic nonlinearity parameter due to microplasticity." Journal of Nondestructive Evaluation, 25(1), 28-36.

Kober, J. and Prevorovsky, Z. (2012). "Nonlinear wave modulation spectroscopy: Quasistatic solution and experimental evidence." XVII International Conference on Nonlinear Elasticity in Materials, Sicily, Italy.

Kodjo, A., Rivard, P., Cohen-Tenoudji, F., and Gallias, J. (2009). "Evaluation of damages due to alkali-silica reaction with nonlinear acoustics techniques." XIV International Conference on Nonlinear Elasticity in Materials, Lisbon, Portugal.

Kosugi, K. (1996). "Lognormal distribution model for unsaturated soil hydraulic properties." Water Resources Research., 2697-2703.

Kosugi, K. (1999). "General model for unsaturated hydraulic conductivity for soils with lognormal pore-size distribution." Soil Science Society of America Journal., 270-277.

Langton, C. (2012). "Transport through cracked concrete: literature review." Funding organisation: US Department of Energy (United States), Savannah River Site (SRS), Aiken, SC, USA.

Leech, C., Lockington, D., Hooton, R. D., Galloway, G., Cowin, G., and Dux, P. (2008). "Validation of mualem's conductivity model and prediction of saturated permeability from sorptivity." ACI Materials Journal, V. 105, No. 1. 44-51.

Lemaitre, J., & Lippmann, H. (1996). "A course on damage mechanics." Berlin: Springer.

Leming, L., Nau, J., and Fukuda, J. (1998). "Non-destructive determination of the dynamic modulus of concrete disks." Materials Journal, 95(1), 50-57.

Lesnicki, K., Kim, J., Kurtis, K., and Jacobs, L. (2011). "Characterization of asr damage in concrete using nonlinear impact resonance acoustic spectroscopy technique." Nondestructive Testing and Evaluation International, 44(8), 721-727.

Lesnicki, K., Kim, J., Kurtis, K., and Jacobs, L. (2013). "Assessment of alkali-silica reaction damage through quanti_cation of concrete nonlinearity." Materials and Structures, 46(3), 497-509.

Li, W., Pour-Ghaz, M., Castro, J., & Weiss, J. (2011). "Water absorption and critical degree of saturation relating to freeze-thaw damage in concrete pavement joints." Journal of Materials in Civil Engineering, 24(3), 299-307.

Lockington, D., Parlange, J. Y., & Dux, P. (1999). "Sorptivity and the estimation of water penetration into unsaturated concrete." Materials and Structures, 32(5), 342-347.

M'Jahad S, Davy CA, Bourbon X, and Skoczylas F. (2014). "Water Retention and Gas Migration of Two High Performance Concretes after Damage." Journal of Materials in Civil Engineering, DOI: 10.1061/(ASCE)MT.1943-5533.0001028.

Martys, N. S., & Ferraris, C. F. (1997). "Capillary transport in mortars and concrete." Cement and Concrete Research, 27(5), 747-760.

Moradi-Marani, F., Kodjo, S., Rivard, P., and Lamarche, C. (2014). "Nonlinear acoustic technique of time shift for evaluation of alkali-silica reaction damage in concrete structures." Materials Journal, 111(5), 581-592.

Mualem, Y. (1976). "A new model for predicting the hydraulic conductivity of unsaturated porous media." Water Resources Research., 513-513.

Neuman, S. P. (1976). "Wetting front pressure head in the infiltration model of Green and Ampt." Water resources research, 12(3), 564-566.

Parlange, J., Barry, D., Parlange, M., Hogarth, W., Haverkamp, R., Ross, P., Steenhuis, T. (1997). "New approximate analytical technique to solve Richards Equation for arbitrary surface boundary conditions." Water Resources Research., 903-903.

Parlange, J., Hogarth, W., Barry, D., Parlange, M., Haverkamp, R., Ross, P., Katul, G. (1999). "Analytical approximation to the solutions of Richards' equation with applications to infiltration, ponding, and time compression approximation." Advances in Water Resources., 189-194.

Parrott, L. J. (1994). "Moisture conditioning and transport properties of concrete test specimens." Materials and Structures, 27(8), 460-468.

Parrott, L.J. (1991). "Factor influencing relative humidity in concrete." Magazine Concrete Research; 43(154): 45-52.

Picandet, V., Khelidj, A., & Bellegou, H. (2009). "Crack effects on gas and water permeability of concretes." Cement and Concrete Research, 39(6), 537-547.

Pour-Ghaz M, Rajabipour F, Couch J, and Weiss J. (2009). "Modeling fluid transport in cementitious systems with crack-like (notch) geometries." In Proceedings of the 2nd international RILEM workshop on concrete durability and service life planning, Haifa, Israel.

Pour-Ghaz M, Spragg R, & Weiss J. (2010). "Moisture profiles and diffusion coefficients in mortars containing shrinkage reducing admixtures." In O. M. Jensen, M. T. Hasholt, & S. Laustsen (Eds.), International RILEM conference on use of superabsorbent polymers and other new additives in concrete. Technical University of Denmark, Lyngby, Denmark.

Pour-Ghaz M. (2011). "Detecting damage in concrete using electrical methods and assessing moisture movement in cracked concrete." Ph.D. thesis, Purdue Univ., West Lafayette, IN.

Pour-Ghaz M., Rajabipour F, Couch J, and Weiss J. (2009). "Numerical and experimental assessment of unsaturated fluid transport in saw-cut (notched) concrete elements." ACI special publication, 266.

Pour-Ghaz, M. (2011). "Detecting damage in concrete using electrical methods and assessing moisture movement in cracked concrete." PhD Thesis, Purdue University, Indiana.

Pour-Ghaz, M. (2014). "Modelling behaviour of Infrastructure Materials." Lecture notes, North Carolina State University, Department of Civil Construction and Environmental Engineering.

Pour-Ghaz, M., Castro, J., Kladivko, E. J., & Weiss, J. (2011). "Characterizing lightweight aggregate desorption at high relative humidities using a pressure plate apparatus." Journal of Materials in Civil Engineering, 24(8), 961-969.

Pour-Ghaz, M., Rajabipour, F., Couch, J., & Weiss, J. (2009a). "Modeling fluid transport in cementitious systems with crack-like (notch) geometries." In Proceedings of the 2nd international RILEM workshop on concrete durability and service life planning, Haifa, Israel.

Pour-Ghaz, M., Rajabipour, F., Couch, J., & Weiss, J. (2009b). "Numerical and experimental assessment of unsaturated fluid transport in saw-cut (notched) concrete elements." ACI special publication, 266, 73-86.

Pour-Ghaz, M., Rajabipour, F., Couch, J., and Weiss, W. J. (2009c). "Modeling fluid transport in cementitious systems with crack-like (notch) geometries." Proceedings of the 2nd International RILEM Workshop on Concrete Durability and Service Life Planning, Haifa, Israel.

Pour-Ghaz, M., Spragg R., Weiss J. (2010). "Moisture profiles and diffusion coefficients in mortars containing shrinkage reducing admixtures." International RILEM Conference on Use

of Superabsorbent Polymers and Other New Additives in Concrete. Technical University of Denmark, Lyngby, Denmark., 197-206.

Pour-Ghaz, M., Spragg, R., Castro, J., and Weiss, J. (2012). "Can acoustic emission be used to detect alkali silica reaction earlier than length change test?." Proceeding of the 14th International Conference on Alkali-Aggregate Reaction in Concrete, University of Texas; Austin, Texas.

Poyet, S., Charles, S., Honore, N., L'hostit, V. (2011). "Assessment of unsaturated water transport properties in an old concrete: determination of the pore-interaction factor." Cement and Concrete Research., 1015-1023.

Rajabipour, F. (2006). "Insitu electrical sensing and material health monitoring in concrete structures." Doctoral dissertation, Purdue University.

Rashetnia R, Ghasemzadeh F, & Pour-Ghaz M. (2015). "Quantifying freeze-thaw damage in concrete using nonlinear acoustic spectroscopy." NDT & E International, Underreview.

Recalde, J. and Leming, M. (2009). "Changes in uid penetrability and mechanical properties of concrete due to high temperature exposure." Journal of ASTM International, 6(6), doi: 10.1520/JAI101326.

Reinhardt, H. W., & Jooss, M. (2003). "Permeability and self-healing of cracked concrete as a function of temperature and crack width." Cement and Concrete Research, 33(7), 981-985.

Richards, L. A. (1931). "Capillary conduction of liquids through porous mediums." Physics1.

Rodriguez, O. G., & Hooton, R. D. (2003). "Influence of cracks on chloride ingress into concrete." ACI Materials Journal, 100(2), 120-126.

Saito, M., Ohta, M., & Ishimori, H. (1994). "Chloride permeability of concrete subjected to freeze-thaw damage." Cement and Concrete Composites, 16(4), 233-239.

Sajedi, S, Bonyadi HR, Ghassemzadeh F, Shekarchi M, and Mohebbi MJ. (2011). "Finite element investigation of the flexural behavior of corroded RC beams before and after repairing." In First Middle East Conference on Smart Monitoring, Assessment and Rehabilitation of Civil Structures.

Samaha, H. R. and Hover, K. (1992). "Influence of microcracking on the mass transport properties of concrete." ACI Materials Journal., 416-424.

Schaap, M., Leij, F. (2000). "Improved prediction of unsaturated hydraulic conductivity with the Maulem-van Genuchten model." Soil Science Society of America Journal., 843-851.

Schneider, S., Mallants, D., Jacques, D. (2012). "Determining hydraulic properties of concrete and mortar by inverse modeling." Materials Research Society Symposium.

Schonlin K, and Hilsdorf HK. (1988). "Permeability as a measure of potential durability of concrete development of a suitable test apparatus." Permeability of concrete, ACI SP-108, D. Whiting and A. Walitt.

Schuh, W.M and Cline, R.L. (1990). "Effect of soil properties on unsaturated hydraulic conductivity pore-interaction factors." Soil Science Society of America Journal., 1509-1519.

Sejna, M., Simunek, J., van Genuchten, M. Th. (2014). "The HYDRUS software package for simulating the two- and three-dimensional movement of water, heat, and multiple solutes in variably-saturated porous media." http://www.pc-progress.com/en/. .%5Cdownloads%5CPgm_Hydrus3D2%5CHYDRUS3D%20User%20Manual.pdf.

Shekarchi M, Sajedi S, Ghasemzadeh S, Razavizadeh SA, and Manafpour A. (2012a) "Numerical investigation on the effectiveness of patch repair on the flexural behavior of corroded post-tensioned beams." In Concrete Repair, Rehabilitation and Retrofitting III: 3rd International Conference on Concrete Repair, Rehabilitation and Retrofitting, ICCRRR-3, 3-5 September 2012, Cape Town, South Africa, p. 417. CRC Press.

Shekarchi M, Ghasemzadeh F, and Sajedi S. (2012b) "Inverse analysis method for concrete shrinkage prediction from short-term tests." ACI Materials Journal 109(3).

Shimada, H., Sakai, K., & Litvan, G. G. (1991). "Acoustic emissions of mortar subjected to freezing and thawing." ACI Special Publication, 126, DOI: 10.14359/2159.

Smyl D, Ghasemzadeh F, & Pour-Ghaz M. (2015). "Numerical simulation of unsaturated moisture transport in damaged mortar and concrete." Journal of Materials in Civil Engineering, ASCE, Underreview.

Snyder KA, Ferraris C, Martys NS, & Garboczi EJ. (2000). "Using impedance spectroscopy to assess the viability of the rapid chloride test for determining concrete conductivity." Journal of Research-National Institute of Standard and Technology. 105 (4): 497-510.

Spiesz P, & Brouwers HJH. (2012). "Influence of the applied voltage on the Rapid Chloride Migration (RCM) test." Cement and Concrete Research, 42(8): 1072-1082.

Spragg RP, Castro J, Nantung TE, Paredes M, and Weiss WJ. (2011). "Variability analysis of the bulk resistivity measured using concrete cylinders." Joint Transportation Research Program Technical Rep., Purdue Univ., West Lafayette, IN.

Syml, D., Ghasemzadeh, F., Hallaji, M., Pour-Ghaz, M. (2014). "Modeling unsaturated flow in damage concrete" Report, North Carolina State University. Materials and Sensor Development Laboratory.

Thomas, M. D. A., & Bentz, E. C. (2000). "Life-365 computer program for predicting the service life and life-cycle costs of reinforced concrete exposed to chlorides." American Concrete Institute, Committee, 365.

Tognazzi, C., Ollivier, J.-P., Carcasses, M., and Torrenti, J.-M., 1998, ''Couplage fissuration-de´gradation chimique des mate´riaux cimentaires: Premiers re´sultats sur les proprie´te´s de transfert.'' Ouvrages, ge´omate´riaux et interactions, Ch. Petit, G. Pijaudier-Cabot, and J. M. Reynouard, eds., Herme`s, Paris, 69–84.

Torquato, S. (2002). Random heterogeneous materials: microstructure and macroscopic properties (Vol. 16). Springer.

Torrijos MC, Giaccio G, and Zerbino R. (2010). "Internal cracking and transport properties in damaged concretes." Materials and structures, 43(1): 109-121.

Van Den Abeele, K., Carmeliet, J., Ten Cate, J., and Johnson, P. (2000a). "Nonlinear elastic wave spectroscopy (news) techniques to discern material damage, part ii: single-mode nonlinear resonance acoustic spectroscopy." Research in Nondestructive Evaluation, 12, 31-42.

Van Den Abeele, K., Johnson, P., and Sutin, A. (2000b). "Nonlinear elastic wave spectroscopy (news) techniques to discern material damage, part i: Nonlinear wave modulation spectroscopy (nwms)." Research in Nondestructive Evaluation, 12, 17-30.

Van Genuchten, M. T. (1980). A closed-form equation for predicting the hydraulic conductivity of unsaturated soils. Soil Science Society of America Journal, 44(5), 892-898.
Van Genuchten, M. Th, Nielsen, D. R. (1985). "On describing and predicting the hydraulic properties of unsaturated soils." Annals of Geophysics., 615-628.

Van Genuchten, M. Th. (1980). "A closed-form equation for predicting the hydraulic conductivity of unsaturated soils." Soil science Society of America Journal., 892-898.

Villani C, Loser R, West MJ, Bella CD, Lura P, Weiss J. (2014). "An inter lab comparison of gas transport testing procedures: Oxygen permeability and oxygen diffusivity." Cement and Concrete Composites, 53(October): 357–366.

Villani C, Spragg R, Pour-Ghaz M, and Weiss WJ. (2014). "The Influence of Pore Solutions Properties on Drying in Cementitious Materials." Journal of the American Ceramic Society, 97(2), 386-393.

Wang L, and Ueda T. (2014). "Mesoscale modelling of the chloride diffusion in unsaturated concrete damaged by freeze-thaw cycling." Journal of Material in Civil Engineering, 26(5): 955-965.

Wang, K., Jansen, D. C., Shah, S. P., & Karr, A. F. (1997). "Permeability study of cracked concrete." Cement and Concrete Research, 27(3), 381-393.

Wang, Z., Feyen, J., Genuchten, M. T., & Nielsen, D. R. (1998). Air entrapment effects on infiltration rate and flow instability. Water Resources Research, 34(2), 213-222.

Warrick, A., Islas, A., Lomen, D. (1997). "An analytical solution to Richards' equation for time-varying infiltration." Water Resources Research., 763-766.

Weiss, W. J. (1999). Prediction of early-age shrinkage cracking in concrete elements. Thesis (Ph.D.), Northwestern University.

Wiens, U., Meng, B., Schroeder, P., & Schiessl, P. (1997). "Micro-cracking in High-Performance Concrete-From Model to the Effect on Concrete Properties." Self-Desiccation and Its Importance on Concrete Technology, Ed. B. Persson, G. Fagerlund, Lund, Sweden, pp193-208.

Wilson, M., Carter, M., Hoff, W. (1999). "British standard and RILEM water absorption tests: A critical evaluation." Materials and Structures., 571-578.

Witherspoon, P. A., Wang, J. S. Y., Iwai, K., & Gale, J. E. (1980). Validity of cubic law for fluid flow in a deformable rock fracture. Water Resources Research, 16(6), 1016-1024.

Wittke, W. (1990). "Rock mechanics: theory and applications, with case histories." Springer-Verlag.

Xi, Y., & Bazant, Z. P. (1999). "Modeling chloride penetration in saturated concrete." Journal of Materials in Civil Engineering, 11(1), 58-65.

Yang Z, Weiss WJ, and Olek J. (2006). "Water transport in concrete damaged by tensile loading and freeze–thaw cycling." Journal of materials in civil engineering, 18(3): 424-434.

Yang, Z. (2004). Assessing cumulative damage in concrete and quantifying its influence on life cycle performance modeling (Doctoral dissertation, Purdue University).

Yang, Z., Weiss, J., & Olek, J. (2005). "Interaction Between Micro-cracking, Cracking, and Reduced Durability of Concrete: Developing Methods for Considering Cumulative Damage in

Life-Cycle Modeling." Report FHWA/IN/JTRP-2004/10. Indiana Department of Transportation and Federal Highway Administration.

Yang, Z., Weiss, W. J., & Olek, J. (2006). "Water transport in concrete damaged by tensile loading and freeze–thaw cycling." Journal of materials in civil engineering, 18(3), 424-434.

Yates, S.R., Van Genuchten, M. Th. ,.Warrick, A.W, Leij, F.J. (1992). "Analysis of measured, predicted, and estimated hydraulic conductivity using RETC computer program." Soil Society of America Journal., 347-354.

Yuan Q, Shi C, De Schutter G, Audenaert K, & Deng D. (2009). "Chloride binding of cement-based materials subjected to external chloride environment–a review." Construction and Building Materials. 23(1): 1-13.

Zhou C, Kefei L, and Jianguo H. (2012). "Characterizing the effect of compressive damage on transport properties of cracked concretes." Materials and structures, 45(3): 381-392.

Zhou C, Kefei L, and Xiaoyun P. (2012). "Geometry of crack network and its impact on transport properties of concrete." Cement and Concrete Research, 42(9): 1261-1272.